Interfacial Study of Input Data in Dynamic Ice-Structure Interaction and Evaluation of Tactile Sensors Usability in Ice-Related Problems

Cathrine Yvonne Pedersen

NORWEGIAN UNIVERSITY OF SCIENCE AND TECHNOLOGY
DEPARTMENT OF CIVIL AND TRANSPORT ENGINEERING

Report Title: **Interfacial Study of Input Data in Dynamic Ice-Structure Interaction and Evaluation of Tactile Sensors Usability in Ice-Related Problems**	Date: **30.08.2014**
	Number of pages (incl. appendices): **181**

Master Thesis	**x**	Project Work	

Name:

Cathrine Yvonne Pedersen

Professor in charge/supervisor:

Knut Vilhelm Høyland

Other external professional contacts/supervisors:

Torodd Skjerve Nord

Abstract:

Tactile sensor recordings have been analyzed in time domain, frequency domain and visually to identify failure processes along a structural interface. Except for the pre-study to this thesis, there was not found anywhere in former literature that the spectral analyze method have been applied at small- scale tactile data from a cylindrical indenter. Underlying data have manly been conducted during the Deciphering Ice Inducted Vibration (EU- HYDRALAB DIIV) test campaign at HSVA in 2011. Both global and local forces have been evaluated. Similar to former studies were intermittent crushing found to dominate at lower indentation rates and brittle crushing at higher indentation speeds. For two test series analyzed in this paper transition speeds were found between 80 -90 mm/s and 60-70 mm/s. Contact area in different crushing regimes have been evaluated. Higher correlations in contact area were observed during tendencies to frequency lock-in. Line-like contact tended to prevail in continuous brittle crushing. Trends in time-history plots of experimental data with theoretical results show a decrease in correlation between local forces with increasing indentation velocities. During tendencies to frequency lock-in a resonant frequency of 8.57 Hz was found. This was slightly below the first natural frequency of the system. A possible sub-harmonic frequency was observed in two of thirteen panels within the same time window.

Usability and the tactile sensors ability to reconstruct rapid pressure changes have been evaluated as a second stage of this thesis. In addition have there been search to develop an experimental routine to calibrate the tactile sensor. A sensor recording with 100 Hz failed in reconstructing a hammer-excitation, but was well reconstructing forces during a compression test of ice with ductile behavior. In general, output data from the tactile sensor was strongly dependent of the calibration file.

Keywords:

1. **Ice-structure interaction**
2. **Failure processes in ice**
3. **Time and frequency domain analysis**
4. **Tactile sensor**

Abstract

Tactile sensor recordings have been analyzed in time domain, frequency domain and visually to identify failure processes along a structural interface. Except for the pre-study to this thesis, there was not found anywhere in former literature that the spectral analyze method have been applied at small- scale tactile data from a cylindrical indenter. Underlying data have manly been conducted during the *Deciphering Ice Inducted Vibration* (EU- HYDRALAB DIIV) test campaign at HSVA in 2011. Both global and local forces have been evaluated. Similar to former studies were intermittent crushing found to dominate at lower indentation rates and brittle crushing at higher indentation speeds. For two test series analyzed in this paper transition speeds were found between 80 -90 mm/s and 60-70 mm/s. Contact area in different crushing regimes have been evaluated. Higher correlations in contact area were observed during tendencies to frequency lock-in. Line-like contact tended to prevail in continuous brittle crushing. Trends in time-history plots of experimental data with theoretical results show a decrease in correlation between local forces with increasing indentation velocities. During tendencies to frequency lock-in a resonant frequency of 8.57 Hz was found. This was slightly below the first natural frequency of the system. A possible sub-harmonic frequency was observed in two of thirteen panels within the same time window.

Usability and the tactile sensors ability to reconstruct rapid pressure changes have been evaluated as a second stage of this thesis. In addition have there been search to develop an experimental routine to calibrate the tactile sensor. A sensor recording with 100 Hz failed in reconstructing a hammer-excitation, but was well reconstructing forces during a compression test of ice with ductile behavior. In general, output data from the tactile sensor was strongly dependent of the calibration file.

Acknowledgements

Contents

List of Figures

List of Tables

Notation

Abbreviations

- *DIIV* - Deciphering Ice Inducted Vibration

- *DOF* - Degree of freedom

- *DFT* - Discrete Fourier Transform

- *FFT* - Fast Fourier Transform

- *HSVA* - Hamburg Ship Model Basin

- *hpz* - High pressure zone

- *ISO* - International Organization for Standarization

- *JOIA* - Japan Ocean Industries Association

- *NTNU* - Norwegian University of Science and Technology

- *USB* - Universal Serial Bus

Greek symbols

Φ_j Angle of force number j

σ_p Standard deviation

μ_k Kinetic friction coefficient

μ_p Mean value

Roman symbols

A_{nom} Nominal contact area

A_{equ} Equivalent contact area

A_{pixel} Pixel area

F_{tot} Total force

P_{mean} Mean pressure

F_j Compressive force in panel j

Q_j Tangential force in panel j

S_j Sum of forces in section j

Y_k^* Complex conjugate of Y_k

B   Panel width

P   Effective pressure

T   Sample length

T_c Impulse duration

W   Curve length of indenter

d   Curve length of each section

h   Ice thickness

r   Normalized covariance

S_{XY} Cross-spectral density

G_{XY} One-sided cross-spectral density

G_{XX} One-sided autospectral density

S_{XX} Autospectral density

B   Shear force matrix

C   Direction matrix

F   Compressive force matrix

R   Correlation coefficient matrix

Chapter 1

Introduction

1.1 General

Offshore exploration of oil and gas in Arctic environments started in the late 1960's in the Beaufort Sea on the northern cost of Canada and Alaska (Gudmestad et al., 2007). Due to the worlds growing energy demand and stronger competition within the field of oil and gas, the industry has been forced to develop and enter new and harsher environments. It is estimated that around 25% of the undiscovered oil and gas resources may be found in areas where an arctic climate is present (Gudmestad et al., 2007). Entering this region demands larger engineering knowledge to withstand low winter temperatures, offshore permafrost, presence of ice as well as darkness and remoteness.

Multiply test campaigns have been funded by governments and industry to solve problems related to operate in arctic waters. One of the main concerns for engineering activities in the Arctic is dynamic ice actions on offshore structures. The 12th of April 1986 a steel caisson structure *Molikpaq*, placed in the Beaufort sea was exposed to significant motions caused by moving ice. Due to the ice-structure interaction Molikpaq was exposed to steady-state vibrations in such range that the structure was close to its limit stability. Before resonance-like ice crushing was only considered at narrow structures with low aspect rations (Bjerkås and Skiple, 2006), but after this episode various test programs have been conducted at different scales in the field of ice-structure interaction. Several researchers have analyzed dynamic ice loads due to crushing failure, since Peyton (1966) reported from the Cook Inlet. Despite of research and funding, outcome of ice- structure interaction processes have not been fully understood and general consensus have not been met. From a dynamic point of view would there during an ice-structure interaction process be of interest how the pressure distribution and contact area are changing with the initial velocity of ice sheets and the elastic deformation rate of the structure. Usually have relations between ice pressure and structural response been separated analyzed in
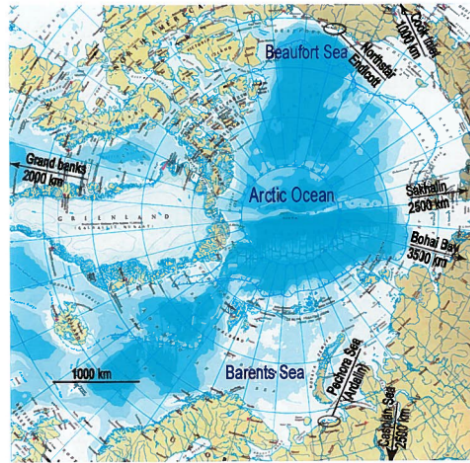
Figure 1.1: Ongoing oil activities in arctic regions (year 2007) (Gudmestad et al., 2007).

time and frequency domain. Findings of steady- state vibrations using time domain have been proposed by e.g. Jefferies and Wright (1988) and Engelbrektson (1997) on full scale data. Respectively on Molikpaq data and measurements from a lighthouse in the Gulf of Bothnia. A stochastic approach to dynamic ice action analyses where first initiated by Jefferies and Wright (1973),(Bjerkås et al., 2006). The idea was followed up by e.g. Määttänen and Reddy (1973) and recently have Kärnä (2003) proposed a new spectral model of evaluating dynamic ice actions.

Earlier have measured results from contact zones been obtained initially from small areas of observation windows (Määttänen et al., 2011). Tactile sensors and load cells are two of many good and different measurement devices to estimate ice actions agents a structure. Tactile sensors have the advantage that they enable extraction of both contact area location and pressure values at high resolution. For this reason tactile sensors have been used on structures in a number of test campaigns over the last years.

This thesis is manly based on tactile sensor data from the Deciphering Ice Induced Vibrations (DIIV) test campaign performed at HSVA in 2011. Measuring systems, ice features and procedure have been described in reports by e.g. (Nord and Määttänen, 2013), (Määttänen et al., 2012) and (Pedersen, 2012). Therefor, only features that are necessarily for understanding of this thesis will be further explained.

1.2   Scope of Thesis

The intention of this research has been to contribute to identification on failure processes in ice along a structural interface. Topics included in this paper are a brief review of literature on ice crushing failure and an overview of the tactile sensor equipment. Data recorded by a tactile sensor during the EU-HYDRALAB DIIV test campaign at HSVA in 2011 have been used to analyze the velocity effects from 10 mm/s to 300 mm/s both in time domain, frequency domain and visually. A flow-chart of how this data may be analyzed is given later in this thesis. Emphasis has been placed on the connection between crushing regimes and initial velocities of ice. But also changes in pressure distribution over the indenter are addressed. This work is limited to level dynamic ice forces and is many considering data from a tactile sensor.

In addition, the usage of a tactile sensor has been evaluated. To get a review over tactile sensors capacity and possible errors, different calibration routines are assessed. Rapid pressure changes are expected along the ice-structure interface. In order to examine if a tactile sensor would record such rapid changes, have the sensor been exposed to a hammer excitation. Compression test of ice have been conducted as a second stage of this evaluation.

Chapter 2

Theory

2.1 Ice-Structure Interaction Processes and Modes of Ice Failure

Ice-structure interaction is a complex process, where deflections usually are a combination of both static and dynamic impact. Ice moving along a structure, may interact with the structure and fail in several different ways. Type of failure mode is particularly dependent on ice properties and velocities of the crushing process. ISO (2010) defines four different modes of ice failure, where three are said to be dynamic ice loads. These different modes and corresponding response regimes are listed in table 2.1.

Table 2.1: Structural response to different crushing phenomena.

Chrushing phenomena	Structural response
Creep crushing	Non of concern from a dynamic point of view
Intermittent crushing	Quasi-static excitation with a decaying transient vibration
Frequency lock-in crushing	Increased response amplitude
Continous brittle	Random stationary response

2.1.1 Creep Crushing

When ice moves against a fixed structure with low velocities (<0.3 mm/s) the ice tends to be deformed in creep. During creep deformation faults in the ice sheet will have time to settle due to low velocities. As a result there may be full contact and uniform pressure at the ice-structure interface. When creep deformations occurs

4

the pressure tends to gradually increase until it reaches a maximum value. With time this ice will settle and gradually reach a steady-sate force around 50-60% of a maximum force (Sodhi and Haehnel, 2003). Creep crushing is not of any remarkable concern from a dynamic point of view and will therefor not be considered further in this thesis.

2.1.2 Intermittent Crushing

The failure mode between ductile and brittle crushing is usually referred to as intermittent crushing. During intermittent crushing ice is usually observed to fail simultaneously along the interface. Velocities in this failure mode are in such a range that pressure has time to build up before it releases. This result in a saw tooth pattern force distribution over time. The force history-plot developing during this failure mode could be divided into two different phases (ISO, 2010). When the loading force-curve is rising we have a loading phase, during this phase the structure is moving in the ice drift direction. At the beginning of a loading phase the ice edge is undergoing ductile deformation. Ductile deformations are moving faster and more continuously as ice actions gradually increases. When a peak value of ice action is reached, brittle crushing starts at the ice edge, leading to transient vibrations in the structure. During an unloading phase the structure falls back to its original position and vibrations decays due to damping in the structure. The cycle then repeats again. Therefore this is often referred to as a quasi-static excitation with decaying transient vibration (Kärnä, 2003).

2.1.3 Frequency Lock-In

Dynamic analyses are manly preformed to ensure that a structure does not enter a self- exciting vibration condition, or frequency lock-in (ISO, 2010). Resonant ice induced vibrations of the structure seems to occur when the ice reaches a special velocity. Typically ranging from 0.04 m/s to 0.1 m/s (ISO, 2010) (Yue et al., 2009). In this mode, Yue et al. (2009) states that the frequency of the ice forces are locked in the natural frequency of the system. However Kärnä (1994) finds from a large among of data that the steady-state vibration occurs at a frequency which is 5% to 15% lower than the natural frequency of the system. Anyway, a lock-in condition may cause large damage to the structure due to severe displacements.

Ice-structure interaction in this mode of failure exhibits alternating phases between ductile loading and brittle unloading (ISO, 2010). Resulting in a sawtooth pattern time-history plot for the force (Sodhi and Haehnel, 2003). Unlike intermittent crushing, Yue et al. (2009) reported about a constant contact between the structure and the ice sheet.

Self- exciting vibration conditions have been reported from several test experiments in different scale. First from full-scale data collected from a drilling platform in

Cook Inlet, Alaska in the 1960s (Blenkarn, 1970). Later have similar events been reported from the *Molikpaq* platform in 1986 and on three multileg jacket platforms in the Bohai Sea (Yue et al., 2009). Frequency lock-in events have also been occurred on other full-scale structures such as the Norströmsgrund lighthouse (Bjerkås et al., 2006),(Bjerkås and Skiple, 2006) and bridge piers (Sodhi, 1988). In laboratory tests have ice-induced vibrations been reported by e.g. Timco et al. (1989), Määttänen (1981) and Nord et al. (2014). However, the lock-in phenomenon is still not completely understood. Different theories and hypotheses have been presented and affect the literature in different directions. Both ISO (2010) and IEC (2009) give guides where a frequency locked-in crushing might occur. ISO (2010) suggest that a locked-in crushing occur between intermittent and continuous brittle crushing, where steady-state vibrations still occurs. The criterion mention in ISO (2010) is based on the concept of negative damping, a phenomenon that is not approved by all researchers in the field of dynamic ice-actions. IEC (2009) base conditions of frequency locked-in on observations during small scale indentation test in laboratory. In contrast to ISO (2010) it suggests the use of a harmonic load, and the tuning criterion is based the ice thickness and velocity, the structures natural frequency and a limiting value. That widely used standards are contradictory like this indicates that there is still a job to do in the field of dynamic forces due to ice crushing.

2.1.4   Continous Brittle Crushing

Normally at velocities higher than 0,1 m/s brittle crushing prevails, (ISO, 2010). In this case both ice actions and the response are said to be random. Ice only gain partial contact with the structure, resulting in a non-simultaneous pressure distribution over the nominal contact area. In this condition there will no longer be any sign to steady-state response and the structure is oscillating with small amplitudes as the ice continuously crushes around the structure. The local pressure changes with time and can be large over small local areas. An averaged pressure over a larger area show lower pressure than the maximum pressure over a smaller area (Sodhi and Haehnel, 2003). In this mode line-like, non simultaneous contact have been discovered by Sodhi and Haehnel (2003), due to the use of tactile sensors.

Despite much research, there are not acknowledged and accepted explanations for the dynamic ice-structure phenomena. The concept of dividing the crushing process into ductile, intermittent and brittle crushing as seen in figure 2.1 where first presented by Sodhi (1989). If the relative speed between the ice flow and the structure is increasing, the failure regime changes towards brittle. In figure 2.1 the arrows indicate three transition speeds which will be dependent on ice properties and aspect ratio (Sodhi, 1989). Sodhi and Haehnel (2003) describes the transition between failure modes due to changes in ice temperature, and (Bjerkås and Skiple, 2006) base their studies on that transition velocities are influenced by both ice thickness and temperatures.
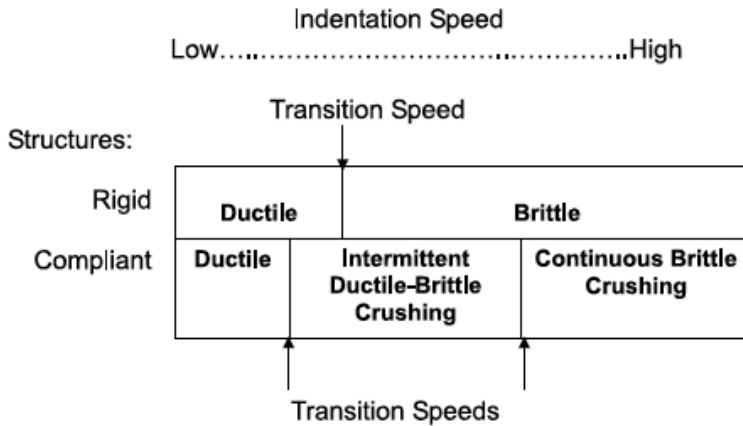
Figure 2.1: Transition velocities between expected modes of ice failure (ductile, intermittent and continuous brittle crushing) during an ice- structure interaction (Sodhi, 2000).

2.2   Local and Global Pressure

Ice is an inhomogeneous material where some areas in the ice sheet may be weaker than other. This implies that when ice crushes against a structure, weaker areas will split and crack easier, than surrounding ice. During the ice-structure interaction process loads will be concentrated at isolated contact points known as high pressure zones *hpzs*, (Jordaan, 2000). This *hpzs* manly occurs due to two reasons:

- Spalling and fracturing in the ice sheet
- Damage layer formation

An illustration of the interface interaction are given in figure 2.2 as five processes (A-E). In the beginning of an ice-structure interaction small scale recrystallization occur and micro cracks form at the edges of *hpzs* (A). The pressure distribution will increase toward the center of *hpzs* (B). Pressure will be so large at the center that a pressure-softening process will start and spread out towards the edges (C). Near the center of the cylinder ice will be strongly recrystallized due to large pressure. The ice will with time sink together as pressure is released and the layer is hardened (D). Recrystallized ice will be extruded and spalling from the edges pushed away from the interaction area. The cycle repeats and leads to dynamic loading (E) (Taylor et al., 2008). In the right corner of Figure 2.2 are the force distribution over time illustrated and point A-E marked.

Analyses of tactile sensor data during high speed test from the JOIA test campaign found that *hpzs* like this covered only around 10% of global interaction area (Taylor et al., 2008). Both global and local forces are pressure multiplied with the nominal

contact area.
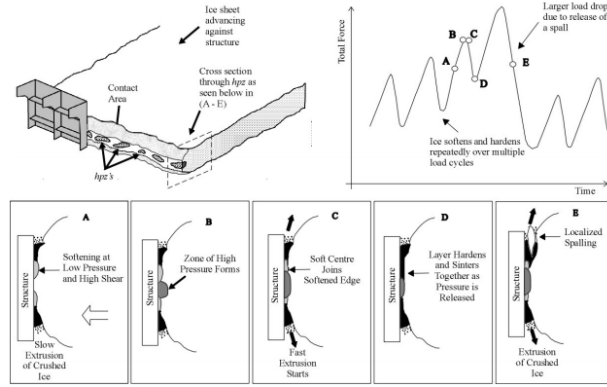
Figure 2.2: *Hpz* formation and load cycling. Figure from Taylor et al. (2010).

2.2.1 Contact Area

The global interaction area is determined by projecting a structure in to the original shape of the ice feature. This definition indicates that global areas are based on the shape of the structure and the shape of the ice feature,(Taylor et al., 2010). When ice is extracted and peeled away from the *hpz*, the actual contact area will change with time. The definition given by Taylor does not account for this change in the global contact area.

By using an instrumentation as a tactile sensor panel may a mean pressure be found by multiplying the total force (F_{tot}) with the panel average over the nominal contact area (A_{nom}) as follows,(ISO, 2010):

$$P_{mean} = \frac{F_{tot}}{A_{nom}} \tag{2.1}$$

$$A_{nom} = B \times h \tag{2.2}$$

Where B indicates panel width and h is the ice thickness. Tests conducted by Taylor et al. (2010) at an indentation rate of 5 mm/s, show that the nominal contact area increases linear with time. At the same time does the shear force and nominal stresses increase through the test. The same article discusses the relationships between failure modes, size of the contact area and pressure distribution. Results in the paper by Taylor et al. (2010) are based on tactile sensor data. A brief summary

will be given here, for complementary theory and description of the conducted tests see Taylor et al. (2010)

Relationship Between Failure Modes and Contact Area

- **Chrushing** Insignificantly changes in distribution and size of contact area between the structure and the ice sheet.

- **Spalling failure** Changes in local load, shape and hpz distribution is often observed from pressure data during a sapling failure.

- **Simultaneous crushing** Due to extrusion of material near the periphery of the hpz are a sudden decrease in intensity frequently found. The shape and position of hpz are not significuly observed.

- **Brittle failure** Easily observed from the load distribution over time. A non-simultaneous peak distribution of the hpz is usual observed. Line-like contact over part of the indenter may be seen (Sodhi, 1998).

2.3   Methods of Data Analyses

Aim with these panel analyses were to find an interval where there may be observed a change in crushing regime. By implementing a method former used by Kärnä (2003), have similarities and patterns in different crushing regimes been analyzed both in time- and frequency domain. It is not known from previous theory that Toumo Kärnä's spectral model have been implemented on data from a cylindrical indenter. In this section are there given a brief overview of the methods and two flow charts on how to proceed. Further explanation regarding the spectral model may be seen in, Kärnä (2003).

Velocity range; 30-300 mm/s

Visual analyses from pressure recordings in I-Scan and cameras

Select a time interval that may be assumed stationary and random

Investigate total and local contact area in Matlab. Compare this to I-Scan.

Frequency domaine analyses

Conduct a spectral matrix in Matlab

Analyze activity close to the natural frequency of the system and symmetry around the indenter

Filter

Find the coherence function

Time domaine analyses

Time-history plots of global and local forces

Evaluate force development around the indenter

Find a correlation coefficient matrix in Matlab

Evaluate and compare the two different methods

Figure 2.3: A flow-chart of how data may be analyzed, based on the project, autumn 2013.

2.3.1 Ice Forces Acting on a Cylindrical Indenter
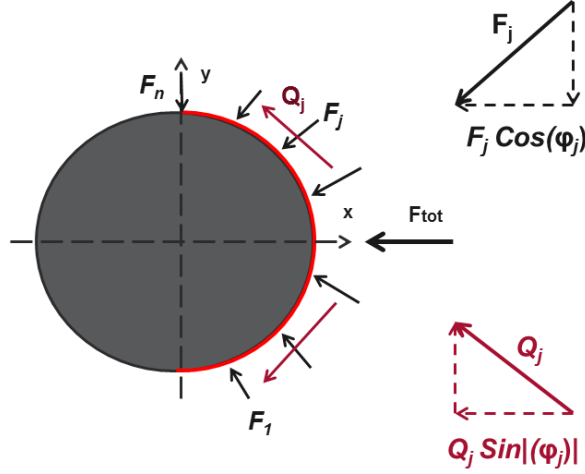
Figure 2.4: Forces acting on a cylindrical indenter.

Local forces acting on an offshore structure may be seen in figure 2.4. As illustrated are positive force values chosen to be in the negative x-direction. The same applies for the velocity vector. Due to the fact that tactile sensors only measures normal forces, have shear forces been decomposed from local normal forces. Local forces are found by discretized the ice-structure contact area into a chosen set of N (j=1,2..n) contact points. In general are local forces composted of two lateral components, (Kärnä, 2003). Tangential components are denoted Q_j^c and compressive local forces F_j^c. Two column vectors $C = [C_j]^T = [cos(\Phi_j)]^T$ and $B = [B_j]^T = [sin|(\Phi_j)|]^T$ are used during summation of the total force. Vector **C** make sure that only those components acting in the requested direction are taken in to consideration of a total force. While **B** ensure that a component of shear force contributes to the total force. Typically constitute shear forces to a very small proportion of the total force, however this depends on the ice-structure friction coefficient and the velocities of the interaction process. In this report are not a study of friction coefficients emphasized, therefor are the same conditions assumed to apply also in the horizontal direction. With this assumption are rations between shear forces and normal forces given as:

$$|Q_n^c(t)| = \mu_k F_j^c(t) \tag{2.3}$$

The kinetic friction (μ_k) will decrease with increasing sliding velocities. When velocities approaches zero will the static friction coefficient dominates. Due to relatively high velocities and small shear force contributions have only kinetic fric-

tion been considered in this report. For further interest in dependency of friction coefficients see Lourens (2012).

2.3.2 Time Domain Analyses

Composition of Total Forces from Compressive and Shear Forces

Both local and global time-history plots should be conducted to determine type of crushing regime. To investigate similarities in crushing pattern around the indenter can local forces be compared and visual described.

Total forces in time domain only considering compressive forces are found by equation 2.4

$$F_d(t) = \mathbf{C}^T \mathbf{F}(t) = \sum_{j=1}^{n} C_j F_j(t) \tag{2.4}$$

Where n is the number of segments and C_j are normal forces acting in the current direction. Shear forces may be included by determine a kinetic friction coefficient and rewriting equation 2.4;

$$F_d(t) = (\mathbf{C} + \mu_k \mathbf{B})^T \mathbf{F}(t) = \sum_{j=1}^{n} C_j F_j(t) + \mu_k \sum_{j=1}^{n} B_j F_j(t) \tag{2.5}$$

Where B_j refers to shear forces in location j.

2.3.3 Correlation and Correlation Coefficients

At an instant in time, the total force F(t) on the indenter is equal to the sum of forces acting in each segment $S_j(t)$. This includes shear forces and may be described as in equation 2.6.

$$F(t) = \sum_{j=1}^{n} S_j(t) \tag{2.6}$$

In literature on ice crushing effective pressure is given as total interaction force divided on contact area (Sodhi et al., 1998). The effective pressure can then be expressed as (Sodhi, 1998):

$$p(t) = \frac{1}{n} \sum_{j=1}^{n} \sigma_{p_j}(t) \tag{2.7}$$

Where σ_{p_j} is tangential force in location j. If h is representing the ice thickness, d the curve length of each section and W indicates the indenter curve length, are $p_j(t) = s_j(t)/(hd)$ and $p(t) = F(t)/(hW)$. The mean value (μ_p) and the standard deviation (σ_p) are given as;

$$\mu_{p(t)} = \frac{1}{n} \sum_{j=1}^{n} \mu_{p_j}, \tag{2.8}$$

and

$$\sigma_{p(t)}^2 = \frac{1}{n^2} \sum_{i=1}^{n} \sum_{j=1}^{n} E[(p_i(t) - \mu_{p_i})(p_j(t) - \mu_{p_j})] \tag{2.9}$$

μ_{p_j} represents a mean of the effective pressure in each section. In Ewins (2000) variance and covariance are given by;

$$\sigma_{p_i}^2 = E[(p_i(t) - \mu_{p_i})^2], i = j \tag{2.10}$$

$$\sigma_{p_i p_j} = E[(p_i(t) - \mu_{p_i})(p_j(t) - \mu_{p_j})], i \neq j \tag{2.11}$$

Now the *correlation coefficient or normalized covariance* may be found from the variance of the effective pressure, Newland (1984);

$$r_{ij} = \frac{\sigma_{p_i p_j}}{\sigma_{p_i} \sigma_{p_j}} \tag{2.12}$$

Where $0 \leq |r_{ij}| \leq 1$ for any pair of sections. One represent a perfect correlation and vice versa. From equation 2.10 are there found that taking the self correlation $i = j$ should always give $r_{ij} = 1$. If effective pressure in each section is independent of effective pressure in other sections are the covariance equal to zero, and the standard deviation expressed in equation 2.9 written as;

$$\sigma_{p(t)}^2 = \frac{1}{n^2} \sum_{i=1}^{n} \sigma_{p_i}^2 \tag{2.13}$$

Where σ_{p_j} is the standard deviation of the effective pressure generated in each section. The assumption that an ice crushing process is assumed to be a stationary random process simplify equation 2.13:

$$\sigma_{p(t)} = \frac{\sigma}{\sqrt{n}} \tag{2.14}$$

13

Kry (1978) found that, increasing the number of independent areas of crushing, keeps the average global effective pressure the same in each segment. The standard deviation of global effective pressure may then decreases as the reciprocal of the square-root of number of sections. The assumption of effective pressure being independent in each segment is valid if the size of crushing zones are small compared to the width of a segment. Then again this is not valid if the size of crushing zones is comparable or larger than the segment width (Sodhi, 1998). In this report, all experimental data are analyzed by use of Matlab. An integrated function *corrcoef* have been used to find correlation coefficients between panels. $\textbf{\textit{R}}$=*Corrcoef(X,Y)* calculates a matrix $\mathbf{R}$ of correlation coefficient between X and Y, based on the above theory. When using the embedded *Corrcoef* function in Matlab may correlation plots show negative correlations, this would be the case when one variable tends to be above its mean when the other variable is below its mean.

2.3.4   Frequency Domain Analyses

The aim of this section is to give background theory for stochastic dynamic analyses used on tactile sensor data further in this thesis. First some essential prerequisites will be explained. Then, main basic equations used in stochastic frequency domain analyses are given.

Ice Excitation; As a Stationary Random Process

A random process is said to be stationary if the probability distributions obtained for the ensemble does not depend on absolute time (Newland, 1984). This implies that the mean, mean square, variance and standard deviation of the process are independent of time. In fact, all the averages should be independent of absolute time. Since most engineering random processes must have a beginning and ending, they cannot be truly stationary. Excitations during an ice-crushing event are one of these engineering processes. For practical purposes it is often adequate to assume that a process is stationary for a majority of its lifetime, or that it can be divided into sub-events where each of them may be approximately stationary (Newland, 1984). With assumption about stationarity, theory of random vibrations may be applied to dynamic ice actions.

In this report ice- structure interaction processes are considered to be stationary when forces are divided into properly selected periods where the excitation can be considered stationary and stochastic within each period (Kärnä and Yan, 2009). Intervals in time where the interaction proses is said to be stationer, are further in this paper referred to as sub-events. Auto-spectral density functions have in former literature showed highest values in the range of lower frequencies (Kärnä and Yan, 2009). To ensure that higher frequencies are represented should the range of each sub-event be sufficiently long. To counteract this did Kärnä and Yan (2009) not use sub-events shorter than 36 seconds. However data analyzed in

this thesis are significantly shorter. To ensure stationarity are each sub-event in average extending over a 15 seconds time interval. During test series 4300 are each sub-event ranging over a constant velocity step. Simple visual controls of the mean level in force plots have been performed to ensure that assuming stationarity is no entirely wrong. However, further investigations should have been conducted.

Fast Fourier Transform and Basic Analysis

An infinite-range Fourier transform of a record v(t) is defined by;

$$V(f) = \int_{-\infty}^{+\infty} v(t) e^{-j2\pi ft} \, dt \tag{2.15}$$

This equation will not be valid for an v(t) that is a representative number of a stationary random process when infinity limits are used (Bendat and Piersol, 2010). In practice a finite range Fourier transform must be evaluated.

In spectral analyses are fast Fourier transforms used to give estimates on spectral density and correlation functions. FFT is a computer algorithm to calculation discrete Fourier transforms (DFT). Consider a pair of sample records $x(t)$ and $y(t)$. Both ergodic Gaussian random processes $\{x(t)\}$ and $\{y(t)\}$, divided into segments x_k and y_k on an unlimited sample length T. Fourier transform for a finite time interval $0 \le t \le T$, will thereby be expressed in equation 2.16 and 2.17.

$$X(f) = X_k(f, T) = \int_0^T x_k(t) e^{-j2\pi ft} \, dt \tag{2.16}$$

$$Y(f) = Y_k(f, T) = \int_0^T y_k(t) e^{-j2\pi ft} \, dt \tag{2.17}$$

The cross-spectral density function is then given by equation 2.18.

$$S_{XY}(f) = \lim_{T \to \infty} \frac{1}{T} E[X_k(f, T) Y_k^*(f, T)] \tag{2.18}$$

Where $Y_k^*(f, T)$ represent the complex conjugate of $Y_k(f, T)$. From equation 2.18 is the one-sided cross-spectral density function given as follows;

$$G_{XY}(f) = 2 \lim_{T \to \infty} \frac{1}{T} E[X_k(f, T) Y_k^*(f, T)] \tag{2.19}$$

Note that S(f) is replaced by G(f) when considering the one-sided spectrum. For more details see Bendat and Piersol (2010). A special case of the one-sided cross-spectral function is the one-sided autospectral density function $G_{xx}(f)$. This function will for all values of f be positive, unlike the cross-spectral density function

15

that basically consists of a real part and a imaginary part. However, when using the method for ice forces analyzes, the imaginary part is neglected as a simplification (Kärnä and Yan, 2009).

$$G_{XX}(f) = 2 \lim_{T \to \infty} \frac{1}{T} E[|X_k(f,T)|^2] \tag{2.20}$$

Equal to equation 2.18 and 2.19 is the autospectral density function given by equation 2.21

$$S_{XX}(f) = \lim_{T \to \infty} \frac{1}{T} E[|X_k(f,T)|^2] \tag{2.21}$$

Input and Output Modeling

A general case of a multi-DOF system is divided in to several nodal points n, where the Fourier transform of the excitation is given by;

$$F_n = \begin{pmatrix} F_1 \\ F_2 \\ \vdots \\ F_n \end{pmatrix} \tag{2.22}$$

Equation 2.21 is then expressed as;

$$S_{XX}(f) = \lim_{T \to \infty} \frac{1}{T} E[F_K(f,T)F_K^{*T}(f,T)] \tag{2.23}$$

$F_K^{*T}(f,T)$ represent the transposed of $F_K^*(f,T)$. If equation 2.23 is used to create a matrix $S_{FF}(f) = [S_{F_i F_j}(f)]$ where i and j is the position for all nodal points n. $S_{FF}(f)$ will be a matrix with the auto spectral density function of the local forces F_i at the diagonal. This matrix is expressed in 2.24 for a general case F_n.

$$S_{F_i,F_j}(f) = \begin{pmatrix} S_{F_1,F_1}(f) & S_{F_1,F_2}(f) & \cdots & S_{F_1,F_n}(f) \\ S_{F_2,F_1}(f) & S_{F_2,F_2}(f) & \cdots & S_{F_2,Fn}(f) \\ \vdots & \vdots & \ddots & \vdots \\ S_{F_n,F_1}(f) & S_{F_n,F_2}(f) & \cdots & S_{F_n,F_n(f)} \end{pmatrix} \tag{2.24}$$

The spectral matrix $S_{FF}(f)$ may be used to find an estimate on total forces acting around a cylinder. For further explanation see Kärnä (2003). A flowchart in figure 2.5 is illustrating how data may be implemented in Matlab.
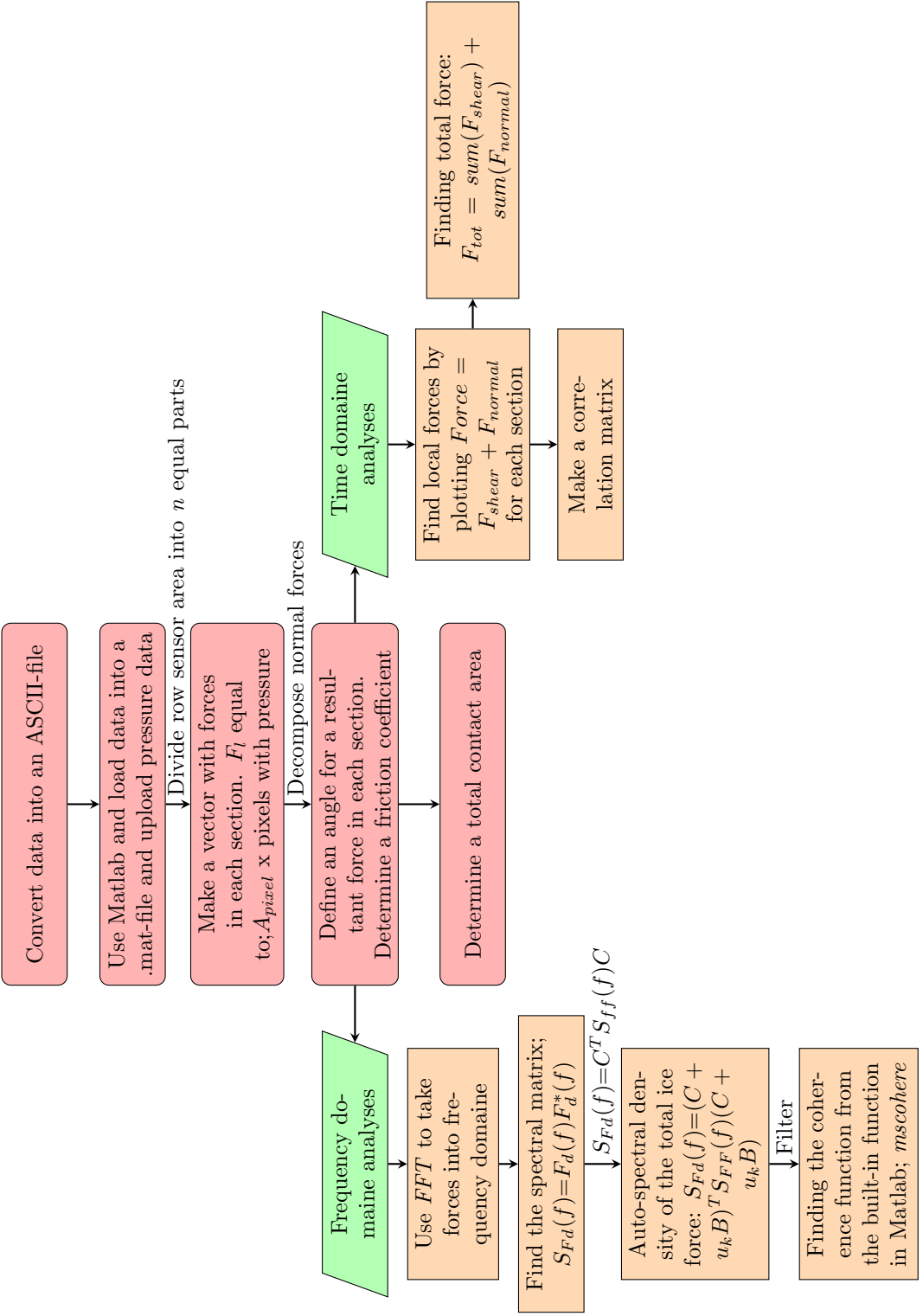
Figure 2.5: Overview of methods used to processing data.

Chapter 3

Equipment

3.1 Tactile Sensor

The tactile sensor is a resistive sensor that first was developed to use in the dental industry, but have in later times been further developed to use both in medical and technological industry (Granheim, 2011). In geotechnical research tactile sensors have been used to investigate normal stresses in soils due to the sensors high capacity and flexibility. Tactile sensors have the advantage that they enable extraction of both contact area location and pressure values at high resolution. For this reason tactile sensors technology have been adapted to understand complex loading distributions also by the ice research community. Ice research with tactile sensors have been preformed by e.g. Määttänen (2011) and in the Japan Ocean Industries Association (JOIA) test campaign to study the details of high pressure zones (*hpzs*) behavior, Taylor(2008).

3.2 Tekscan Pressure Measurement System- 5513

Tekscan Pressure Measurement System consists of a sensor template, a USB Handle and a software program. Detail information about procedure for this system is easily found in the user manual that comes with the program. A brief overview is summarized here.

1. If the application has not been connected to a computer before; Install the software.

2. Connect the USB handle to a computer. Open the handle and connect the sensor tab.

3. Start a new blank session in I-Scan to see that everything is working.

4. Calibrate the sensor:

    (a) Check units

    (b) Adjust the sensitivity before saving any calibration points. All calibration points will be deleted if the sensitivity is changed.

    (c) Preform a two or one-point load calibration.

    (d) Save the calibration file on you computer.

5. Mesuring:

    (a) Open a new session and load the initial calibration file.

    (b) A recording is started by pressing the red button on the toolbar or the recording start/ stop button on the USB handle.

    (c) After end session; Stop recording and save file.

6. When a recording have been stored, it is possible to change calibration files on the recorded movie.

3.2.1 Sensor Template

A tactile sensor of model 5513 produced by *TEKSCAN Icn.* were used during the DIIV test campaign. Same model were applied during laboratory test described later in this thesis. Therefor the 5513 model is further described in this chapter. There are various sensors available on the market for specific usage. This 5513 model was chosen mainly due to three reasons;

- **Pressure measuring range** Sufficiently large pressure measuring range needed at HSVA.

- **Coverage** Dimensions of the sensor template, covers the front of the cylindrical indenter used at HSVA.

- **Tab length** A tab length of 397.5 mm make it possible to have the USB handle further from the waterline during ice experiments.

Figure 3.1 illustrates the sensor template for model 5513. The sensor template has rows and columns in a checkerboard pattern that consist of an electrically conductive material separated by semi conducting inks. Due to variations in electrical resistance between inks, signals are sent to the USB handle. The 5513 model has overall dimensions of $609.6mm \times 474mm$, with matrix dimensions of $416.1mm \times 156.5mm$. This sensor is composed of 44×55 sensing elements (pixels) where each pixel have a column width of 5.7 mm and spacing of 8.0 mm. The temperature range for the 5513 model is from -9°C to -60°C (Lu, 2013). An overview of parameters for sensor model 5513 is given in table 3.1.
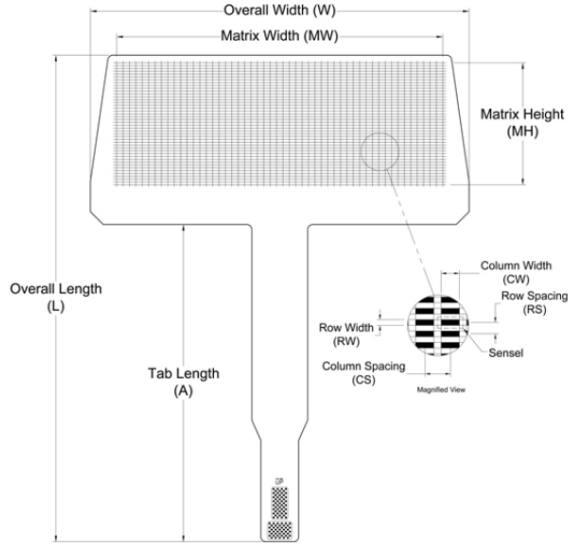
Figure 3.1: Tactile sensor template model 5513. Illustration from Lu (2013).

Table 3.1: Essential parameters, sensor model 5513.

Overall Length [mm]	Overall Width [mm]	Tab Length [mm]	Matrix Width [mm]	Matrix Height [mm]	Columns	Rows	Pressure range [MPa]
609.6	474	397.5	416.1	156.5	55	44	0-175

3.2.2 USB Handle

The USB handle used during laboratory tests at NTNU and at the HSVA campaign was of the type EH-2 produced of Tekscan, Inc. It consists of a handle that opens for the ability to connect the tab to a data logger. The USB handle connects to the computer through a UBS port. The USB handle gathers data from the sensor so it can be seen in a special software program in real time. This UBS handle can also be used to stop and start recording. When the USB handle is connected to the computer, a test will run to check the connection between the logger and the computer. A picture of the USB handle is given in figure 3.2.
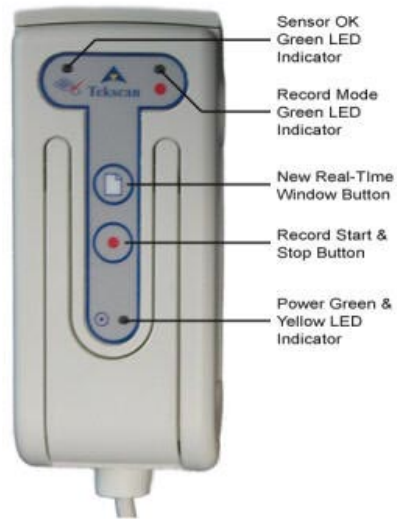
Figure 3.2: USB Handle (Tekscan, 2012).

3.2.3 Software

I-Scan 1.6X software is a graphical program that illustrates the pressure distribution at the sensor template, using 13 different colors that illustrate a pressure interval. Color ranges are seen in a legend, as the one displayed in figure 3.3. The legend illustrates a pressure interval for each color where the number displayed on each color is the lowest value in that color's range. Pressure ranges can be changed by increasing or decreasing the upper or lower limit value.

A pressure distribution recording may be given in real time and be saved as a movie where the I-Scan program records with a given frequency. The maximal recording frequency with the technology used at NTNU and HSVA was 100 Hz. I-Scan 1.6X uses map files to convert the pressure detected by the hardware into pressure data displayed in the real-time window (Tekscan, 2012). Recorded pressure distributions may both be given in 2D and 3D presentations where it is possible to look at the pressure distribution in individual frames separately and control the contact area. I-Scan also has the advantage that it is possible to have a force distribution in a chosen area as a function of time and determine the location of the resultant force. After recording a set of frames in a movie may I-Scan use the file extension ASCII so information can be taken in to separate worksheets.
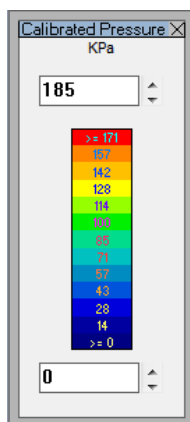
Figure 3.3: Legend displayed in I-Scan.

3.3 Calibration of Tekscan Tactile Pressure Sensor-5513

According to the I-Scan user manual equilibration and calibration of sensor should be preformed before use.

Equilibration is preformed to minimize the variation between individual elements in the sensor template. This should be completed before calibrating the sensor. An equilibration is conducted by applying a highly uniform pressure across the individual sensing elements. Applied pressure during equilibration is recommended to be close to the highest pressure expected during tests. If outputs from each element within the sensor are not uniform, the software determines a unique scale factor to compensate for these variations. The main reason for different sensitive element outputs during identical pressure is that some areas on the sensor template have been exposed to more pressure then other and therefore contains more worn pixels. Different output may also have to do with lost continuity between rows or columns. Lost continuity may occur when sensors have been folded during storing or transport. For more information on equilibration see the I-Scan user manual.

Calibration should be preformed every time the sensor is used for a new application. Sensors give output in RAW data during calibration. RAW data tell something about the applied pressure relative to the given sensitivity. For a given sensitivity will RAW numbers varies from 1 to 255. When the sensor template is charged the color combination in the I-Scan window is used to select a good combination of sensitivity and saturation. Most important, pixels should not be overloaded (showing read color) and the smallest measurable pressure change (kPa/RAW)/ (N/RAW) should be as small as possible. Primarily there are two different methods to calibrate the sensor (Granheim, 2011);

- Force calibration: The sensor template is loaded with one ore two known

loads. This two loads will be calibrated agents an average RAW value for this loads (N/RAW).

- Pressure calibration: The sensor template is exposed to different known pressures, evenly distributed over the sensor template. This pressures are then calibrated agents an average RAW-value (kPa/RAW).

In the Tekscan manual, they recommend the use of their own calibration devise. The calibration devise consists of a thin flexible membrane that should be wrapped around the sensor template and pressurized. For more information regarding the calibration devise, read the Tekscan user manual. Pressure calibration will not be evaluated further in this thesis due to lack of this pressure device at NTNU.

For best results 25% of the sensing element area should be exposed to an evenly distributed loading, which is approximately 20% of the maximum loading expected during the actual application. This will fine-tune the sensor to measure within the interesting voltage range.
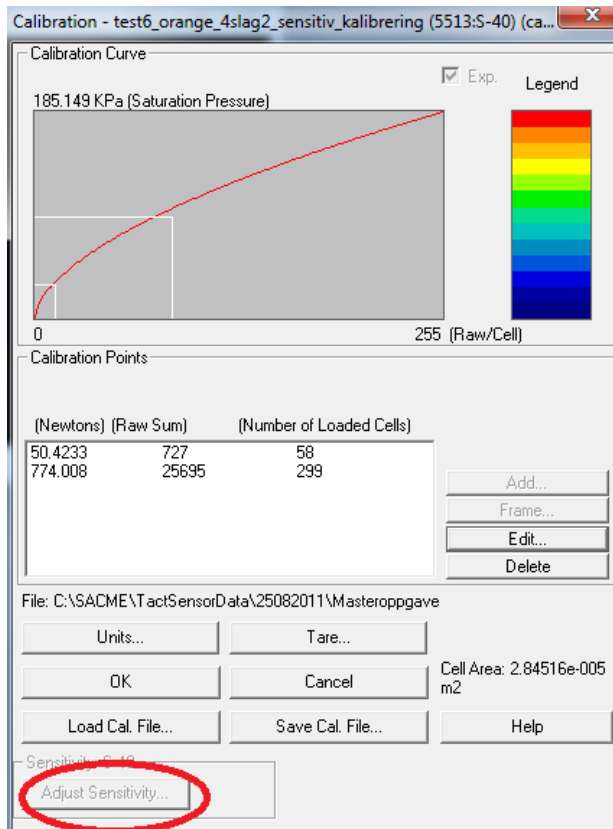
Figure 3.4: Illustration of calibration toolbox in I-Scan. Marked where sensitivity may be adjusted.

When an acceptable sensitivity is found, force calibration mainly are preformed in two different ways:

- Singel Load (Linear) Calibration
- Two-Load (Non-Linear) Calibration

Single Load Calibration uses the fact that when zero load is applied the sensor have zero output. When a known load is applied, I-Scan draws an extrapolated line through two points and zero in a RAW/force-plot as illustrated in figure 3.4. This calibration method is preferred when the pressure distribution with different loads is similar. During a Non-Linear calibration two loads with precisely known weight are entered into the software correctly, and applied to the sensor. For best result it is recommended that this two loads are respectively 20 % and 80 % of the highest expected pressure value. I-Scan uses iteration to calculate a power law equation for calibration in the RAW/force-plot seen in figure 3.4. According to the Tekscan manual, the advantage of a two-point load calibration is that it may help to reduce errors if the experimental loads vary over a large range.

Figure 3.5 and 3.6 are taken from the user manual to illustrate the concept of single load and two-point load Calibration.
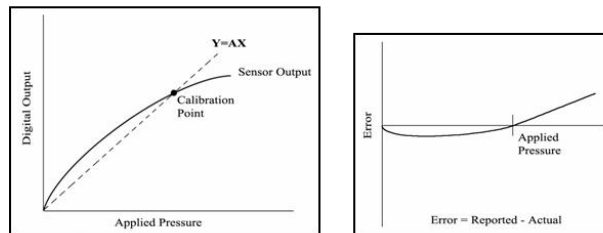
Figure 3.5: Illustration of single-load calibration concept and expected error (Tekscan, 2012).
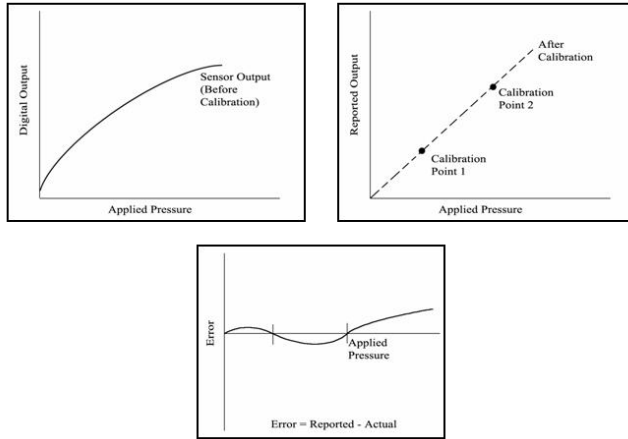
Figure 3.6: Illustration of two-point load calibration concept and expected error (Tekscan, 2012).

3.3.1 General Considerations During Calibration

In general, three important considerations have to be taken during calibration:

1. **Saturation pressure and sensitivity**

   It is important to find a usable combination between required sensitivity and saturation. These two properties are influence each other, low sensitivity lead to high saturation pressure and vice versa. The trade-of between range and resolution may be seen in figure 3.7.
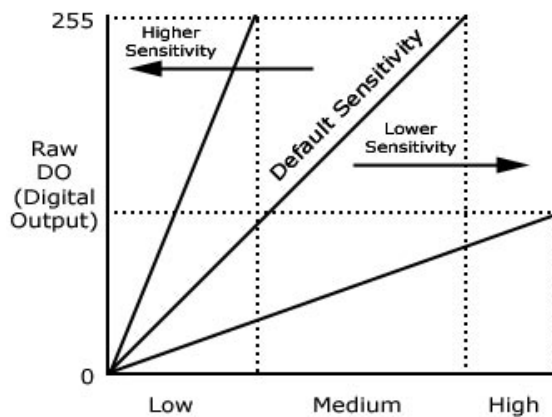
Figure 3.7: Relationship between saturation and range of pressure that can be measured (Tekscan, 2012).

Good saturation during calibration may easily be seen by test loading the sensor before actually generating a calibration file. An appropriate sensitivity is illustrated in figure 3.8b.

(a) Low sensitivity.   (b) Good sensitivity.   (c) High sensitivity.
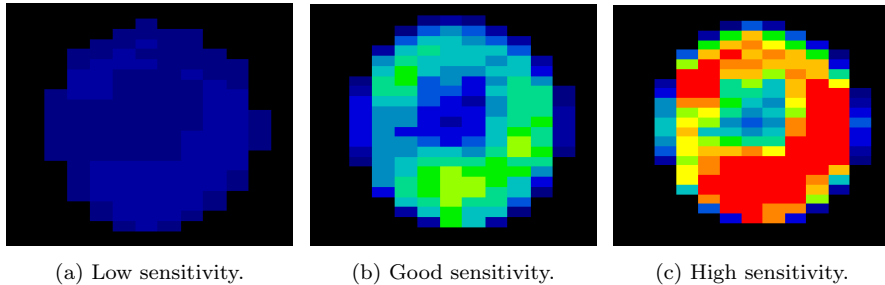
Figure 3.8: Illustration of sufficient sensitivity. Pictures from laboratory test.

2. **Material interface**

Type of material used during calibration will have influence on the pressure distribution. The material used in contact with the sensor template should be thin and flexible. This to gain an evenly distributed pressure over the loaded sensing elements. Using materials with a mating surface or high structural stiffness will influence the actual pressure being applied to the sensor. Figure 3.9 displays an example of good and an uneven pressure distribution.

(a) Pressure distribution on sensor template when using steel as loading material.

(b) Example of an acceptable pressure distribution. plexiglas used as loading material.

Figure 3.9: Example of pressure distributions with different materials.

3. **Temparature**

It is recommended to calibrate the sensor template close to its working temperature. Change in temperature between calibration environment and test environment may give an error around 0.25 % for every degree Fahrenheit change in temperature (Lu, 2013).

3.4 Synchronization of Tactile Data With Other Measurement Devices

Tactile sensor data gives value information on processes in ice-structure contact zones. Together with strain-gauges and accelerometers, processes developing in contact zones can be related to a structural response. In order to compare data from different measurement equipment, it is first of all important to synchronize recorded time series. In this thesis comparison of data from the tactile sensor and recorded movies were based on visual observations. A point in time where it could be seen from pressure recordings in I-Scan and movies that the indenter was reaching the ice was used as a synchronization point. Recorded data between strain- gauges, accelerometers and the tactile sensor were sync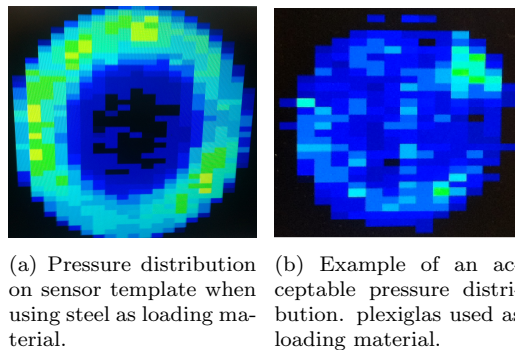hronized by finding the first peak when the indenter entered the ice. Doe to a clear force peak at the time the indenter entered into the ice, this was easily preformed in test 4300 and 3100. Synchronizing by using a starting point like this would most likely give good results for time tracks around this point. However Määttänen et al. (2011) reported about a time lag hidden in tactile sensors physical operation. By comparing initial peak load from tactile data and strain-gauges, Määttänen et al. (2011) found a depreciation in time during fast changing crushing phenomena. The average peak pressure measured with strain gauges was in general higher than what was found from tactile data. A trend like this will effect how data should be synchronized. Several distinct synchronization points through time series would be a possible solution for this problem. Since manly tactile sensor data is discussed in this thesis, further investigations on time lag will not be preformed.

Chapter 4

Laboratory Tests and Calibration of Tactile Sensor

4.1 Impact Excitation

A tactile sensor of the same type as described in the previous chapter has been exposed to hammer excitation on an aluminum beam. The purpose was to investigate the sensors ability to reconstruct the force impulse from an hammer impact. To which extent calibration files have an impact on the force reconstruction has been evaluated as well.

4.1.1 Hammer Excitation

A relatively simple measurement process to excite a structure into vibration is through an impactor as the one seen in figure 4.1a. Usually the impactor has either a load cell or an integrated force transducer, which detects the force magnitude felt by the impactor. Forces recorded by the sensor are assumed to be equal and opposite to the force experienced by the structure (Ewins, 2000). This makes it possible to compare loads recorded by the impactor with loads recorded by another sensor. The load is predominantly effected by the hammer head's mass and the impact velocity.
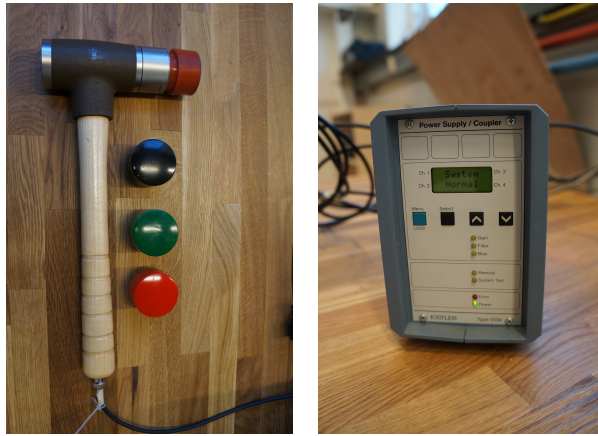
(a) Impact hammer used during experiments preformed at NTNU.

(b) Transduser used during hammer impact tests of tactile sensor.

Figure 4.1: Equipment used during hammer impact testing.

The challenge in recreating forces from a hammer impact is the short duration of the impulse. As a result of this, requirements to the sampling rate are necessarily. A typical impact force pulse is illustrated in figure 4.2. This figure illustrate that a hammer impact pulse is presented in a short time window, given in microseconds. Tc indicates the duration of the pulse. Force identification from a hammer impact has recently been preformed in a much larger scale by Lourens (2012). Her work gave relatively good results on force reconstruction using 34 accelerometers at different positions on a steel beam. There are not know of earlier published literature where force from a hammer impact have been reconstructed using a tactile sensor.
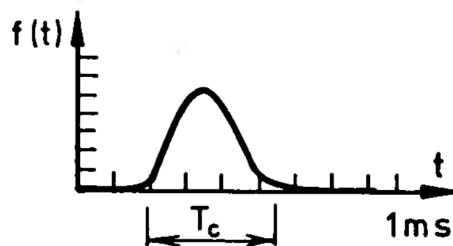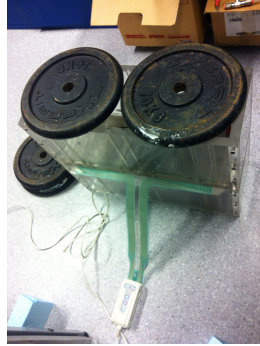

Figure 4.2: Typical force pulse from an impact hammer (Ewins, 2000).

(a) Steel wights used to load the sensor during calibration.

(b) Use of plexiglas above and below the sensor template.

Figure 4.3: Calibration with weights and plexiglas.

Experimental Setup and Proceedure

To become familiar with the tactile sensor and the calibration routine before the actual impact test. Three test calibration files were made by loading the sensor template with different loads, loading area and material, see figure 4.3. To reduce errors, only two-point load calibrations were preformed. A flexible loading material that gives an even loading distribution is recommended by the Tekscan manual to use during calibration. In this calibration tryout steel, polystyrene, wood and plexiglas were used as the closest material to the sensor. For steel materials the loading distribution was uneven with a large error in the actual contact area. This was most likely due to the high stiffness of steel. The same was observed for polystyrene materials, only that they were too soft. The material placed on top of the polystyrene would have a significant impact on the actual force distribution. The sensor template was placed on a wooden panel to be more flexible, than it would be on the concrete floor. However this did not provide the desired flexibility. Two plexiglas boxes were then used, one was placed under the sensor template and one was placed over the template and loaded with weights as seen in figure 4.3b. This provided a good solution with respect to flexibility of the structure. A preferable solution was found by using plexiglas in the bottom and a 10 cm steel cylinder at the top of the sensor, see figure 4.4a. This solution yielded good results between forces recorded by the sensor and forces applied. Test setup can be seen in figure 4.4. Three calibration files were made and the force recorded was compared with the applied force and noted for this solution. Result can be seen in Appendix B.

(a) Tactile sensor placed on a wooden board and plexiglas.

(b) Loaded cylinder. The tactile sensor are resting on a plexiglas box.

(c) Steel cylinder with a diameter of 10 cm. Used during calibration.
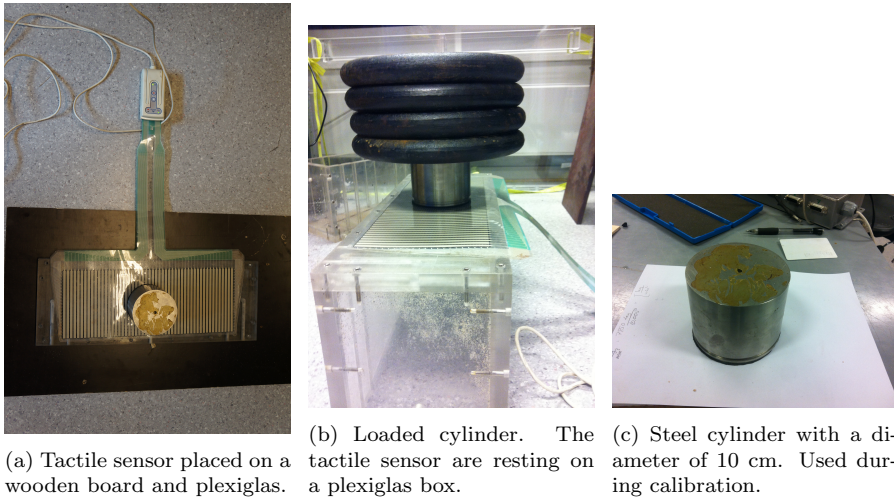
Figure 4.4: Calibration devices.

As preparation for the hammer excitation test were the impact hammer tested eight times against an aluminum cross section placed over two trestles. Test strokes was carried out to identify in witch force range a calibration had to be preformed before the actual hammer impact was tested with the tactile sensor. In this experiment, we used an impact hammer of the brand Bruel and Kjær - 8208, see figure 4.1a. The impactor had an integrated load cell and came with four impact tips with different hardness. Figure 4.1 show an amplifier of type 5146 produced by *Kistler instrument corp.* This amplifier was connected to the hammer and linked to the computer where data was implemented directly in Matlab. Force recordings for four different tips are presented in table 4.1. It is important to notice that orange is the softest tip and black hardest.

Table 4.1: Expected force range during hammer excitation, [N]. Found from test strokes.

| Stroke number	Orange	Green	Red	Black
1	1823	2616	3166	2147
2	2403	2151	3898	2717

Four test series of hammer impact were preformed with four strokes in each series. During earlier test strokes, a general hammer sensitivity had been implemented in Matlab. Hammer sensitivity was during the actual test changed to a given specific sensitivity for this particular hammer. Therefore it was expected that the recorded force during actual strokes will be smaller than forces recorded during test strokes, (see table 4.1). Higher sensitivity during test strokes was a mistake, and should not be seen as an usual procedure.

The aluminum cross section had a natural frequency around 40 Hz and was chosen due to its ability to be more flexible than a concrete floor. Due to the flexibility of the structure used at HSVA it was desired to use a flexible structure during impact tests. Contact time between the hammer and a flexible structure will last for a longer time, than hammer excitation agents a fixed structure. This gives the sensor more time to record the force signal. Picture of test setup and how the sensor was attached to the aluminum section may be seen in figure 4.5.

The I-Scan user manual recommend to have calibration loads in the range of 20% and 80% of the highest expected load during tests. Therefor only the two softest tips were tested during the experiment. Harder tips would have been used if higher calibration loads had been available at the time. The tactile sensor was recording with a frequency of 100 Hz during all four tests.

(a) Sensor were connected to the aluminum section using tape.
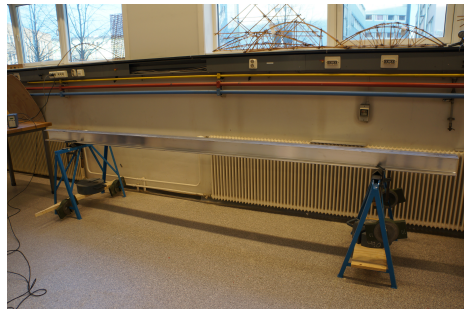
(b) Aluminum cross section used during hammer excitation.

Figure 4.5: Picture of hammer impact test system.

Two two-point load calibration files with different sensitivity and loading range were prepared for the hammer impact test, both statically. The sensor template was placed on a wooden board and plexiglas to achieve an even loading distribution and more flexible loading plane, see figure 4.4. To gain control over the actual contact area and the contact area given by the tactile sensor, weight bars and a steel plate were loaded on a steel cylinder placed on the tactile sensor. The same solution was described previously. Diameter of the cylinder was 10 cm. (Figure 4.4c). The sensitivity of calibration file one and two were 32-S and 40-S, meaning that calibration file two is more sensitive than file number one. For both calibrations, weight bars were removed carefully one by one to register force changes and contact area recorded by the sensor. This were noted and compared to the actual force. Results are seen in tables 4.2 and 4.3.

Table 4.2: Testing calibration file number 1.

Weight [Kg]	Calculated force [N]	Sensor [N]	Deviation [N]	Contact Area [m^2]
5.14	50.4	5.1	45,3	0.0005
34.14	333.9	202.4	131.5	0.0048
44.14	433.0	267.1	165.9	0.0056
54.14	531.1	349.1	182.0	0.0063
74.14	727.3	562.8	164.5	0.0067
99.14	972.6	797.5	175.1	0.0069
124.04	1217.8	1167.7	50.1	0.0069
144.04	1414.0	1432.2	18.2	0.0070
159.04	1561.2	1598.4	37.2	0.0071
174.04	1708.3	1749.9	41.6	0.0073
184.04	1806.4	1856.8	50.4	0.0075
194.04	1904.5	1968.1	63.6	0.0075
204.04	2002.6	2103.3	100.7	0.0077
214.04	2100.7	2215.4	114.7	0.0077
229.04	2247.9	2256.0	8.1	0.0078
234.04	2296.9	2310.5	13.6	0.0078
239.04	2346.0	2356.2	10.2	0.0078

Table 4.3: Testing calibration file number 2.

Weight [Kg]	Calculated force [N]	Sensor [N]	Deviation [N]	Contact Area [m^2]
28.9	283.5	459.0	175.5	0.0078

Hammer Impact Results

Forces recorded by the tactile sensor read from both I-Scan, Matlab and recordings from the impact hammer for all four test series are given in table 4.4. Column two and five show respective tip color and recorded force. Each test series are numerated from one to four where every stroke in each series is numerated from on to four. These are the numbers that would be referred to further in the text.

In table 4.4, column five and six may there be seen a different force given directly from I-Scan and data implemented in Matlab. The percentage difference between F_{I-Scan} and F_{Matlab} is approximately the same for all hammer tests. This inconsistent is most likely due to a systematic error, such as different definition of contact area. There are not found any explanation in the I-Scan user manual how I-Scan calculates force from the recorded pressure. In the implemented Matlab script is an equivalent area (A_{equ}) considered, while in I-Scan may only pixel area (A_{pixel}) have been used (see figure 4.6). However, these mismatches are only recognized and not further investigated when there was not mentioned in the I-Scan user manual. In column number five in table 4.4 as forces found by using Matlab multiplied whit

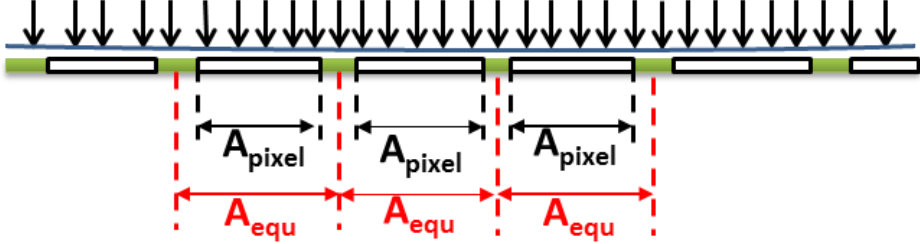the relationship between the equivalent area and pixel area.

Figure 4.6: Definition of contact area to calculate pressure.

Table 4.4: Results from hammer impact tests.

Test number	Stroke number	Tip color	Cal. range [N]	F_{I-Scan} [N]	F_{Matlab} [N]	$F_{Matlab} \times \frac{A_{equ}}{A_{pixel}}$ [N]	F_{Hammer} [N]
1	1	Orange	50- 774	242.4	283.5	331.6	1342
	2			38.1	44.45	51.86	1788
	3			161.4	189.2	221.8	2087
	4			113.9	133.3	156	2095
3	1	Orange	1306-2394	1035.4	1231	1464	1565
	2			-	-	-	1792
	3			1345.6	1590	1880	1563
	4			1768	2095	2482	2102
4	1	Orange	1306-2394	111.7	1303	1527	2071
	2			80.8	94.73	111.1	2016
	3			16.0	18.87	22.26	2172
	4			1129.7	1325	1553	1882
5	1	Red	1306-2394	385.8	452.3	530.2	4340
	2			385.8	452.3	530.2	4340
	3			61.2	71.82	84.29	2634
	4			-	-	-	4369

Forces recorded by the hammer and the tactile sensor for hammer impact number 3.1 was compared and illustrated in figure 4.7. It is important to notice that time synchronization between the sensor and the hammer was not preformed. The large difference in recorded peak force indicated that the tactile sensor failed in reconstructing the impact and therefor were time synchronization evaluated to be unnecessary.
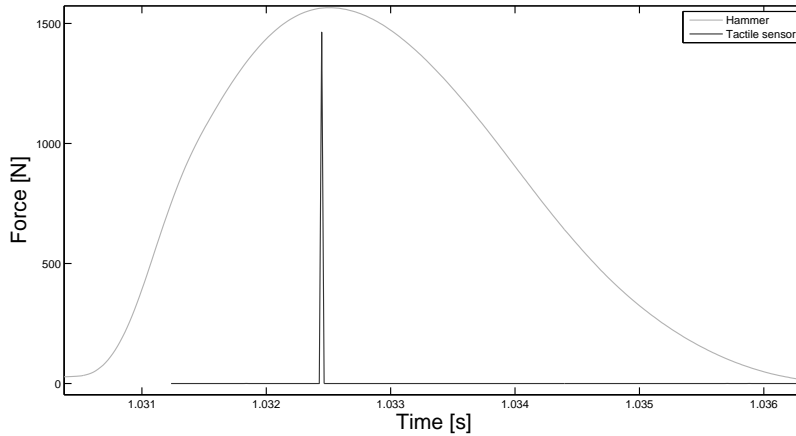
34

Figure 4.7: Time history of the measured hammer impact versus the reconstructed force obtained from the tactile sensor. Test 3.1.

Discussion; Reconstruction of a Hammer Impact

Tekscan's calibration device mentioned in chapter three, was not available during these impact tests. Therefor, calibration files were made by using weight bars. These weights were not intended to be used in scientific experiments and have therefore not very good accuracy. A machine consisting of a loading cell and having the opportunity to maintain constant load over a certain time would have decreased this error in the calibration file and would therefore have been preferred. Such apparatus was not available at NTNU when hammer impact test were performed. Different materials were tested. Both steel and wooden panels were giving an uneven pressure distribution over the loaded area. After several attempts, plexiglas was found to be a good material to use during calibration of the sensor. The material is not to stiff and gave a satisfying flexibility to the sensor template.

From impactor excitation tests conducted was a reconstruction of a hammer impulse found to be difficult with a tactile sensor recording with a frequency of 100 Hz. Both in test number three and five are one of four strokes not registered by the tactile sensor. With a recording frequency of 100 Hz are the sensor sampling every 0.01 seconds. From section 4.4.1 was a hammer impact given to last less than one microsecond dependent on the flexibility of the contact surface. This indicates that there was a good possibility that the sensor not would register an impact, with use of a recording frequency of 100 Hz. Improved results would most likely have been found with a higher recording frequency. This is not tested when equipment with higher recording capacity was not available at NTNU.

Hammer impact recordings and tactile data were closely compared in all four tests.

Test number three proved to be best reconstructed by the sensor, except stroke number two which was not registered at all by the tactile sensor. Calibration file used in test three ranged from 1306 N to 2394 N. Smaller errors in this test compared to test number one may be related to where the recorded loads were within this range. In test number one was the hammer force in the same range as test number three, but calibration file number two was used on this test. From table 4.4 may there be seen that the tactile sensor gives a larger error in this case. As mentioned in chapter three, a saved recording may be replaced by using a different calibration file. In this case calibration file number two was tested on series number three. This gave lower force values and a larger error between the tactile sensor recordings and the force recorded by the impact hammer. This indicates that calibration of the sensor is an important part of an experiment where a tactile sensor is used. However when it is possible to change the calibration file and regulate the sensitivity and the loading range after conducting the experiment are there not really important to have a good calibration file before the experiment are preformed. By using various calibration files may higher accuracy or sensitivity in a range be found. The force development through the experiment can be used to make a better calibration file. In test series number three should calibration file number one be relatively good when the calibration load range was within respectively 20 % and 80 % of maximum load. Lower force values were found when using calibration file two on series number three. Instead of using a recalibrating file to calibrate the sensor after the conducted experiment have other solutions been used at data from former experiments. Sodhi (2000), calibrated the tactile sensor by matching the total force from the tactile sensor with forces recorded by a load cell at the time of highest force. In that case were there found good agreement between the two data sets, and discrepancies may be explained by the noise in the tactile sensor data (Sodhi, 2000). This method has not been used during these hammer excitations.

Although the tactile sensor failed in reconstructing a hammer impact, it does not mean that tactile sensors can't be used to investigating an ice crushing event. The accuracy of the reconstruction will depend on time needed to break down an ice mineral and the flexibility of the structure. Since a brittle crushing process are taking place at higher velocities than intermittent crushing, should this laboratory tests indicates that a tactile sensor will better reconstruct an intermittent crushing event than a brittle event.

4.2 Recalibration of Tactile Sensor Data for Test Series 4300 and 3100 Recorded at HSVA

Due to the possibility to recalibrate the sensor are there not required to know the approximately maximum load before testing. New calibration files for test 4300 have been made in various loading ranges with different sensitivity and saturation to investigate how this effects the pressure distribution and load output given by

the tactile sensor. Developing new and better calibration files requires first of all an understanding of how the sensitivity are changing the output given by the sensor. Figure 3.7 in section 3.3.2 illustrating the relationship between measured pressure range and sensitivity, show that a lower sensitivity brings high saturation pressure and opposite. This indicates that when recalibrating a recorded test series where the calibration loads are the same, but changed the sensitivity would give different outputs. This has been tested. Figure 4.8 show a blue line drawn from data recorded by a load cell. In the same picture are output data from the tactile sensor using the initial calibration file colored gray and output using a recalibration file colored black. In both calibration files are the same pressure applied, but the sensitivity is different (see table 4.5). As may be expected from figure 3.7 was a higher sensitivity giving a lower pressure.

Table 4.5: Input parameters used during testing of effects of changed sensitivity.

Calibration file name	Pressure 1 [kPa]	Pressure 2 [kPa]	Sensitivity
Origional calibration file	1000	1600	S-18
New calibration file	1000	16000	S-24
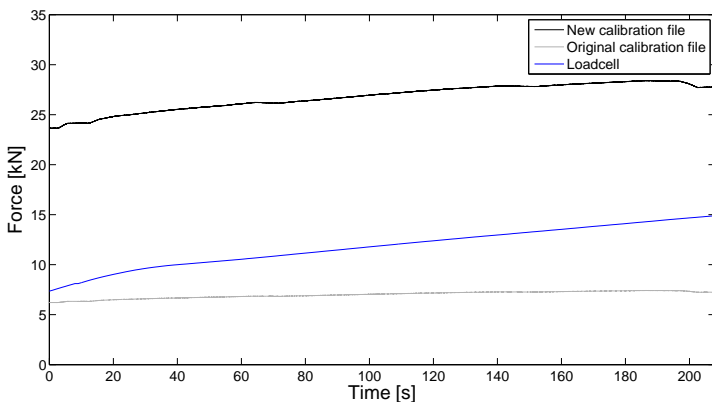
Figure 4.8: Illustration of how adjustments in sensitivity changes output from tactile data.

An oedometer loaded with weight bars as seen in figure 4.14b, and an axial press were used to find appropriate calibration files for test 4300. Files found by using the oedometer to load a 7.2 cm in diameter cylinder gave pressure in a much lower range than required for test 4300. A pressure device with higher capacity was needed. A Geonor press and a load cell with a loading capacity of 50 tons, was used to obtain the required pressure. Calibration files conducted with *Geonor 50* are listed in table 4.6 and if needed found at the *k:\Faglig\Faggruppe MB* server. This calibration files may also be appropriate for other test series from the DIIV test campaign. Force output given by the tactile sensor with different calibration

files have been compared to time- history plots found by scaling data from the accelerometer and strain gauges attached on the indenter.

Table 4.6: Calibration files made for test series recorded at HSVA.

File name	Loading area $[m^2]$	Force1 [N]	Force2 [N]	Sensitivity
cal-1-D7.2		8000	23600	S-21
cal-2-D7.2		4600	18400	S-24
cal-3-D7.2		3000	12000	S-24
cal-4-D7.2		8000	32000	S-11
cal-5-D7.2	0.004072	5000	20000	S-24
cal-6-D7.2		6500	22000	S-24
cal-7-D7.2		6500	22900	S-22
cal-8-D7.2		6500	22000	S-23
cal-1-D15		4000	16000	S-28
cal-2-D15		6000	24000	S-31
cal-3-D15		3000	12000	S-33
cal-4-D15	0.017671	8000	32000	S-23
cal-5-D15		10000	20000	S-29
cal-6-D15		3000	10000	S-33
cal-7-D15		8000	32000	S-26

Maximum force during test 4300 was approximately 21 kN. From the recommendations given by the Tekscan user manual should calibration loads then be approximately 4200 N and 16800 N. In theory should cal-2-D7.2 or cal-1-D15 give satisfying results. However when preparing a calibration file is pressure per area important, and not the force it self which can be interpreted by the user's guide. Therefore would the required pressure per area easier be reached with a reduced calibration area. In the user's manual is it recommended that 25 % of the sensing area should be loaded during calibration, to do this was a 15 cm in diameter cylinder required. To meet this requirement, much higher force needed to be applied to the sensor to achieve the same pressure per area as by loading a 7.2 cm diameter cylinder.

Approximately 35 calibration files was made before a necessarily combination of force, sensitivity and saturation were found for test 4300. Only some of them are mentioned in this thesis. Cal-8-D7.2 turns out to be a good calibration file to use at test 4300. Time-history plots found from scaling are seen in figure 4.9b. Comparison of time-history plots from the tactile sensor and plots found from scaling show good agreement over the whole time series. Figure 4.9a shows how cal-8-D7.2 change the force plot compared to the initial calibration file.

New calibration files were also tried to be found for test series 3100. cal-3-D7.2 gave satisfying results when considering the force development over time, compared to findings from scaled results. However the pressure distribution were not changed and there seemed to have a "cut-off" pressure. The problem appears to be that test 3100 where recorded with a high sensitivity (S-32), giving a low saturation

pressure. A calibration file with lower saturation will not be able to reconstruct a higher pressure then what have been recorded. This meaning, when recording an experiment should a low saturation be chosen at the initial calibration file, then a recalibration can be used more effectively.

An appropriate calibration file will reduce the uncertainty using scaling to estimated forces action on the indenter, however preparing new calibration files require some work and available equipment.
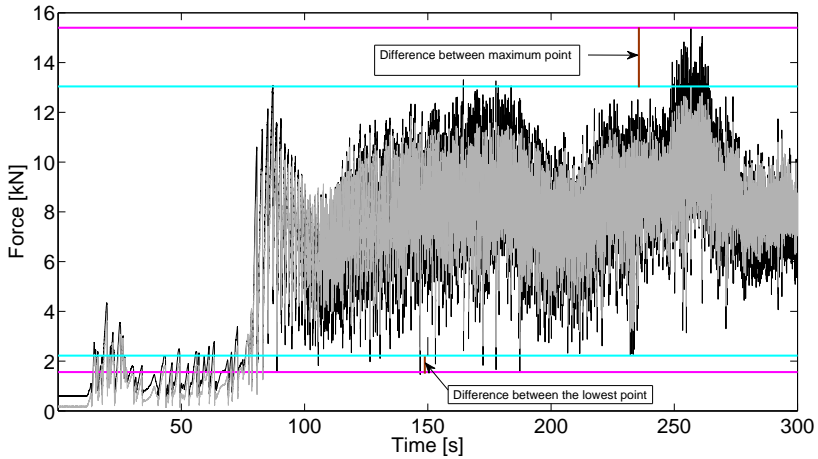
(a) Time history plot for test 4300 found by recalibration.
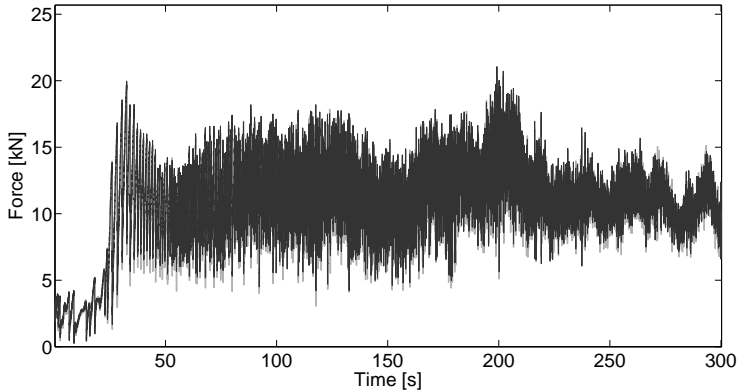
(b) Time-history plot for test 4300 found by scaling.

Figure 4.9: Force development in test 4300 found with different methods.

4.3 Compression Test of Ice

When the tactile sensor failed in reconstructing a hammer excitation, it is natural to raise the question if the sensor is able to reconstruct fast changes during an ice crushing process. To investigate this further, an axial compression test of ice was conducted. A simple compression test would give us the ability to see how the tactile sensor data was changing through the crushing proses in relation to what was observed and recorded by a load cell. Again different calibrations files were made to see how the pressure trends were changing with adjustments in sensitivity, saturation and force range.

4.3.1 Experimental Setup and Procedure

The compressive test were carried out in *NTNU- Geotechnical laboratory* on the 25th of April 2014. Air temperature in the laboratory where the test took place was around 21 °C (Normal room temperature). Since ice properties were not examined, was neither the temperature of ice or surroundings controlled during the experiment. Saline ice made in *FRYSISII* at the *NTNU- ice laboratory*, was placed into a pressure machine of the brand *Geonor 50*. The compression machine was connected to a load cell with a capacity of 50 tons. The pressure device was produced by *HBM Wägetechnik Germany*. By moving the lower piston agents the load cell at the top was the ice sample compressed with a constant velocity. Input parameters given in table 4.7 was used in the control program *Stiv-triax*:

Table 4.7: Essential input parameters in Stiv-triax.

Recording frequency	Deformation	Velocity
10 Hz	65 mm	180 mm/h

Due to the lower pistons movement restriction at 6,5 cm, two POM cylinders were used to lift the ice sample closer to the load cell. To reducing melting of the sample, the POM cylinder close to the ice were cooled down in the *NTNU- cold lab* before use. The ice sample was approximately 11 cm from the top to the bottom. A peak where formed at the top of the sample to gain higher pressure and hopefully manages to get a brittle fracture in the ice. Ice geometry and dimensions are seen in figure 4.10. The tactile sensor was placed directly under the load cell, and held carefully on both sides. Test setup may be seen in figure 4.11b. The tactile sensor was recording with a frequency of 100 Hz. Recording frequency and velocity input were restricted by the capacity of the apparatus. Higher velocities could stop the engine in the middle of the test. Due to low compression rates and fast melting, the ice behaved in a ductile manner. Despite the opportunity for the engine to stop, the test was stopped after 8 minutes to increase the velocity of the pistol from 180 mm/h to 300 mm/h.

In an attempt to gain a calibration file that would be high enough to register
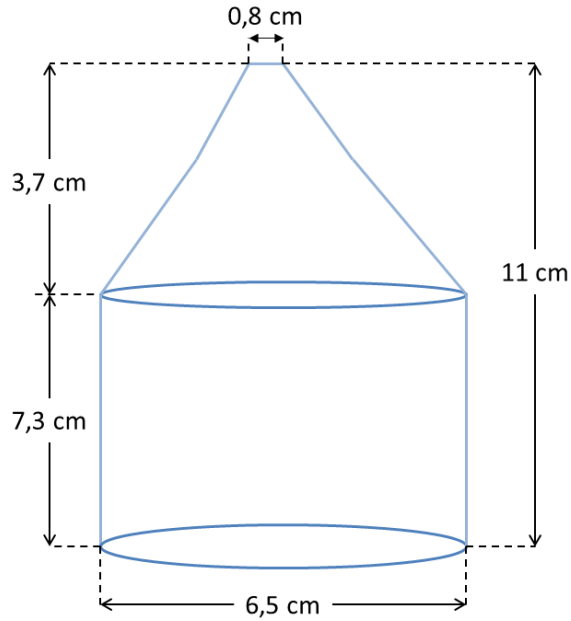
Figure 4.10: Geometry and shape of the ice sample. (Not drawn in scale.)

pressure in the range 0.2 to 3 MPa we used smaller contact area than recommended by the user manual. A 3 cm in diameter POM cylinder where used to make two calibration files. Details are given in table 4.8. Calibrations were conducted with the *Geonor 50* compression machine. The initial file was calibrated with a sensitivity S-6, so higher sensitivity files could be used for recalibration and still obtain an acceptable pressure distribution. The idea was to create calibration files with higher force and better sensitivity, but during the second recalibration the black plastic expanded and POM cylinder slid out. Recalibration at such high pressure ranges was proved to be difficult with the equipment available and therefor the experiment was not repeated. In stead, a calibration file made for test series 4300 (cal-3-ice) was found to be usable for this experiment.

Table 4.8: Calibration files used for compression test of ice.

File name	Loading area $[mm^2]$	Force1 [N]	Force2 [N]	Pressure1 [kPa]	Pressure2 [kPa]	Sensitivity
cal-1-ice	706,85	6000	15000	8488	21220	S-6
cal-2-ice		1500	6000	2122	8488	S-20
cal-3-ice	4071	8000	31500	1965	7860	S-11

(a) Calibration with 3 cm POM cylinder.

(b) Test setup during compression test.

(c) Compressed and melted ice sample.
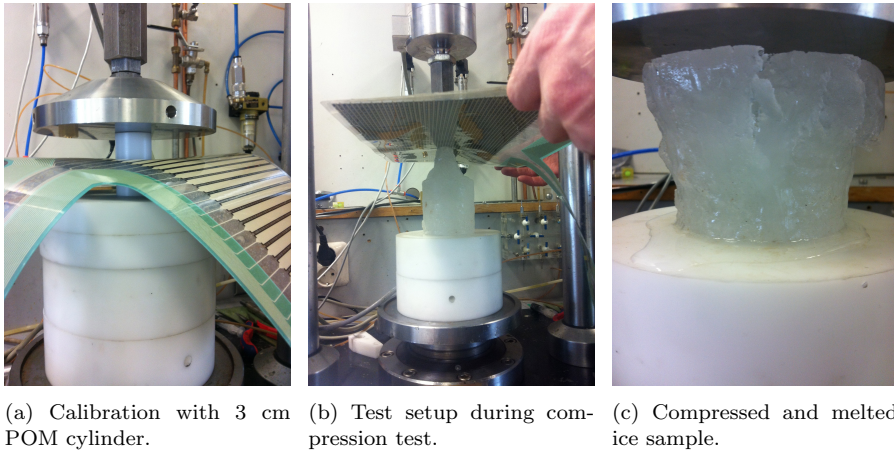
Figure 4.11: Compression test of ice.

4.3.2 Results and Discussion; Compression Test of Ice

Time-history plot obtained for the sample during a time step when the velocity of the piston was 300 mm/s is shown in figure 4.12. Data recorded from the load cell is illustrated with the blue line, data with the initial calibration file illustrated in black and tactile data with calibration file number two and three are illustrated in gray and red.
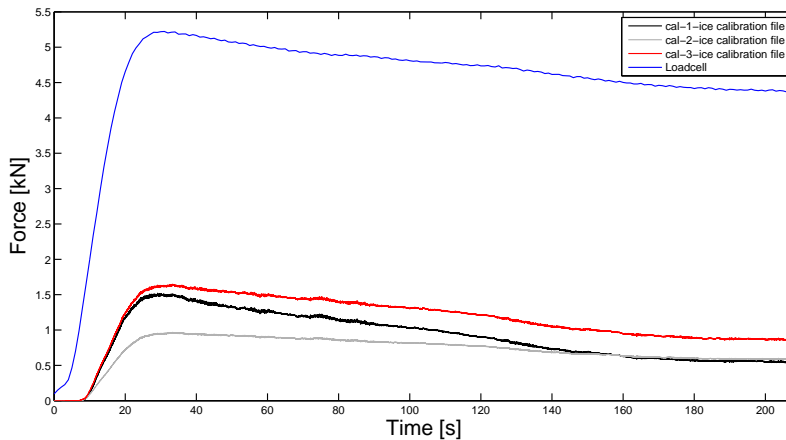
Figure 4.12: Time-history plots recorded by the tactile sensor and a load cell during compression test.

Aim of this compression test was to see if the tactile sensor would be able to register

pressure changes during fast events or brittle fracture in an ice structure. Due to high temperature in the surroundings, heat from the load cell and low compression velocities, the ice sample melted fast and the ice gained a clear ductile behavior. Regardless of melting and ductile behavior, the piston velocity was increased and the compression test completed. When the ice sample started to flake and a fracture started to propagate was this also observed from the tactile sensor data (see figure 4.13). A line with lower pressure could be observed to propagate over the ice sample before this part of ice unfastened. Figure 4.11c shows how the ice sample melted after finishing the test. To gain a brittle fracture, the compression experiment should have been conducted in a cold lab with higher strain-rates. However in general we found a good correlation in trend between data curves obtained from the load cell and the tactile data.
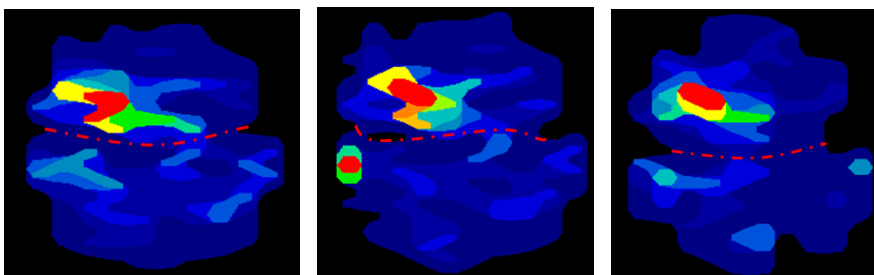
Figure 4.13: Crack development in ice during compression test.

4.4 Summary of Calibration and Testing of the Tactile Sensor

The tactile sensor failed to reconstruct the force from a hammer excitation. Based on this we preformed a compression test of ice. The main intention with the compression test was to gain a quick failure in the ice, and see if the sensor was able to record this. However, the ice tended to gain a ductile behavior and no suddenly faults were triggered. Satisfying agreement between the load cell and tactile data were found during ductile failure. Due to poor test conditions were not additional tests conducted.

Different types of loading material were tested to obtain flexibility to the sample template. Also even pressure distributions over the loaded area were evaluated. In order to obtain an even pressure distribution have POM with black plastic and plexiglas found to be good materials to use.

Different types of calibration devises have been used in order to make calibration files giving sufficiently good results. Firs calibration files were made for the hammer impact test. They were made manual with weight bars. This method was heavy and time demanding. Relative low pressure was obtained with manly kilograms

weights. In order to use less weight, but maintain the pressure was an oedometer tested. Still were not the required pressure achieved. At the end was a 50 tons Geonor compression device used to achieve the required pressure.

New calibration files for test 4300 and 3100 have been made. There have been found that an initial calibration file should have low saturation in order to avoid a "curt-of" pressure. During preparation of calibration files for the compression test were this taken into account.

An increase in load output when using cal-3-ice as calibration file during the ice crushing recording confirms what is seen in figure 3.7. High sensitivity increases force outputs. If higher sensitivity had been used on file cal-1-ice the loading output would be even higher.

Regardless of calibration files was the tactile sensor failing reconstructing a hammer impact. Files made by use of the Geonor 50 apparatus were used to recalibrate impact recording. This gave changes in force output, but not larger accuracy.

4.4.1 Practical Challenges

Trends of effective pressure during ice- structure interaction for both small, medium and large-scale testes are found in former literature. In Sodhi et al. (1998) are effective pressure found to vary in a range from 1 to 20 MPa, whereas Jefferies and Wright (1988) measured ice loads grater than 100 MN on first and multi-year ice in the Canadian Beaufort Sea. Loads of high magnitude puts demands on the tactile sensor. Based on experience from work preformed in this chapter, the following practical challenges were found to affect preparation of calibrations files for high loads.

- Loading area.

Calibrating in high pressure ranges and still have a loading area covering 25% of the sensing area, require the possibility to add high loads. If a smaller area could have been loaded would lower forces had to be inflicted, this could easily be seen from equation 2.6.

- Loading device.

Even tough calibration doesn't require much equipment are loads in high ranges often not available in test environments where the sensor are used for ice-structure interaction. Preferably should the device be constructed so the tactile sensor template does not need to be folded as seen in figure 4.14b. Folding the template may give error in the force distribution and damage the sensor.
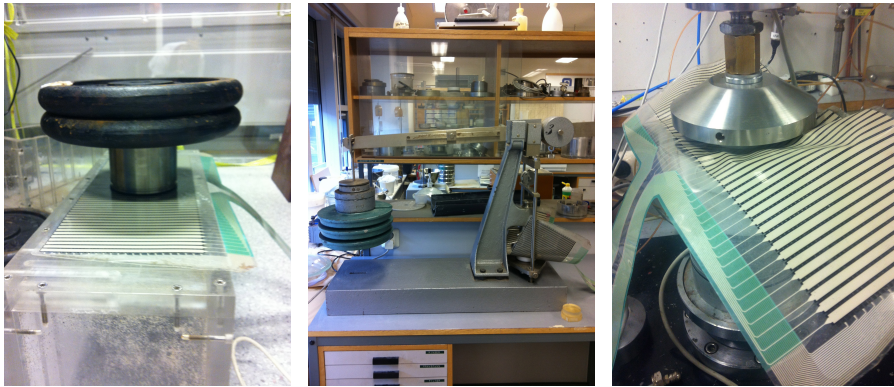
(a) Calibration files con-
ducted using weights.

(b) Tactile sensor loaded by
using a odometer.

(c) Tactile sensor loaded by
using a Triax.

Figure 4.14: Examples of different loading techniques.

- Choice of material during calibration.

It have been mentioned earlier that the choice of material used during calibration
was important to gain an even pressure distribution over the loaded area. An
inflexible material as steel may give a pressure distribution as seen in figure 3.9a.
However when calibrating in large pressure reneges is it also important that the
material used above and below the template dos not extend to much. To obtain
some flexibility during calibration was plastic used under the sensor template and
above the *POM*. During large pressure did this black plastic expand and started
to fold as seen in figure 4.14c. This damaged the sensor template.

Chapter 5

Qualitative and Quantitative Analyses of Data From Test Series

Tactile sensor data from two test series recorded during the Deciphering Ice Induced Vibration (DIIV) test campaign at HSVA in 2011 have been analyzed both in time and frequency domain. Respectively test 4300 and 3100. For a description of the test setup and other parameters regarding these test series see Pedersen (2012). Data recorded by the tactile sensor were converted into an AIIC file and further analyzed in Matlab. I-Scan where used as an external control. In both test series the sensor area was divided into thirteen sections, with equal curve length (see figure 5.1). Numbers of sections were selected based on a combination of satisfying and readable results.
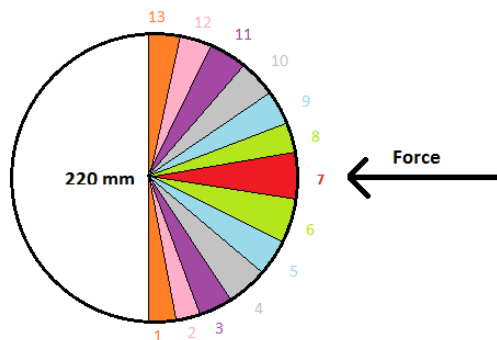
Figure 5.1: Sensor area divided into sections.

5.1 Test Series 4300

The analyzed time sequence in test 4300 covers velocities between 30 mm/s and 200 mm/s. Ice velocities were increased stepwise with time as displayed in figure 5.2.
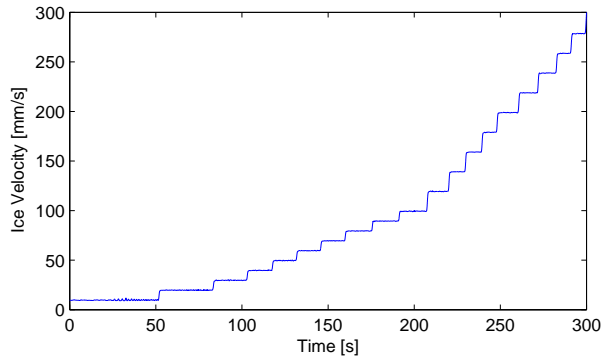
Figure 5.2: Velocity changes with time for test 4300.

In order to assume a random stationary process time series 4300 was divided into sub-events as seen in table 5.1.

Table 5.1: Sub-events during test 4300.

Sub event number	Velocity step
1	30 mm/s
2	40 mm/s
3	50 mm/s
4	60 mm/s
5	70 mm/s
6	80 mm/s
7	90 mm/s
8	100 mm/s
9	200 mm/s

5.1.1 Time Domain Analysis of Test Series 4300

Local forces within thirteen sections were analyzed in time domain. Forces in each section were compared and correlation coefficients matrixes found. Correlation coefficient matrix in 3-D bar chart and 2-D contour plots for nine sub-events, with velocities ranging from 30 mm/s to 200 mm/s are presented in this thesis. Transition speeds between intermittent and continuous brittle crushing are typically found in velocity ranges below 100 mm/s. Above 100 mm/s continuous brittle crushing usually dominates (ISO, 2010). Due to this, manly velocities ranging from 30 mm/s to 100 mm/s were emphasized. In addition may global force plots, local force plots and correlation plots for the 200 mm/s time interval be seen in Appendix C. Due to the large amount of data, only representative events are presented below. For enthusiast information from remaining velocity intervals can be found in Appendix C.

Tactile sensors only measure normal forces. Shear forces were estimated as explained in section 2.3.1. by assuming an ice-aluminum foil friction coefficient of 0,027 (Sergiy Sukhorukov and Wenjun Lu, Personal communication). Local and global forces illustrated in this chapter includes shear forces.

Sub-Event One: 30 mm/s

A typical intermittent crushing regime is observed from the global force plot in figure 5.3. In accordance to section 2.1.2 forces was seen to build up over time, before they reached a maximum value and suddenly dropped to a value close to zero. Figures 5.4 and 5.5 shows similar patterns for local forces in all sections except of sections one, two, twelve and thirteen. Section one was exposed to higher peak forces than section thirteen. In both cases small and random force patterns were observed. Force recordings in figure 5.4 show simultaneously occurrences of peak forces at different locations around the cylinder.
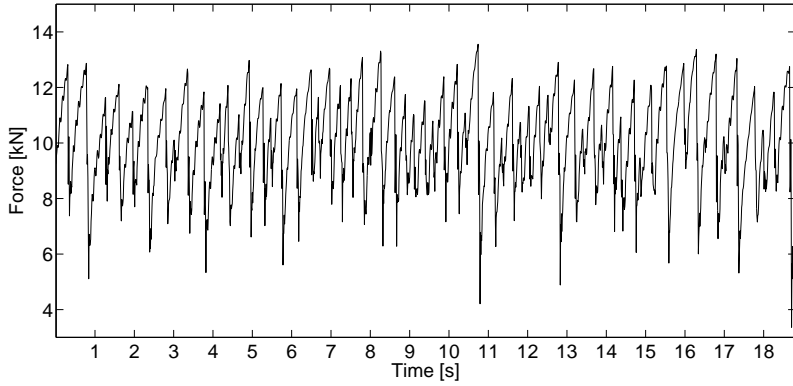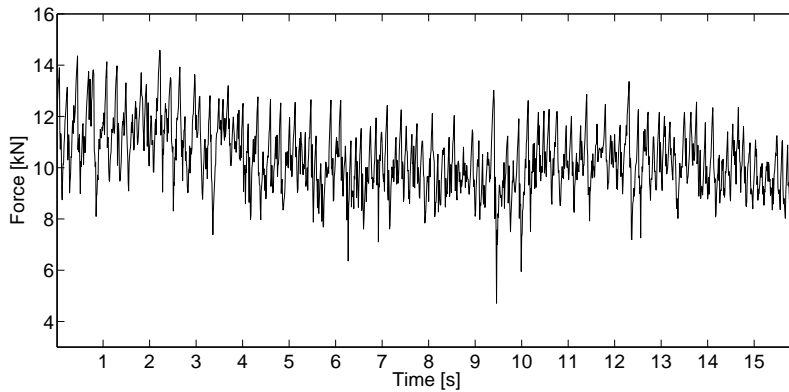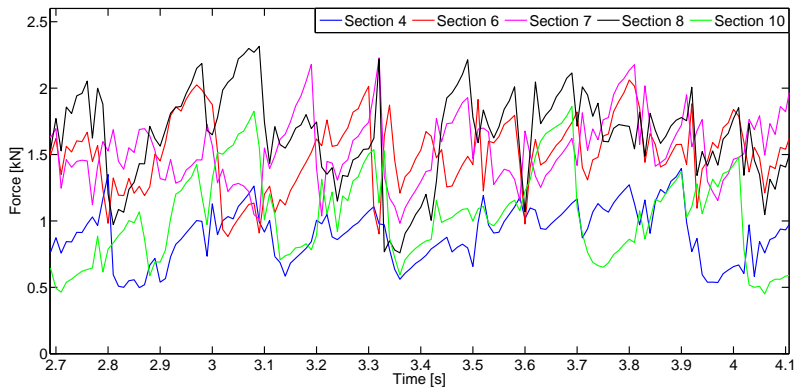
Figure 5.3: Global force within sub-event one.
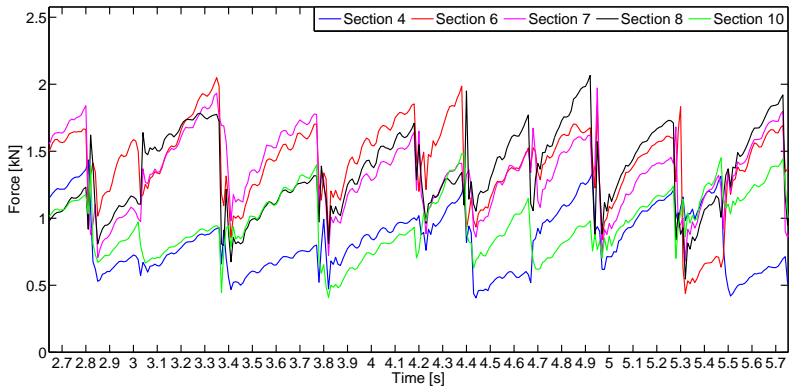
Figure 5.4: Local forces within a small time window of observation for sections 4,6,7,8 and 10 in sub-event one.
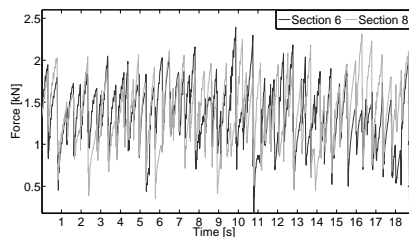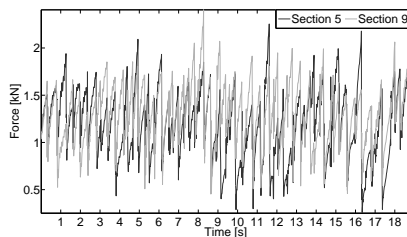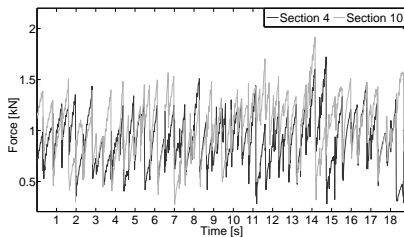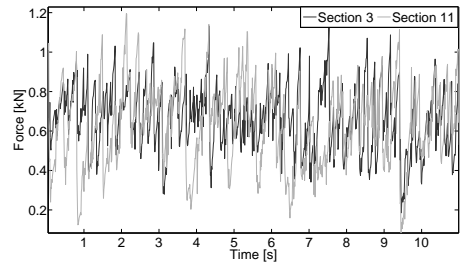
49

(a) Section six and eight.

(b) Section five and nine.

(c) Section four and ten.
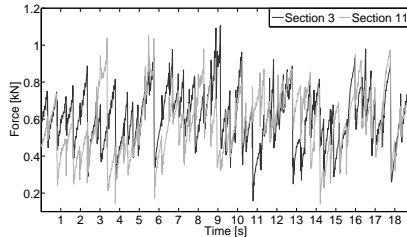
(d) Section three and eleven.
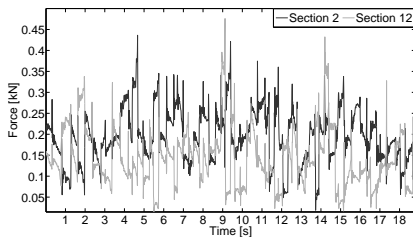
(e) Section two and twelve.
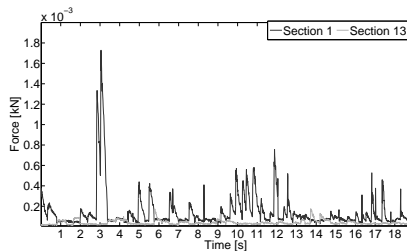
(f) Section one and thirteen.

Figure 5.5: Local forces in symmetrical sections around the middle of the indenter.

Figure 5.6a displays a bar representation of the correlation matrix for sub-event one. Self-correlations are depicted along the diagonal. Pillars at the non-diagonal term indicate cross-correlations between sections. Figure 5.6a show a self-correlation equal to one and lower values for cross-correlations. Directly adjacent panels showed to have higher cross-correlation than distant sections and symmetrical sections. In this context, symmetrical refers to the symmetry around the center of the tactile sensor. Sections close to the middle of the sensor tended to have higher cross correlation with surrounding panels, than sections near the edges. Sections three, six and seven shows better cross correlation with sections further apart then any of the other sections. In addition sections three, six and seven were showing low cross correlations between immediately adjacent sections.

Figure 5.6b provide an alternative graphical presentation of figure 5.6a. Red color indicates high correlation and blue low correlation. This contour plot shows that the correlation matrix is symmetrical around the diagonal. Symmetry indicates that correlations between for example S1 (sections one) and S2 (section two) are

the same as S2 and S1. Any asymmetries from this are most likely artifacts of plotting routine.
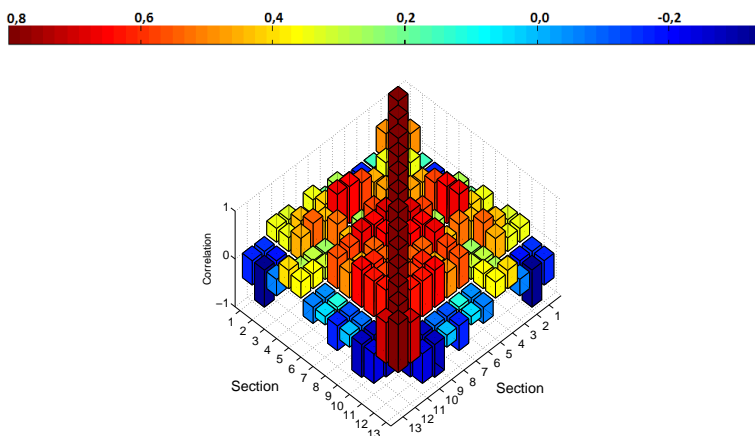

(a) Correlation coefficient matrix 3-D bar chart.
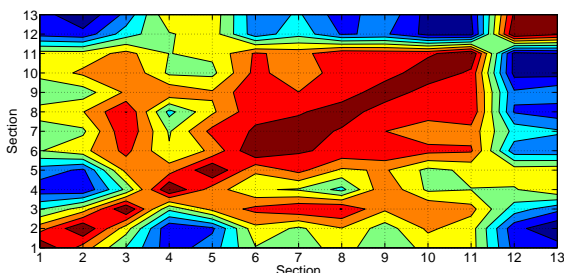
(b) Correlation coefficient contour plot.

Figure 5.6: Panel correlations during a 30 mm/s velocity interval.

Sub-Event Eight: 100 mm/s

Force distributions within sub-event eight indicated a dominating continuous brittle crushing regime. Time-history plot of the global force was random orientated, unlike the characteristic sawtooth pattern indicating an intermittent crushing regime. Global force for velocity interval 100 mm/s may be seen in figure 5.7.

Figure 5.8 and 5.9 shows time-history plots of local forces. A random force development was observed with few signs of synchronizations between sections. In contrast to sub-event one, peak forces occurred randomly within sections. Comparison between section ten and four seen in figure 5.9c shows some similar force reductions during the time window, but in general section ten was exposed to larger forces than section four. The same applies for section five and nine given in figure

5.9b. Sections six and eight have virtually the same force trends compared to local forces in other section within this time window. However, also here differences were found. In general, local forces seemed to be indicating a continuous brittle crushing pattern. Except from section one and thirteen where no indications of either intermittent or brittle crushing was observed.


Figure 5.7: Global force within sub-event eight.

Figure 5.8: Local forces within a smaller time window of observation for sections 4,6,7,8 and 10 in sub-event eight.
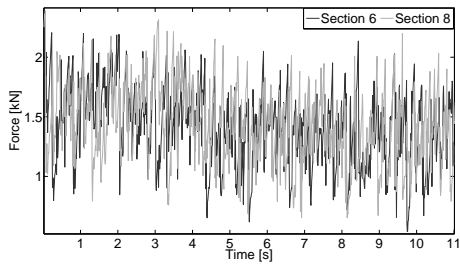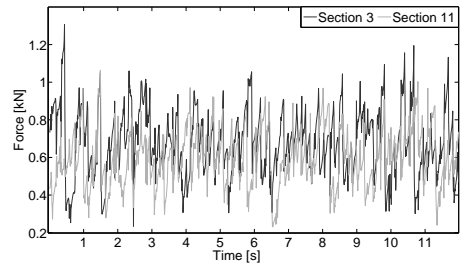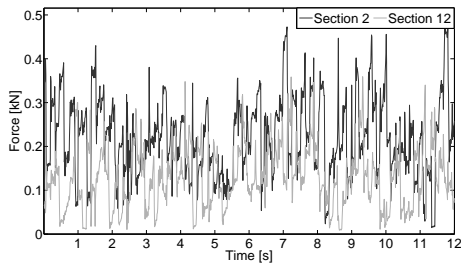
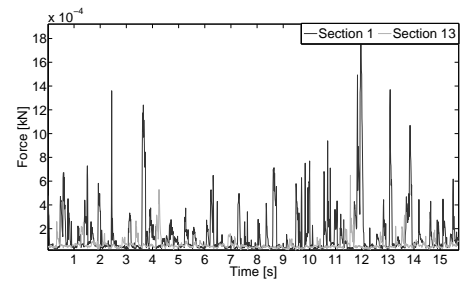(a) Section six and eight.
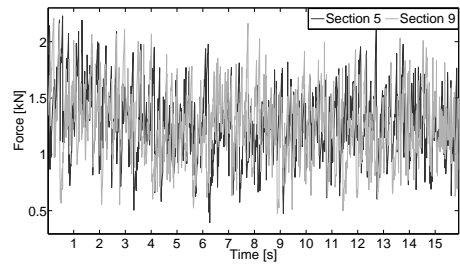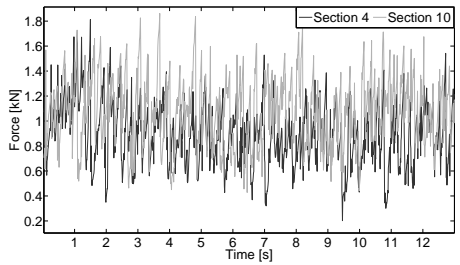
(b) Section five and nine.

(c) Section four and ten.

(d) Section three and eleven.
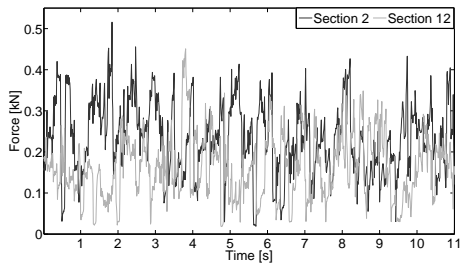
(e) Section two and twelve.
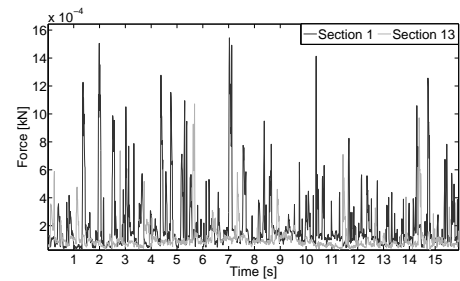
(f) Section one and thirteen.

Figure 5.9: Local forces in symmetrical sections around the middle of the indenter.

53

Figure 5.10a shows higher correlation between immediately adjacent sections than distant panels. This confirm observations found from local force plots in figures 5.8 and 5.9. However in figure 5.10a high correlation may be seen between section ten and three and section four and twelve. Higher correlations were not observed from local force plots. Figure 5.10b indicates high self correlation ($r_{ij} = 1$). Compared to figure 5.6b, this contour plot shows lower correlation with immediately adjacent panels. Orange color in correlation between section ten and three as well as section four and twelve confirms what was found from figure 5.10a.
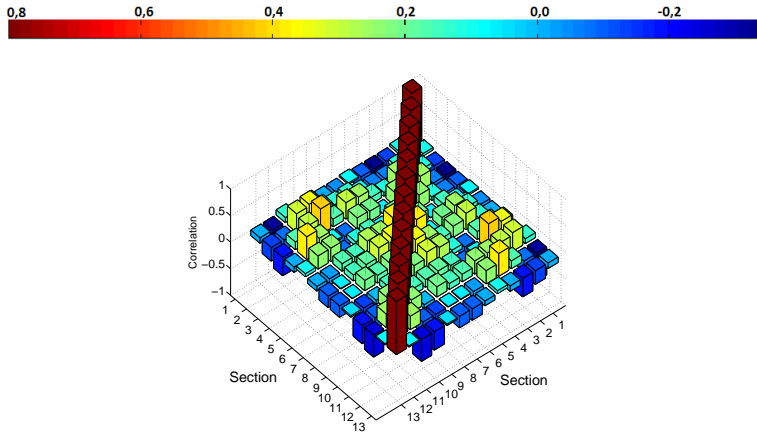
(a) Correlation coefficient matrix 3-D bar chart.
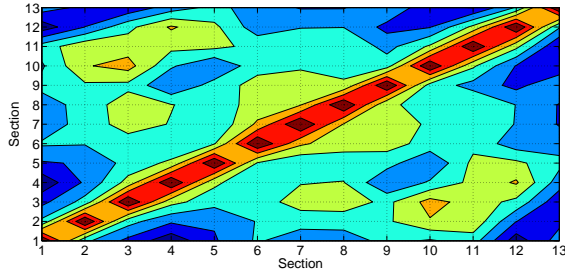
(b) Correlation coefficient contour plot.

Figure 5.10: Panel correlations during a 100 mm/s velocity interval.

Sub-Event Six: 80 mm/s

Time-history plots of both local and global forces within sub-event seven (90 mm/s) seen in Appendix C showed few signs of intermittent crushing, and a brittle crushing regime seemed to dominate. Comparison of local forces shows few signs of synchronizations except from a few similarities in sections six and eight. This in contrast to sub-event five (70 mm/s), where similarities in local force pattern may be observed between section six and eight, five and nine, four and ten as well as three and seven in figure C.18. An intermittent crushing regime dominated. For further interest in sub-event seven and five see Appendix C.

A typical crushing regime was partly difficult to recognize within sub-event six (80 mm/s). Shape of the global force time-history plot appeared to have a small change six seconds within velocity interval 80 mm/s. Smaller difference between force peaks and lower values was observed after six seconds, see figure 5.11. Force developments at the beginning of sub-event six consist of peaks where a force buildup with small force drops were observed up to a maximum value. However this were also observed during velocities around 70 mm/s.
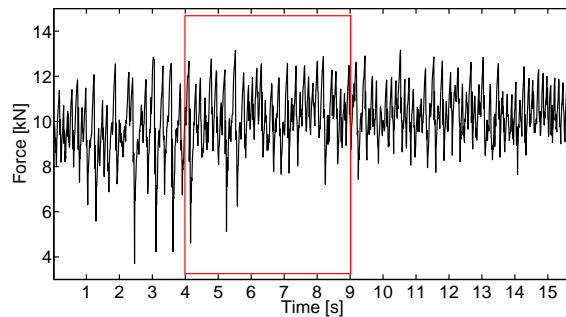
(a) Time-history plot for sub-event six.
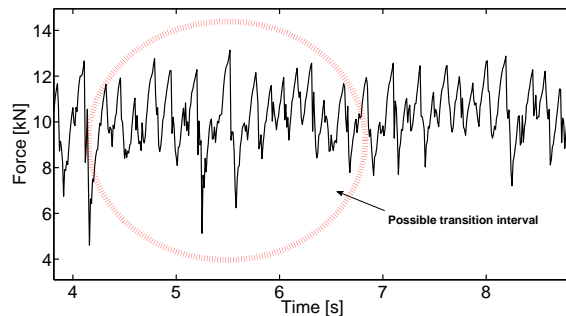
(b) Smaller tim window within sub-event six.

Figure 5.11: Global forces within sub-event six.

Time-history plots of local forces have been examined. Forces are seen in figure 5.12 and 5.13. In general, a typical intermittent force release phase was found for local forces in sections close to the edge of the sensor. Small force drops was observed in the force buildup stage when the force was growing towards a maximum value. However for sections close to the middle of the sensor an indeterminable and random pattern was observed, more like brittle crushing. Changes in force development after six seconds observed in the global force plot, may also be seen in figure 5.13b from local forces in section nine. After six seconds local force peaks in section nine propagated with higher frequencies. In figure 5.12 mark the dashed line, the area in witch a trend change was observed from the global force plot. There was not found any changes in force trends from other local forces in this time window.
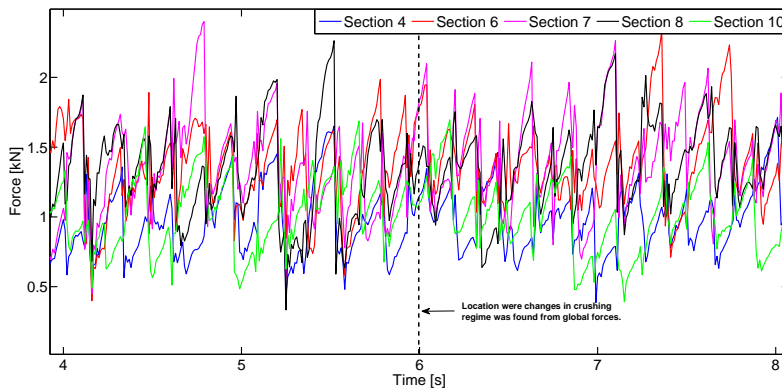
Figure 5.12: Local forces within a smaller time window of observation for sections 4,6,7,8 and 10 in sub-event six.
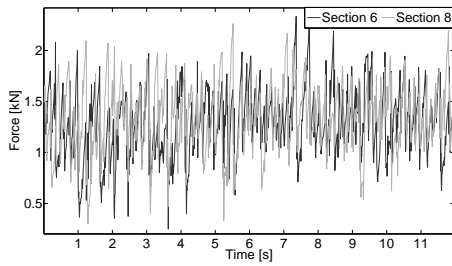
(a) Section six and eight.
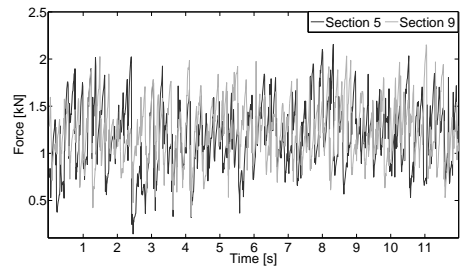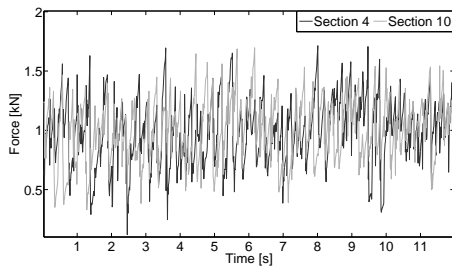
(b) Section five and nine.

(c) Section four and ten.

(d) Section three and eleven.

(e) Section two and twelve.

(f) Section one and thirteen.

Figure 5.13: Local forces in symmetrical sections around the middle of the indenter.

Figures 5.14a and 5.14b shows similar trends in correlation within sub-events one and eight; correlations between selected sections and immediately adjacent sections were stronger than distant sections. A perceptible exception was the correlation between section six and eleven. Higher correlation between sections six and eleven was also seen with orange color in the correlation coefficient matrix contour plot.
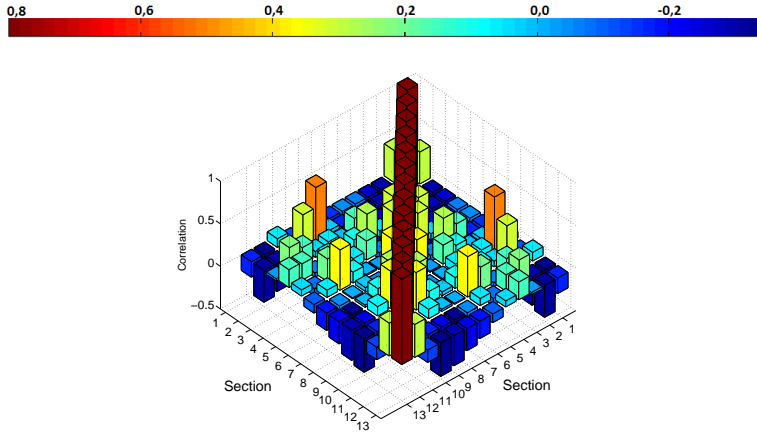
(a) Correlation coefficient matrix 3-D bar chart.
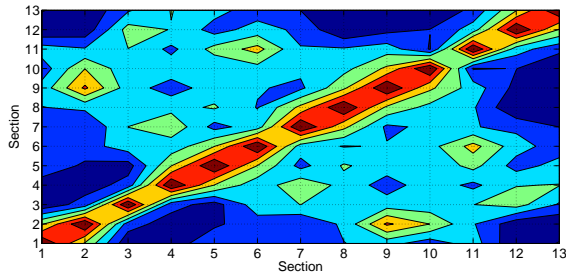
(b) Correlation coefficient contour plot.

Figure 5.14: Panel correlations during a 80 mm/s velocity interval.

5.1.2   Stochastic Dynamic Analysis of Structures; Test 4300

As mentioned in section 2.3.4 is a spectral model for forces due to ice crushing, based on theory manly applied for stationary excitation processes. Each time series was therefore divided into sub-events and stationarity assumed within each sub-event. Length of each time step analyzed ranged from 12.10 to 30.16 seconds. Average time duration within each sub-event was 16.4 seconds for time series 4300. In the following, spectral density matrixes for selected sections are given and discussed. The diagonal term of the spectral density matrix is the two-sided auto-spectral density function of the local forces in each section. Autocorrelations plots for selected sections are presented for some sub-events in time series 4300. Due to a large amount of data only some sections are presented here. Auto-spectral density functions in each section was studied, to find a pattern in dominating frequencies around the indenter, within different crushing regimes. Where frequencies are marked with a color is each color illustrating a frequency that was found in more than one section within the same sub-event. Similar colors are used in all sub-events, so each color do not represent an unique frequency.

Sub-Event One: 30 mm/s

Figure 5.15 shows spectral density matrixes for sections one, four, seven, ten and thirteen. Spectral density functions proved to have highest value in the range of low velocities, and decreased with increasing frequencies. The two sections closes to the edge on both sides of the cylinder had frequencies with lower magnitude than other sections. There again, frequencies found from auto-spectral densities in section thirteen have lower magnitudes than in section one. From auto-spectral density plots in figure 5.15, can there be seen less dynamic action close to the edges of the indenter. Spectral density plots near the edges progresses faster towards zero with increasing frequencies than what was observed for other sections. However this trend was also found in the middle of the indenter (section seven).

Sub-event one had a number of frequencies represented in different sections. A common feature of these frequencies are that they were relatively low (<4Hz), see figure 5.16. Most similarities were found between sections near the middle of the cylinder. Figure 5.16 show that sections one, two, eleven and twelve have few similar frequencies with other sections. However in section two and twelve, two similar frequencies were found. These two sections are located symmetrical around the middle of the cylinder. Recurring frequencies were recorded at multiple locations around the indenter in this sub-event. Highest resemblance were found between sections three and nine, seen in figure 5.16c and 5.16e. Five frequencies were found to be similar within these two sections, but the magnitude tended to variate. Some frequencies appeared to recur in adjacent sections, where this occurred seemed to change with number of sections implemented. When increasing the number of sections this tended to be the case more often. An example of this may be seen between sections eleven and twelve in figure 5.16f and 5.16g.
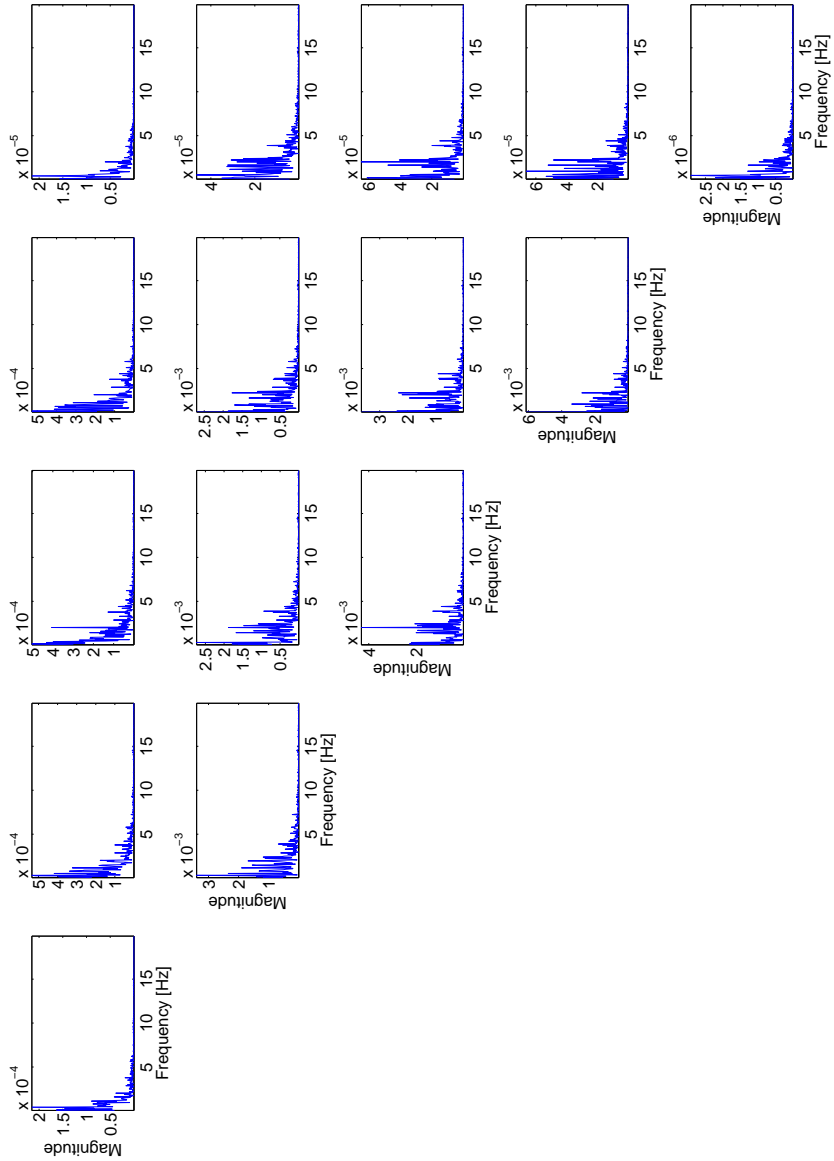
Figure 5.15: Auto- and cross-spectral density plots for sections (from the top) 1,4,7,10,13 within sub-event one.
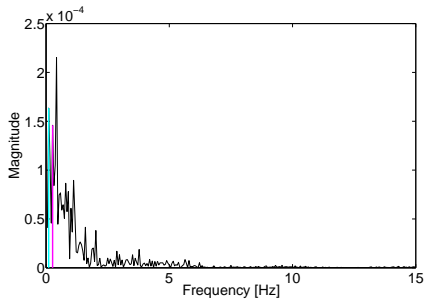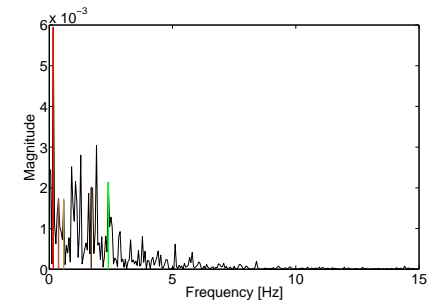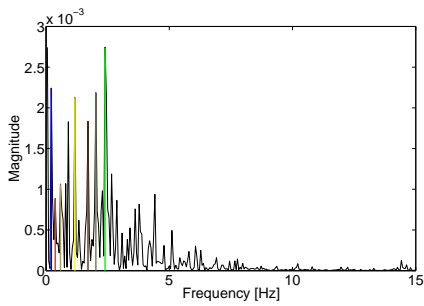
(a) Autospectral density section 1
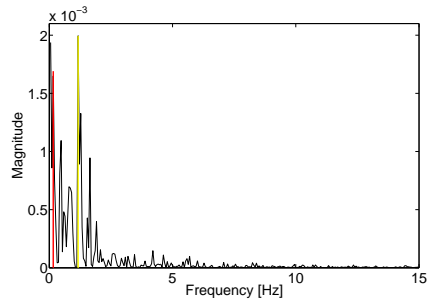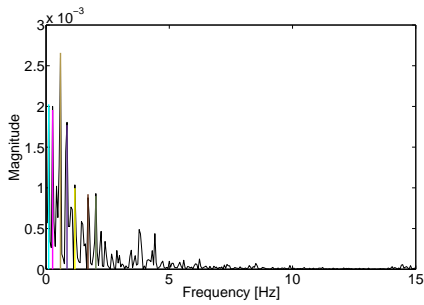
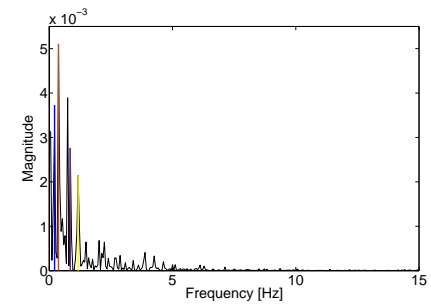(b) Autospectral density section 2
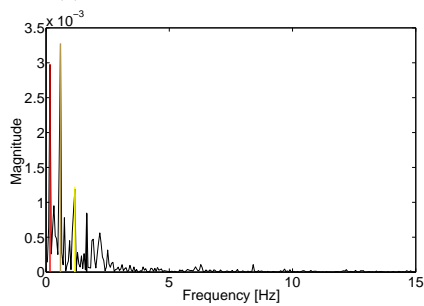
(c) Autospectral density section 3
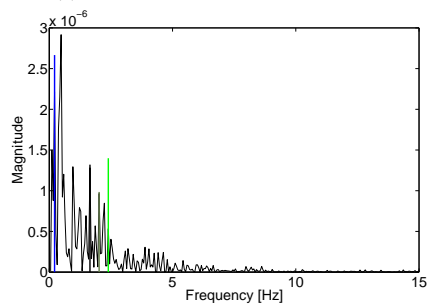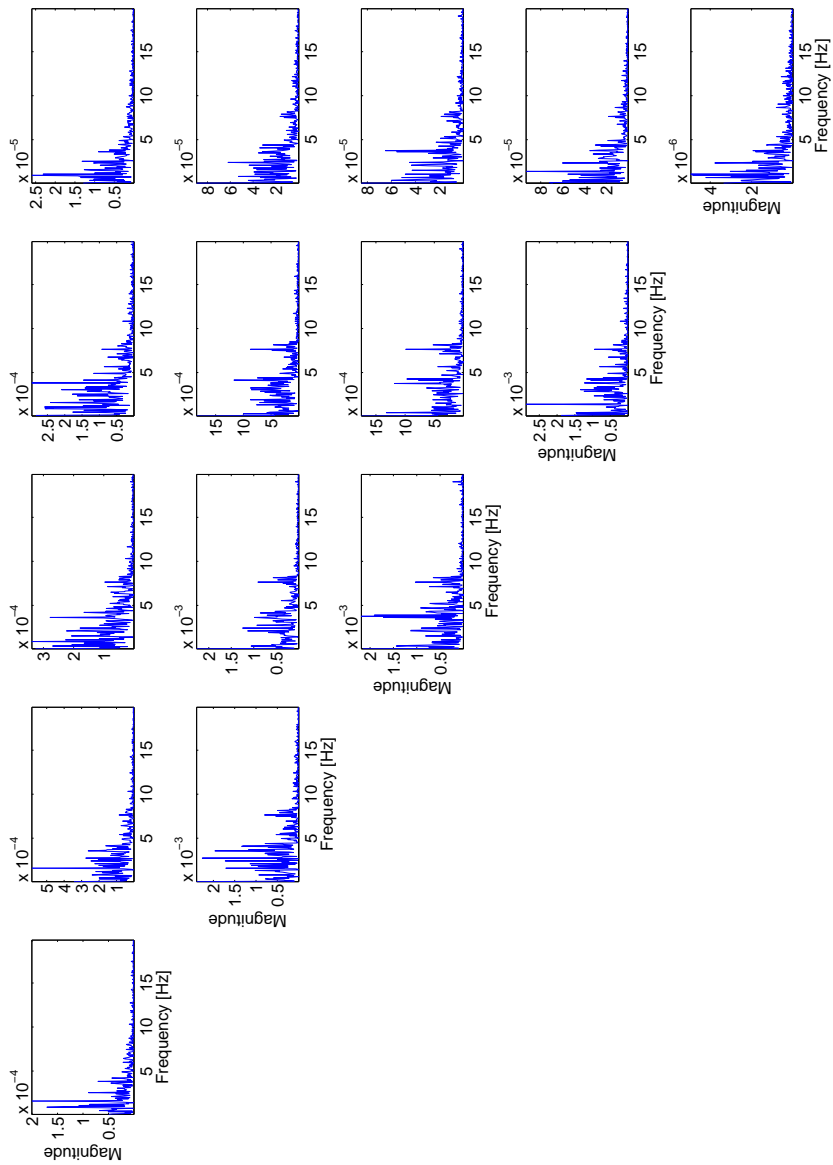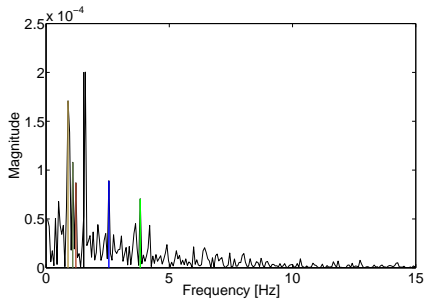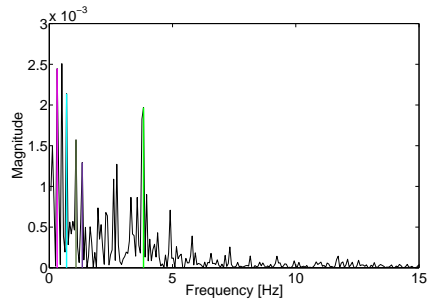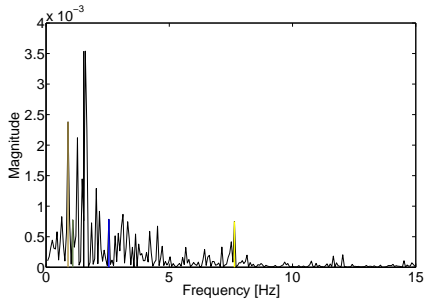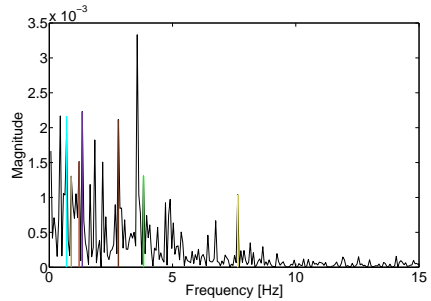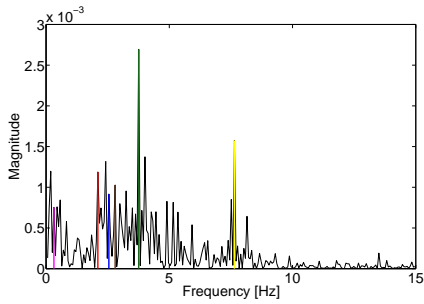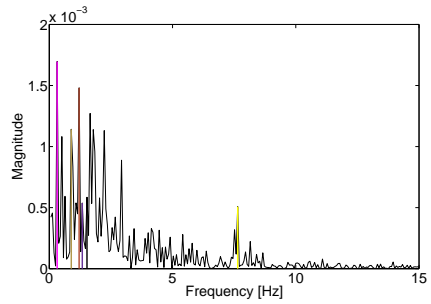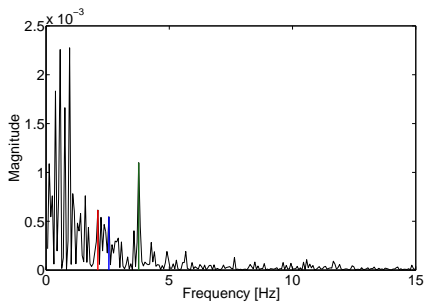
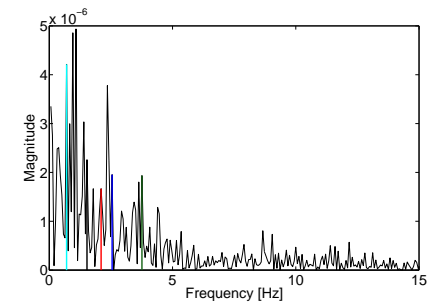(d) Autospectral density section 5

(e) Autospectral density section 9

(f) Autospectral density section 11

(g) Autospectral density section 12

(h) Autospectral density section 13

Figure 5.16: Auto-spectral density plots for selected sections within sub-event one. Similar frequencies are marked with the same color.

Sub-Event Six: 80 mm/s

Similar trends as mentioned for sub-event one was observed within sub-event six. Auto-spectral density plots for sections one, two, eleven and twelve show lower magnitude for frequencies peaks than other sections. Compared to sub-event one, figure 5.17 shows more dynamic spectral density plots. The spectral density plots tended to slower approach zero with higher frequencies than observed in figure 5.15.

Auto-spectral density plots for sections one, two, three, five, nine, eleven, twelve and thirteen are displayed in figure 5.18. Compared to sub-event one less recurring frequencies were found to be represented at different locations around the cylinder. By comparing auto-spectral density plots of all sections, symmetric similarity around the cylinder mostly was found towards the sides. Although magnitudes of frequency peaks were small at the edges, frequencies were similar to frequencies found towards the middle of the indenter. Unlike sub-event one, where frequency similarities were observed between sections closer to the middle of the indenter. An exception was section five, where seven recurring frequencies were observed. In general frequencies found in most sections were smaller than 4.5 Hz. Except 7.64 Hz, indicated with a yellow color. 7.65 Hz was found to have a relatively high magnitude in all sections except within sections six, two and one.
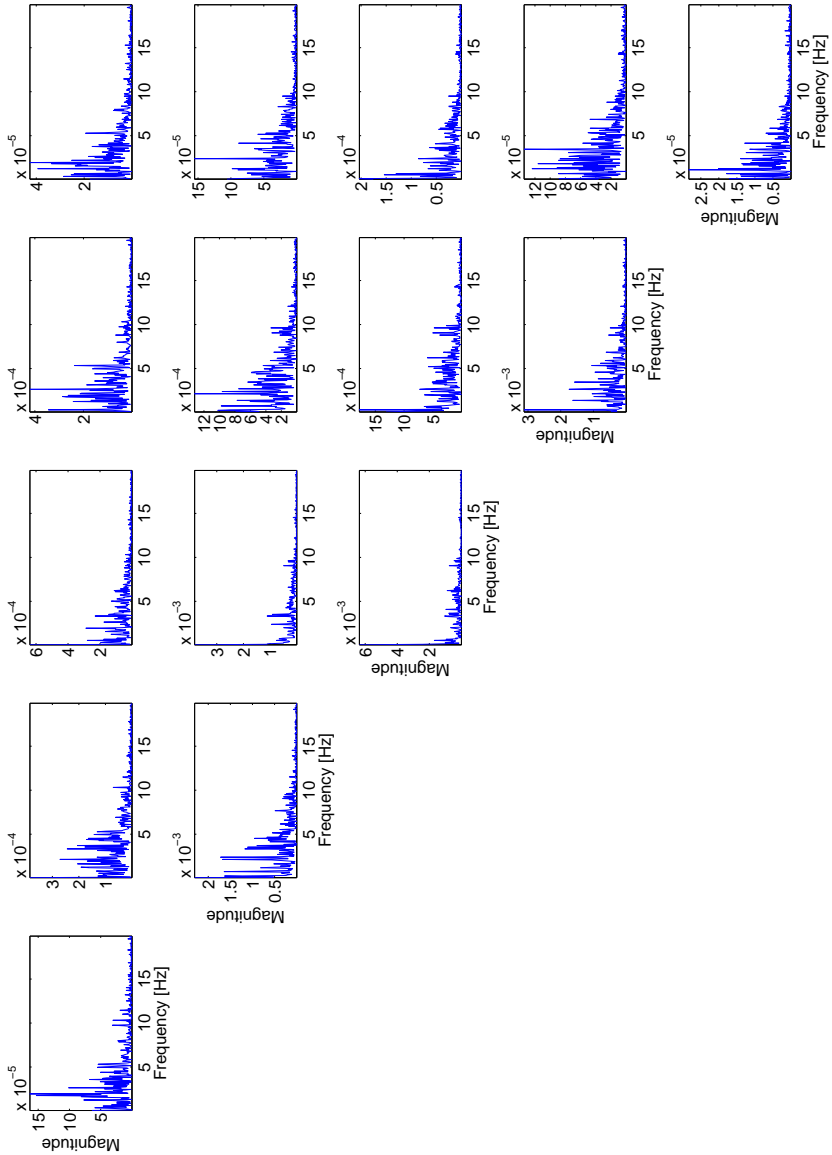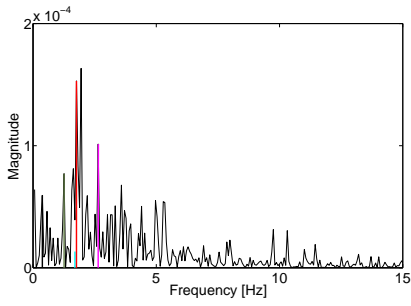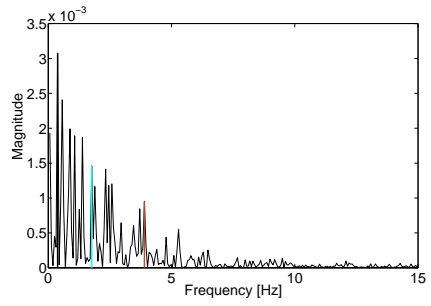
Figure 5.17: Auto- and cross-spectral density plots for sections (from the top) 1,4,7,10,13 within sub-event six

63

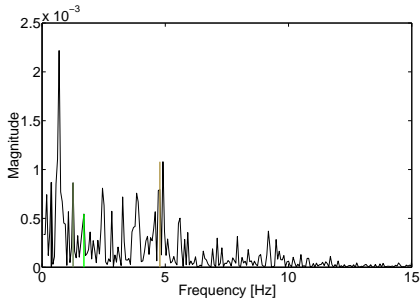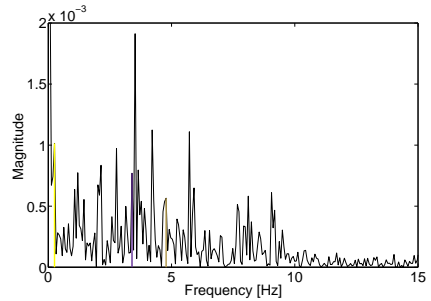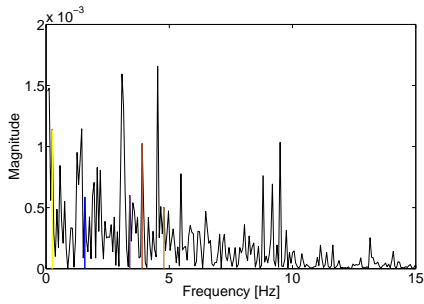(a) Autospectral density section 1
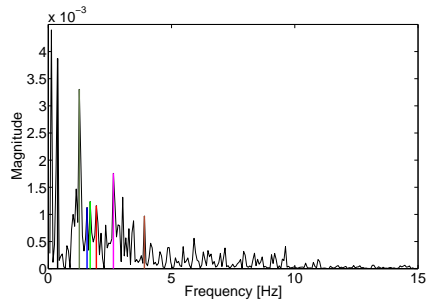
(b) Autospectral density section 2
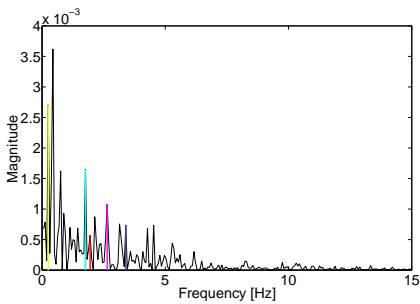
(c) Autospectral density section 3
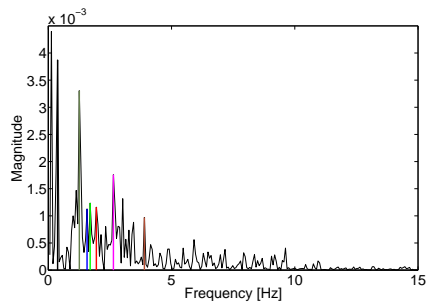
(d) Autospectral density section 5

(e) Autospectral density section 9

(f) Autospectral density section 11

(g) Autospectral density section 12

(h) Autospectral density section 13

Figure 5.18: Auto-spectral density plots for selected sections within sub-event six. Similar frequencies are marked with the same color.

Sub-Event Eight: 100 mm/s

Auto- and cross- spectral density plots for sections one, four, seven, ten and thirteen covering a 15.9 seconds time window are displayed in figure 5.19. Similar to sub-events one and six, sections one and twelve shows lower magnitudes on frequency peaks than rest of the sections. However, sections one and twelve have more equal auto-spectral density plots than lower velocities sub-events. Higher magnitudes were found for higher frequencies compared to lower velocity sub-events. In general magnitude of frequency peaks was lower in sub-event eight than lower velocity intervals. In section seven (middle section), the auto-spectral density plot was almost flat, and only small peaks were observed.

By highlighting similar frequencies in auto-spectral density plots, few similarities were found. Those who are marked in figure 5.20, mostly recurred in two sections. Most of the frequencies that recurred were found in adjacent sections. Figure 5.20 shows some selected sections.

Figure 5.19: Auto- and cross-spectral density plots for sections (from the top) 1,4,7,10,13 within sub-event eight.

(a) Autospectral density section 1

(b) Autospectral density section 2

(c) Autospectral density section 3

(d) Autospectral density section 5

(e) Autospectral density section 9

(f) Autospectral density section 11

(g) Autospectral density section 12

(h) Autospectral density section 13

Figure 5.20: Auto-spectral density plots for selected sections within sub-event eight. Similar frequencies are marked with the same color.

67

5.2 Test Series 3100

Test 3100 was manly analyzed to support findings in test 4300. Due to constant acceleration in test 3100 may there be possible to find a more exact value for the transient speed between intermittent and brittle crushing. Velocity changes in test 3100 are illustrated 5.21. In addition Nord et al. (2014) was reporting about tendencies to frequency lock-in in test 3100. Due to lack of knowledge about the dynamic processes during frequency lock-in, was it of interest to investigate a lock-in event both in frequency and time domain.

Similar to test series 4300, only tactile data was evaluated and shear forces were decomposed and added together as described in section 2.3.1. Test setup and material was the same as in test series 4300. So also here a friction coefficient of 0.027 was used. Both local and global force plots displayed further in this section are including shear forces. In test series 3100 the indenter reached the ice edge with a velocity around 60 mm/s. Unlike test 4300, the whole time series have been analyzed in test 3100. Manly to make sure that time-history plots found in test 4300 was characteristics for medium and high- velocity events. But also to lock fore signs of frequency lock-in in different velocity ranges.
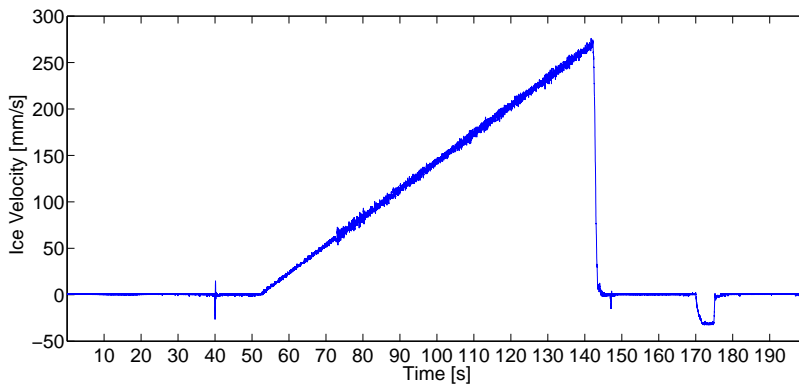
Figure 5.21: Velocity changes with time for test 3100.

Test 3100 runs over approximately two minutes. In contrast to test 4300, test 3100 was divided into four sub-events covering an velocity range (see table 5.2). Range of sub-event I was chosen where a change in crushing regime can be expected based on previously literature and test 4300. Otherwise sub-events were chosen to be approximately in the same lengths. Still, each sub-event was assumed to be stationary.

Table 5.2: Sub-events during test 3100.

Sub event number	Velocity range
I	50 - 100 mm/s
II	100 - 150 mm/s
III	150 - 200 mm/s
IV	200 - 270 mm/s

5.2.1   Time Domain Analysis of Test Series 3100

Similar to test 4300 local forces for each section were evaluated. Figures illustrating correlations plots and local- and global forces between sections within each sub-event were created.

Sub-Event I: 50-100 mm/s

Time-history plot of the global force is displayed in figure 5.22. It has not been observed any clear dominating crushing regime within this sub-event compared to figure 5.3 in test series 4300. However, it seemed to be a change in force pattern after 2.5 seconds. Faster fluctuations and smaller difference between low and high force peaks may be observed. If this indicated a change in crushing regime or a convenient is not clear. Test series 3100 started at relatively high velocities, so the opportunities to compare with lower velocity ranges was limited.

Local forces were evaluated on different locations around the indenter. Figure 5.23 display time-history plots for some local forces. In general section one was exposed to higher forces than section thirteen. Figure 5.23f illustrates the same trend as found for section one and three in test series 4300. It seems like ice was sliding against the cylinder. Both section two and twelve showed rapid fluctuations between lower force areas. In figure 5.23e few correlations were observed, rather the opposite. No particular brittle or intermittent crushing trends were found. Unlike sections two and twelve figure 5.23d show a sawtooth pattern time-history plot. Sections three and eleven tended to have better correlation than sections two and twelve. However this correlation declined towards the end of the time window. Similar to sections three and eleven an intermittent crushing regime dominated in sections four and ten. Figure 5.23b display the time-history plot for sections five and nine within sub-event I. In these two sections distinct sawtooth patterns were observed throughout the entire sub-event compared to sections further out on the cylinder. Local forces in sections six, seven and eight shows fluctuating time-history plots compare to other section in this sub-event. Local forces from sections four and ten and out towards the edges shows small tendencies to intermittent crushing, compared to what may be seen from figure 5.22. Especially from figure 5.23c may there be observed a sawtooth patterned force plot with small force drops in the loading phase.
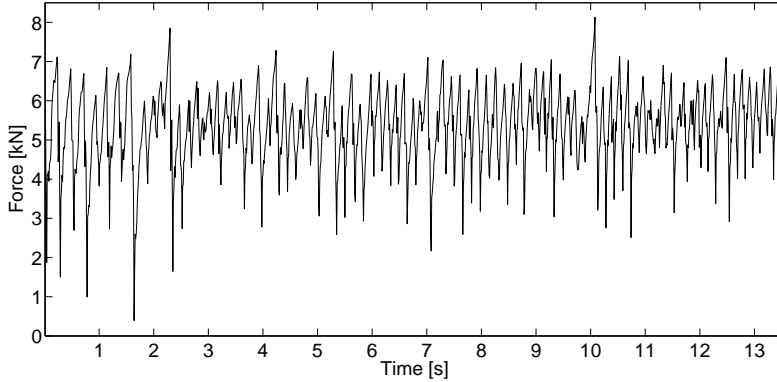
Figure 5.22: Global force time-history plot for sub-event I.

Figure 5.24 displays time-history plots of local forces within sub-event I where sections four, six, seven, eight and ten are compared. No changes in force trends between these five sections were observed through the time interval. Only a short time window was displayed here as an illustration. Compared to the global force in figure 5.22, local forces do not show any change in trend after 2.5 seconds.

A bar representation of the correlation matrix for sub event I may be seen in figure 5.25a. High correlation values were found between most of the sections expect, sections one and thirteen where correlation with other panels were low. These trends can also be seen in figure 5.25b. Red area indicates high correlation and mainly were found around the middle of the indenter and on the diagonal of the correlation matrix where self-correlation are displayed. In both representations low correlations were found between sections two, twelve and the other sections. These pattern was also found from time-history plots in figure 5.23. Sections two and twelve have an appreciable different trend than the other sections.
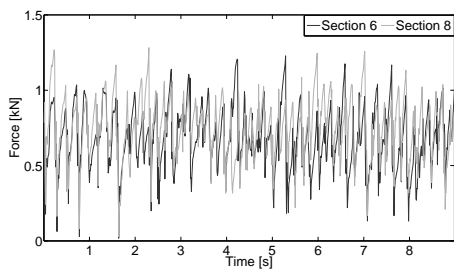
(a) Section six and eight.
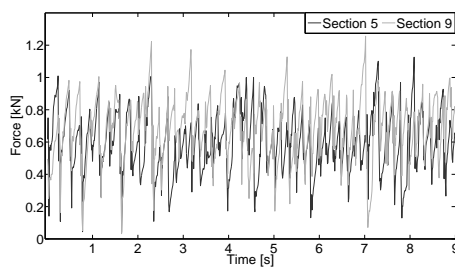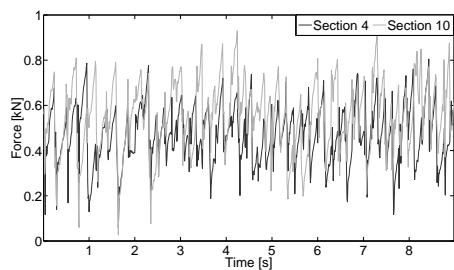
(b) Section five and nine.

(c) Section four and ten.
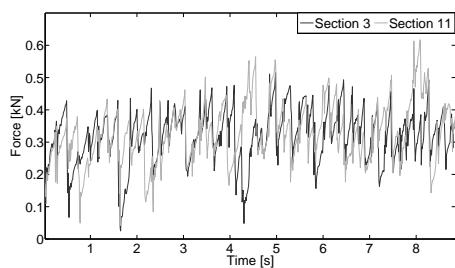
(d) Section three and eleven.
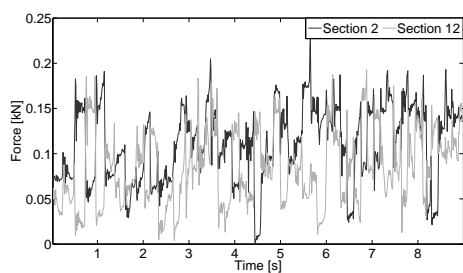
(e) Section two and twelve.
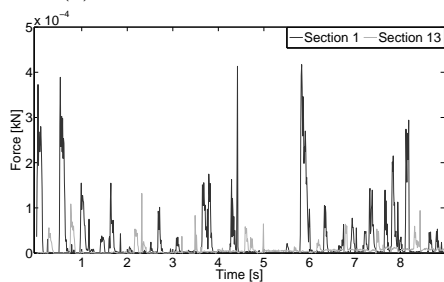
(f) Section one and thirteen.

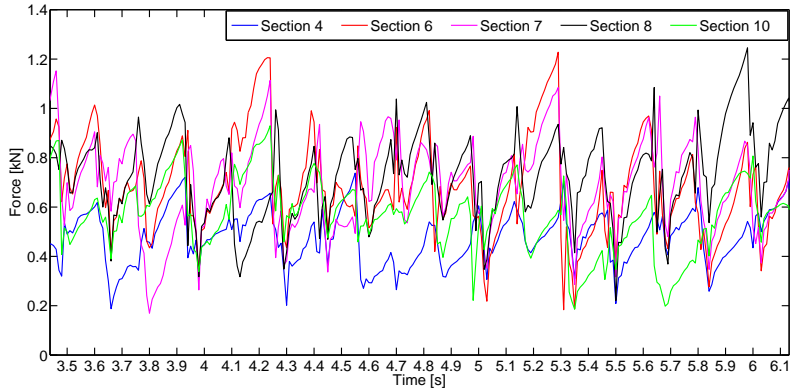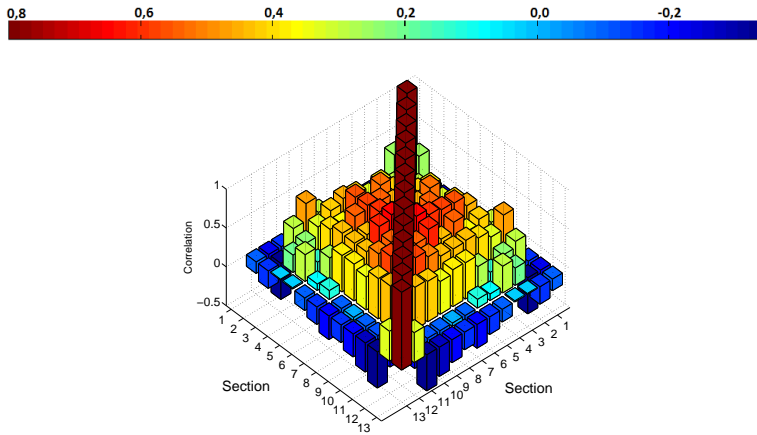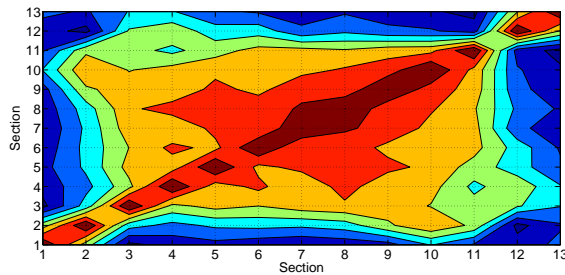Figure 5.23: Local forces in symmetrical sections around the middle of the indenter.

Figure 5.24: Local force plots for sections 4,6,7,8 and 10 within sub-event I.

(a) Correlation coefficient matrix 3-D bar chart for sub-event I.

(b) Correlation coefficient matrix contour plot for sub-event I.

Figure 5.25: Section correlations during a time window covering the 50- 100 mm/s velocity interval.

A tendency to frequency lock-in or self-excitation within test 3100 was found from accelerometer and strain gauges data analyzed by Torodd S. Nord. In this data a 1.4 seconds frequency lock-in event could have taken place. Tendencies to lock-in may be found approximately 70 seconds into test 3100.

Figure 5.26a shows a 12 seconds time history plot within sub-event I. The red square indicates where a frequency lock-in event may have taken place. From the highlighted image in figure 5.26b it may be observed a regular residual pattern of alternating phases with ductile loadings and brittle unloading. A small notch can be seen in the unloading phase. The ellipses indicate areas with deviations from this pattern during the possible event. Deviations like that may be explained by change in ice characteristics during the event.
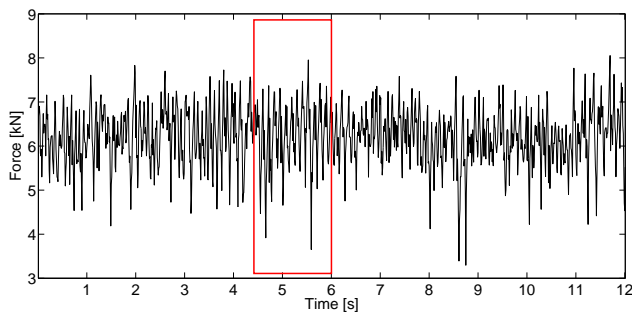
(a) Time-history plot of the global force around a potential lock-in event.
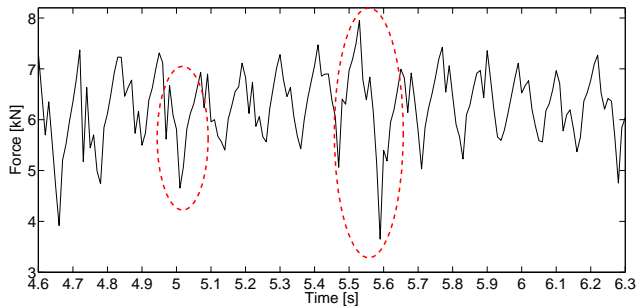
(b) Time-history plot during tendencies to frequency lock-in.

Figure 5.26: Time-history plots for a smaller time window within sub-event I.

Figure 5.27 shows time-history plots of local forces during the potential lock-in event. Due to large deviations from other panels sections one and two were not included. A corresponding deviation as found in figure 5.26b is not recognized in time-history plots for local forces in sections eleven to three. Towards the edges of the cylinder lower forces were recorded and no special force pattern observed from time-history plots. High accordance between panels may be seen from figure 5.27.
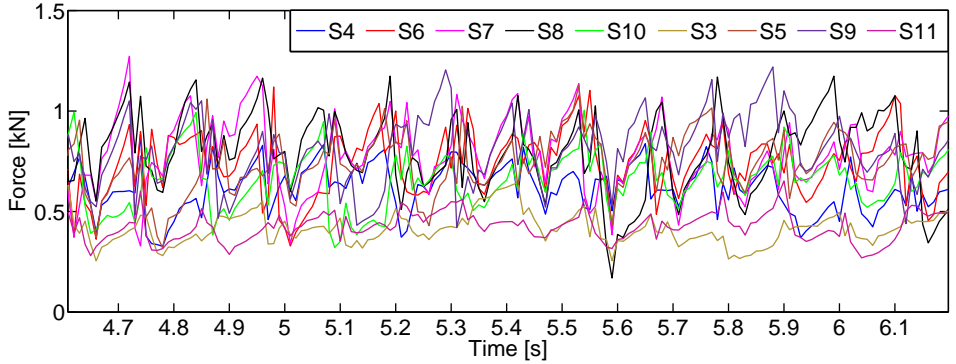

Figure 5.27: Local forces at different locations around the indenter during tendencies to frequency lock-in. S stands for section.

Figure 5.28 illustrates correlation between panels before, after and during the potential event. To get an equal basis for comparison, each sub-event covered a 1.4 seconds time window. Higher correlations between panels were found during tendencies to frequency lock-in, compared to directly after the event. Panel correlation 1.4 seconds before the event show a correlation value between 0.2 and 0.0 for most panels. This may be seen from a lot of green and blue colored areas in figure 5.28b. A reduction of this green colored area may be seen in figure 5.28d. However in figure 5.28c and 5.28d higher correlation between directly adjacent sections were observed. The general correlation seemed to be lower, but some areas marked green before are during the event colored orange, indicating higher correlation than before. After the event, a small and random correlation was observed from figure 5.28. The contour plot during the possible event implies the same as found from time-history plots. Local forces from sections three to eleven were better correlated.
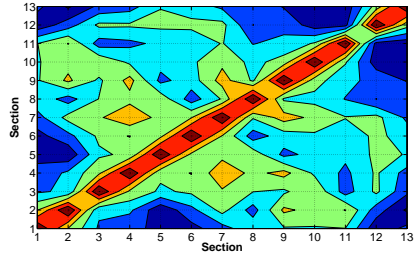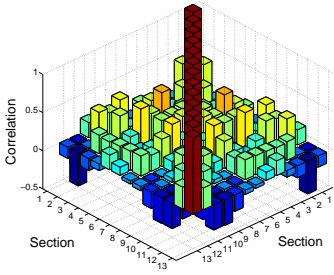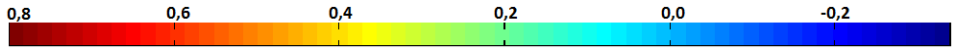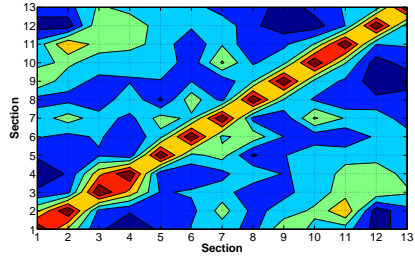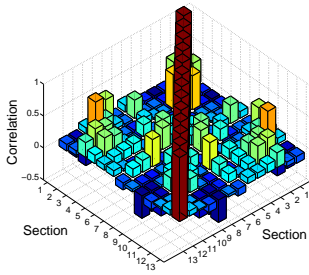
(a) Bar representation of the correlation between sections before the event.

(b) Contour plot of local forces before the locked-in event.
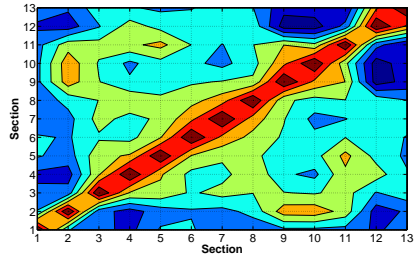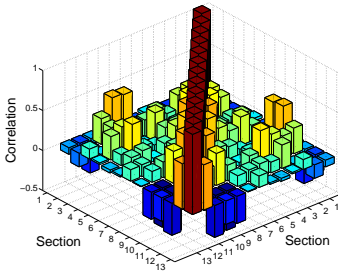
(c) Bar representation of the correlation between sections during the event.

(d) Contour plot of local forces during tendencies to frequency lock-in.

(e) Bar representation of the correlation between sections directly after the event.

(f) Contour plot of local forces directly after the frequency locked-in event.

Figure 5.28: Correlation plots in shorter time windows within sub-event I.

Sub-Event II: 100-150 mm/s

Sub-event II covered velocities between 100 mm/s and 150 mm/s. Compared to the global force found within sub-event I, figure 5.29 shows a more dynamic process. A continuous brittle crushing regime seemed to dominate the process. Evaluation of local forces in the same thirteen sections as sub-event I, shows similar trends in time-history plots for all sections except for the outer two on each side of the cylinder. Similar to lower velocity ranges sections one and thirteen within sub-event II were exposed to lower forces compared to other areas around the cylinder. Section one had some force peaks that was higher than forces peaks in section thirteen. However in both cases it seemed as ice and rubble slide along the indenter. Time-history plots for sections two and twelve are seen in figure 5.30e. Force trends similar to them found previously in test 3100 was found in figure 5.30. Changes to this trend were not found throughout the time window. Local forces evaluated closer to the middle of the indenter show a random crushing pattern, indicating a brittle crushing regime. From local force time-history plots sections five, nine and eight were found to be well correlated compared to other sections within the same sub-event.
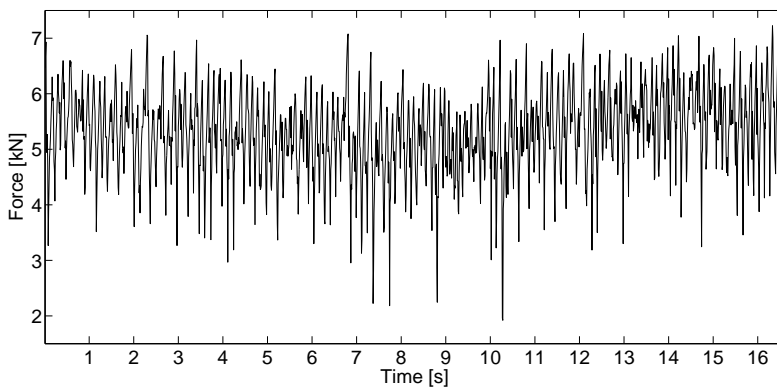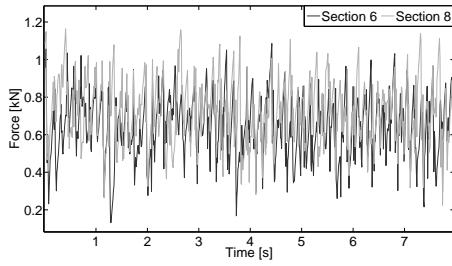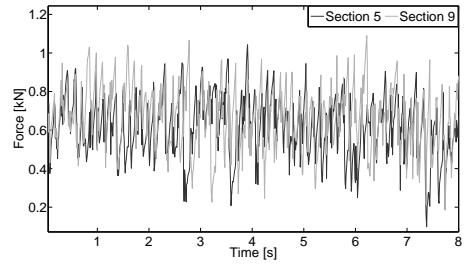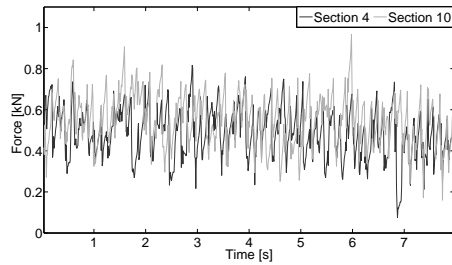

Figure 5.29: Global force time-history plot for sub-event II.
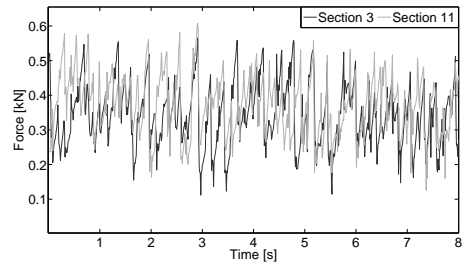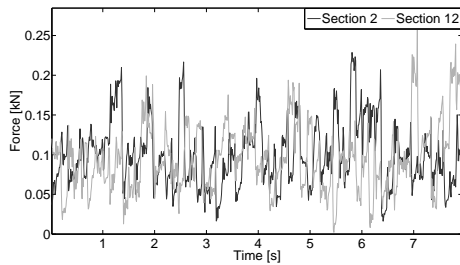
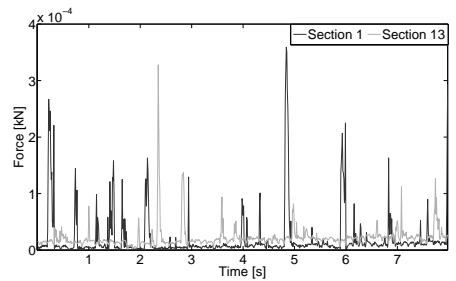(a) Section six and eight.

(b) Section five and nine.

(c) Section four and ten.

(d) Section three and eleven.

(e) Section two and twelve.

(f) Section one and thirteen.

Figure 5.30: Local forces in symmetrical sections around the middle of the indenter.

Trends for all thirteen local forces were compared. A small time window for sections four, six, seven, eight and ten are displayed in figure 5.31. Unlike figure 5.24, figure 5.31 shows a random crushing pattern and forces within each section was not easily compared. In contrast to lower velocities plots where the process was less dynamic.

Figure 5.32a illustrates the correlation coefficient matrix for sub-event II by using bar representation. Relative high correlation between adjacent sections were observed, but unlike sub-event I correlations with other sections was low. Three exceptions were sections three, five and twelve. They seemed to be better correlated with other sections. This were not found by a closer lock at time-history plots. However, high correlation were observed between sections five and eight. High correlation was also observed from time-history plots in figure 5.30.
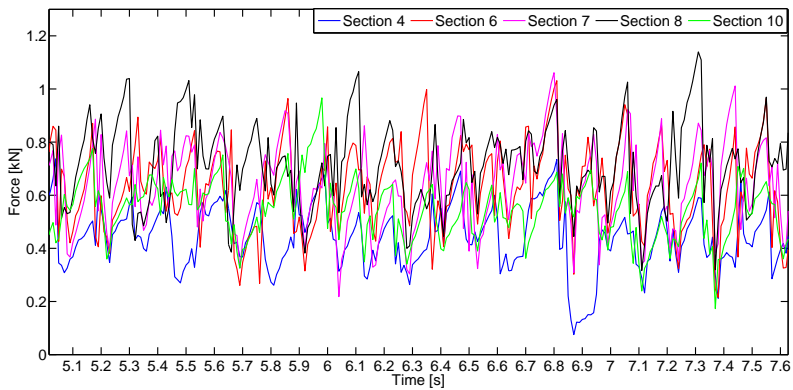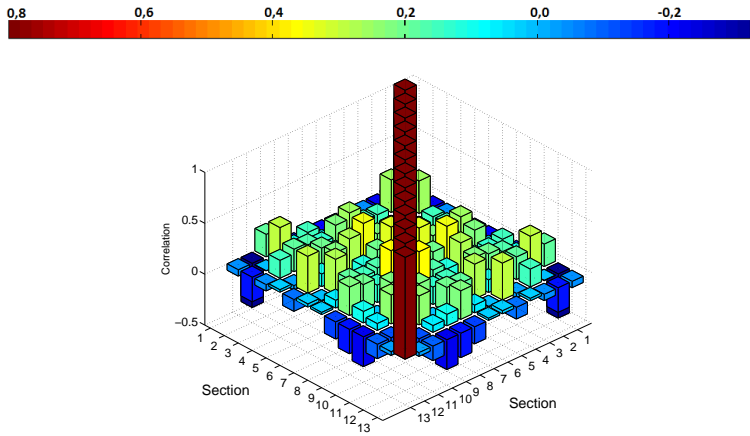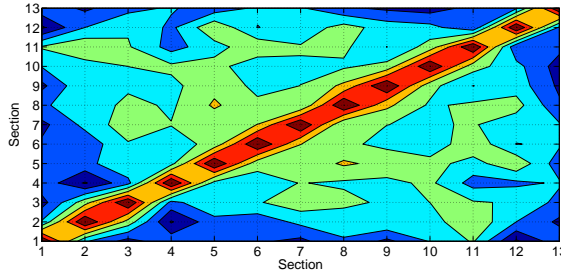

Figure 5.31: Local force plots for sections 4,6,7,8 and 10 for a smaller window of observation within sub-event II.

(a) Correlation coefficient matrix 3-D bar chart for sub-event II.

(b) Correlation coefficient matrix contour plot for sub-event II.

Figure 5.32: Panel correlations during a time window covering the 100- 150 mm/s velocity interval.

Sub-Event III: 150-200 mm/s

Figure 5.33 shows the global force for a time window covering sub-event III, ranging from 150 mm/s to 200 mm/s. The time-history plot for the global force tended to be random, indicating a dominating brittle crushing regime.

From figure 5.34 and further investigations of local forces were sections six, seven and eight observed to have similar trends compared to other sections. However this was not the case when decreasing and increasing number of local forces. Local forces in twelve sections are displayed in figure 5.35. Sections one and thirteen were exposed to relatively low forces. Force peaks occurred with variating frequencies. Figure 5.35e indicates a random crushing procedure in sections two and twelve. Time- history plots for sections five to nine shows an increase in fluctuation and an average decrease in amplitude. At the same time sections five and nine seemed to be well correlated certain places within sub-event III. Time-history plots were

characterized by small force variations that occurred between larger and faster force buildups and force drops phases. Local forces from remaining sections show clearly a dominating continuous brittle crushing regime.
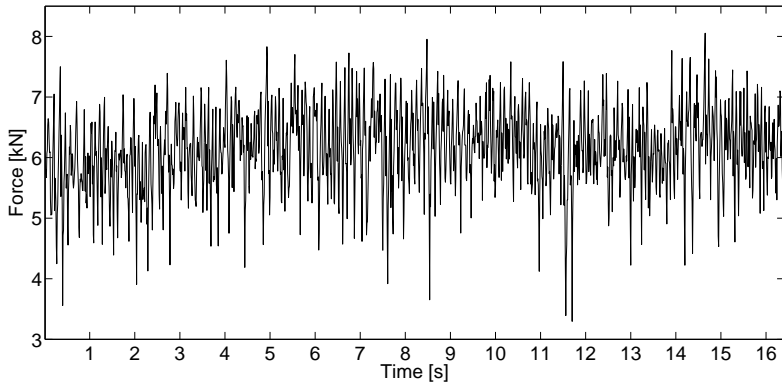

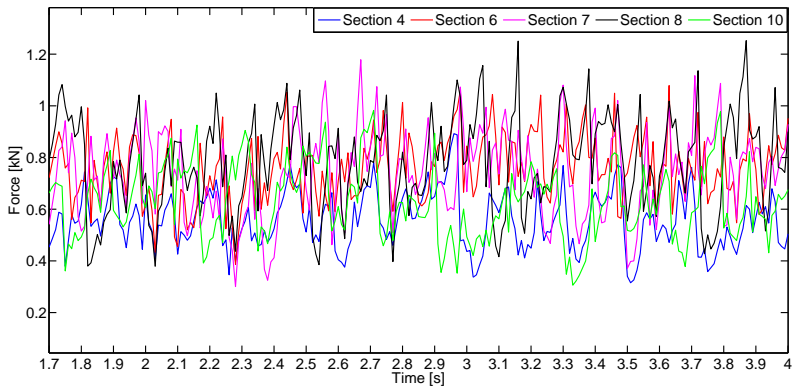Figure 5.33: Global force time-history plot for sub-event III.
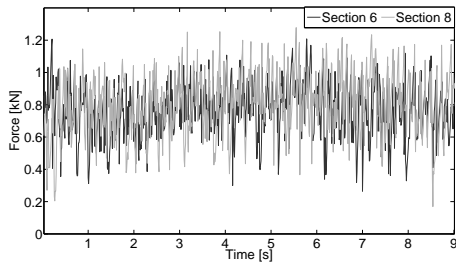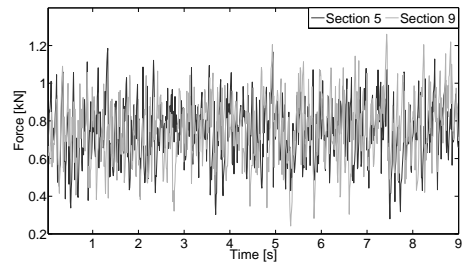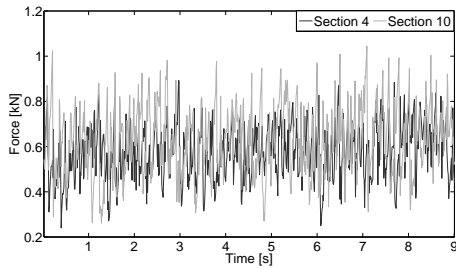

Figure 5.34: Local force plots for sections 4,6,7,8 and 10 for a smaller window of observation within sub-event III.
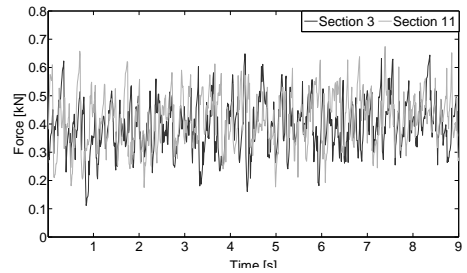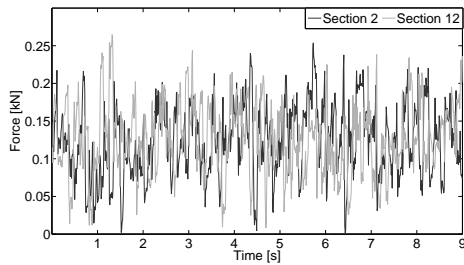
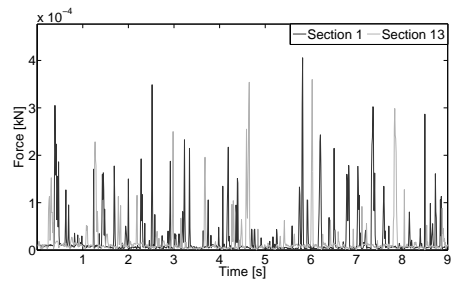(a) Section six and eight.

(b) Section five and nine.

(c) Section four and ten.

(d) Section three and eleven.

(e) Section two and twelve.

(f) Section one and thirteen.

Figure 5.35: Local forces in symmetrical sections around the middle of the indenter.

The bar representation in figure 5.36a shows highest correlation between sections twelve and thirteen. Similar to observations seen in other sub-events, higher correlation tended to occur between directly adjacent panels than distant panels. From figure 5.36a may there observed a higher correlation between sections two, three, four and ten, eleven, twelve. These are symmetrical sections around the middle of the indenter. Areas marked with green in figure 5.36b, indicates the same observation as found from the bar representation. However this was not seen from time-history plots.
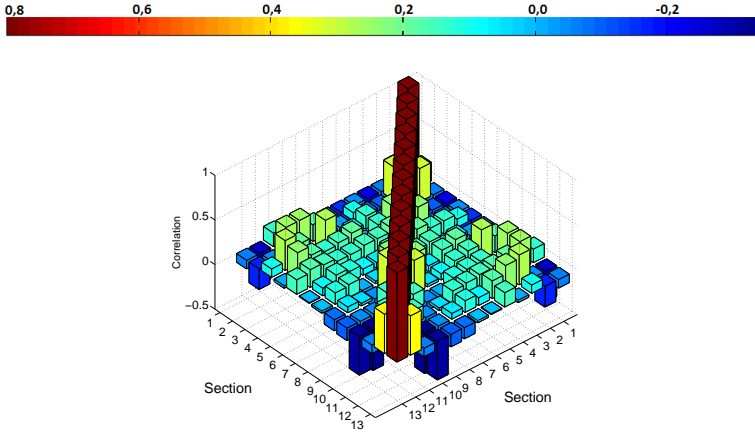
(a) Correlation coefficient matrix 3-D bar chart for sub-event III.
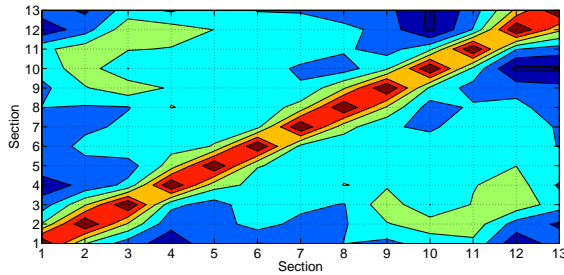
(b) Correlation coefficient matrix contour plot for sub-event III.

Figure 5.36: Panel correlations during a time window covering the 150- 200 mm/s velocity interval.

Sub-Event IV: 200-270 mm/s

Both local and global forces was dominated by a continuous brittle crushing regime in sub-event IV, covering the velocity range from 200 mm/s to 270 mm/s. As expected for this velocity ranges figure 5.37 displaying the global force, was showing continuous brittle crushing.

Figure 5.38 compare local force trends in sections four, six, seven, eight and ten. Local forces were in general highly uncorrelated, but some sections show higher correlation than other. However where and witch sectors that was correlated appeared to be more or less random over time. From figure 5.39 may there be seen that sections one and thirteen indicates the same trend as observed for previous sub-events in test series 3100, but also in test 4300. It seemed as processes near the edges were more dynamic with increased velocities, also by evaluating sections two and twelve. Figure 5.39e shows a dominating brittle crushing regime, compared to what have been observed for this sections in previous time windows. Similar to sub-events II and III tended sub-event IV to be more dynamic closer to the middle of the cylinder. A random crushing process dominated and no particular force pattern was found.
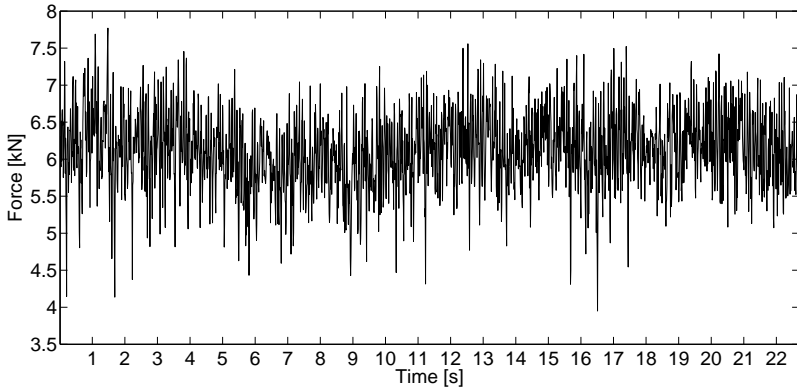
Figure 5.37: Global force time-history plot for sub-event IV.
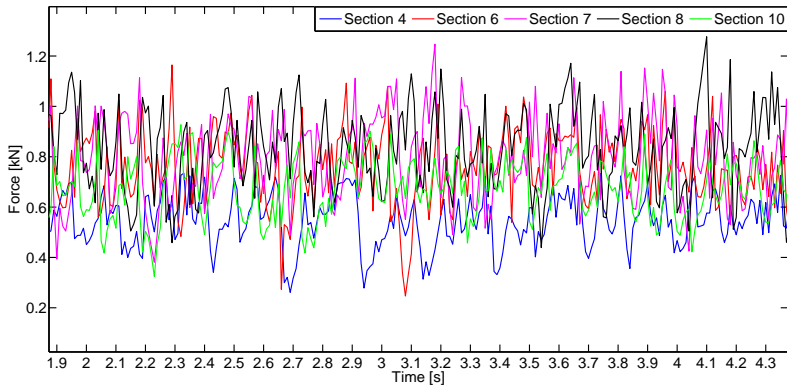
Figure 5.38: Local force plots for sections 4,6,7,8 and 10 for a smaller time window of observation within sub-event IV.
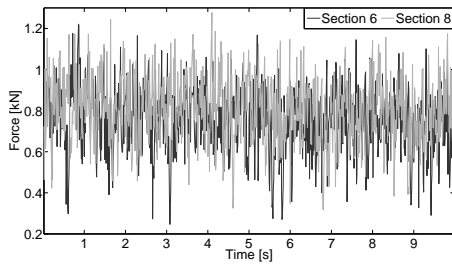
(a) Section six and eight.
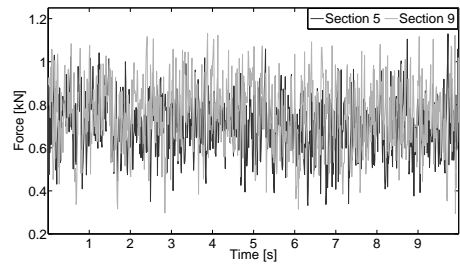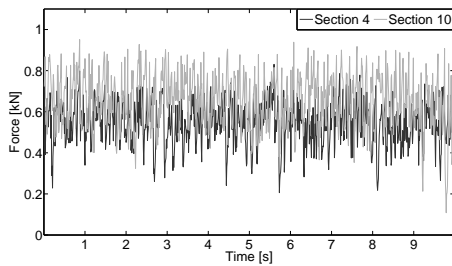
(b) Section five and nine.

(c) Section four and ten.
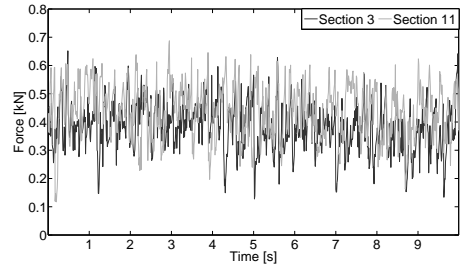
(d) Section three and eleven.
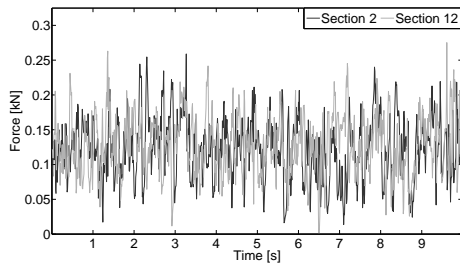
(e) Section two and twelve.
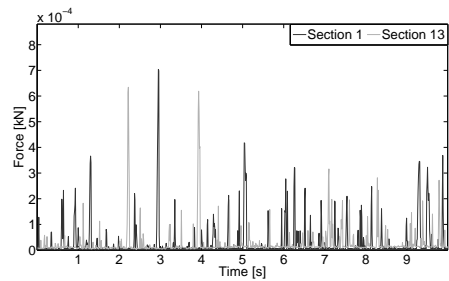
(f) Section one and thirteen.

Figure 5.39: Local forces in symmetrical sections around the middle of the indenter.

Both figure 5.40a and 5.40b shows high self correlation, however correlation between direct nearby sections were lower than similar illustrations have indicated for sub-events covering lower velocities. Areas colored green in figure 5.40b indicate slightly higher correlation between sections twelve and five, twelve and six, eleven and two, eleven and four. This was not observed from time-history plots.
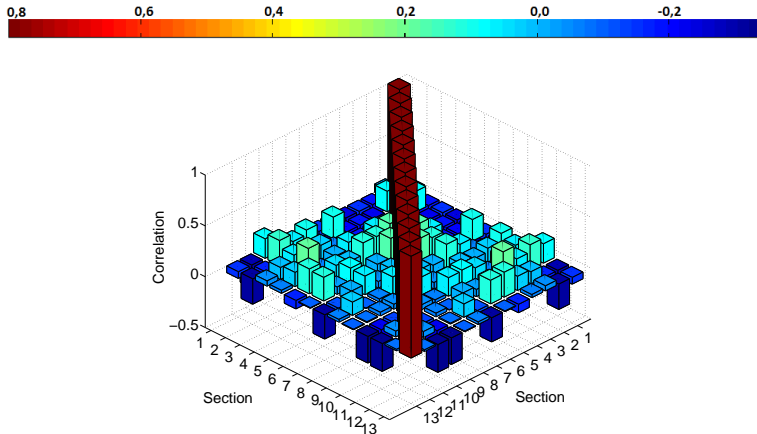
(a) Correlation coefficient matrix 3-D bar chart for sub-event IV.
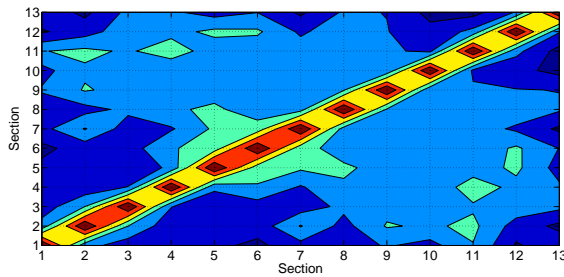
(b) Correlation coefficient matrix contour plot for sub-event IV.

Figure 5.40: Panel correlations during a time window covering the 200- 270 mm/s velocity interval.

5.2.2 Stochastic Dynamic Analysis of Structures; Test 3100

Similar to test 4300, spectral analysis was used to evaluate if changes in crushing regimes easily can be found from frequency domain. Both auto- and cross spectral densities are displayed below for each sub-event.

Sub-Event I: 50-100 mm/s

Figure 5.41 displays auto-and cross spectral density plots for sections one, four, seven, ten and thirteen. Relatively high peak values were found at high frequencies. Auto- spectral densities on the diagonal of the matrix are highly fluctuating, except within section twelve. Hardly any peaks were seen in section twelve. Similar to test 4300 both auto- and cross-spectral density plots were approaching zero at higher frequencies (>10 Hz). Equivalent to test 4300 cross-spectral densities seen in column five was little affected by sections one and thirteen, due to low magnitude of frequency peaks. Some auto-spectral density plots are displayed in figure 5.42. Frequencies that occurred in more than two sections are marked with similar colors. In general, few signs of patterns were found by locking where each frequency was present. Frequencies found in most sections seemed to be more ore less random orientated. Although there may be found cases of symmetry around the middle of the indenter. For example 6.5 Hz was found both in sections four and ten. Frequencies of 2.36 and 6.06 Hz were observed both in sections six and eight.

Figure 5.41: Auto- and cross-spectral density plots for sections (from the top) 1,4,7,10 and 13.
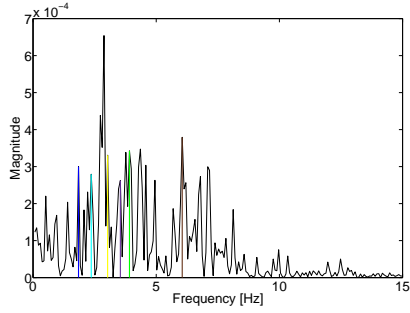
(a) Autospectral density section 6
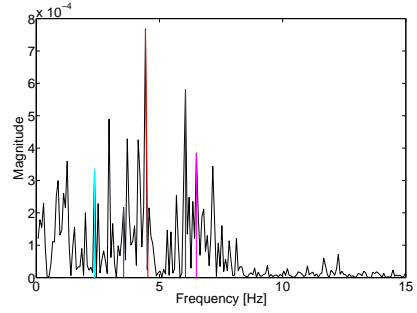
(b) Autospectral density section 8
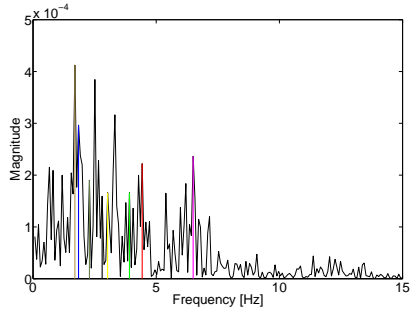
(c) Autospectral density section 4

(d) Autospectral density section 10

(e) Autospectral density section 2

(f) Autospectral density section 12

Figure 5.42: Auto-spectral density plots for some sections within sub-event I. Similar frequencies are highlighted with the same color.

In order to find out more about dynamic characteristic of ice forces during a frequency lock-in event, auto- and cross-spectral density plots within the possible time window was further investigated. Duan et al. (2002) found multiple resonance frequencies observed from the spectrum during a self-excited event. Similar findings were seen from auto- and cross-spectral density plots in figure 5.43 and 5.44. Figure 5.44 show small difference between functions within the central sections (three to eleven). The red line indicating 8.57 Hz was dominating in nine of thirteen sections. Also in sections one, two and twelve there was found peaks at 8.57 Hz. However, not as clear as in section three to eleven. This resonance frequency was below 9.45 Hz and 14.9 Hz which was reported to be the first and second mode of the system (Nord and Määttänen, 2013). As may be seen from figure 5.44 was neither 9.45 Hz or 14.9 Hz any resonant frequency. Another finding was seen in sections four and ten, a peak was observed at 4.286 Hz. Exactly half of the dominating resonance frequency. It is hard to say whether this may be a phenomenon or just a coincidence. This possible sub-harmonic frequency was only found within two panels.

Tendencies to a 1.4 seconds lock-in event was not detected in frequency domain when analyzing sub-event I covering a 13.5 seconds time window. The resonant frequency during the possible event was only noted in one section when analyzing the whole time window. Length of the sub-event had to be decreased to notice. The same time window used during time domain analyzes around the event, were used to se if the lock-in event may be detected. Even not then could resonance frequencies around the cylinder be found. Other frequencies were dominating and 8.57 Hz was only found in five sections. The time window had to cover only the time length where tendencies to lock-in was found.
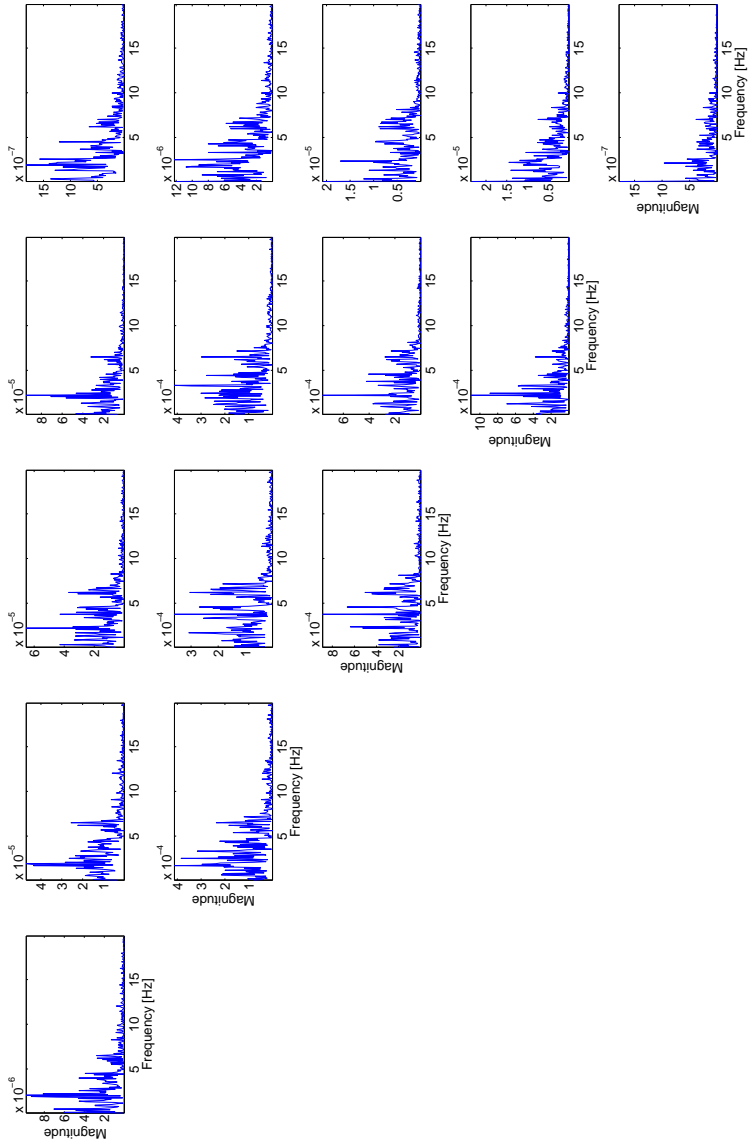
Figure 5.43: Auto- and cross-spectral density plots for sections (from the top) 1,4,7,10 and 13.
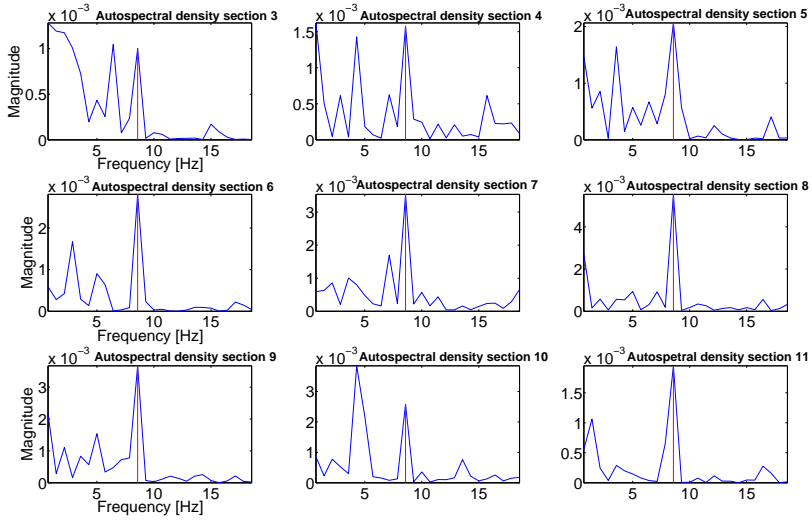
Figure 5.44: Auto-spectral density plots for sections three to eleven during tendencies to frequency lock-in.

Sub-Event II: 100-150 mm/s

Figure 5.45 show fluctuating spectral density plots compared to sub-event I, representing velocity step 50-100 mm/s. Greater response at higher frequencies seemed to be repetitive in most sections. Spectral density plots tended to approach zero at velocities higher than 20 Hz.

From figure 5.46 was few similar frequencies found. Most of them at lower frequencies (<2 Hz). 8.45 Hz occurred in all sections from four to ten except within section eight. A pink line in figure 5.46a, 5.46c and 5.46d indicates 8.45 Hz.

Figure 5.45: Auto- and cross-spectral density plots for sections (from the top) 1,4,7,10 and 13.
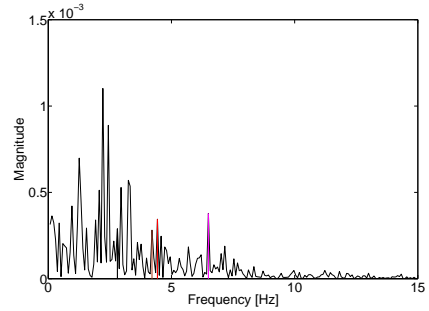
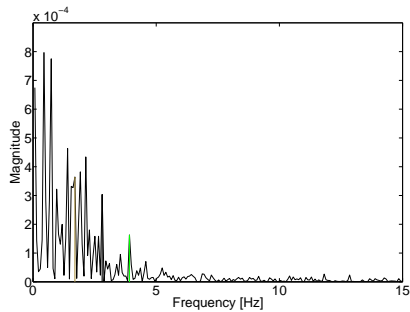(a) Autospectral density section 6   (b) Autospectral density section 8
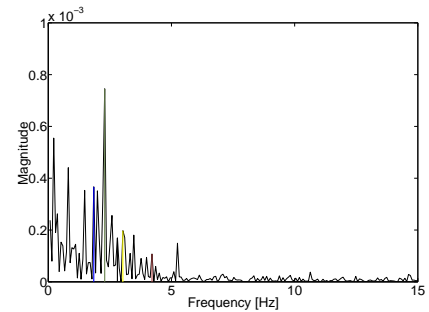
(c) Autospectral density section 4   (d) Autospectral density section 10

(e) Autospectral density section 2   (f) Autospectral density section 12

Figure 5.46: Auto-spectral density plots for some sections within sub-event II. Similar frequencies are highlighted with the same color.

Sub-Event III: 150-200 mm/s

Figure 5.47 stands out from figure 5.45 within sub-event II. The spectral density plots occurred to fluctuate less and attempt to approach zero at lower frequencies. By highlighting recurring frequencies was a pattern found around the cylinder. Some frequencies were recurring symmetrically around the middle of the indenter. Examples of this may be seen in all sections displayed in figure 5.48. A trend like this was not been observed in other sub-events in time series 3100 and similar trends were not found when increasing or decreasing the time window. When dividing the indenter into smaller sections like 52 instead of 13, there was not found any frequency pattern.
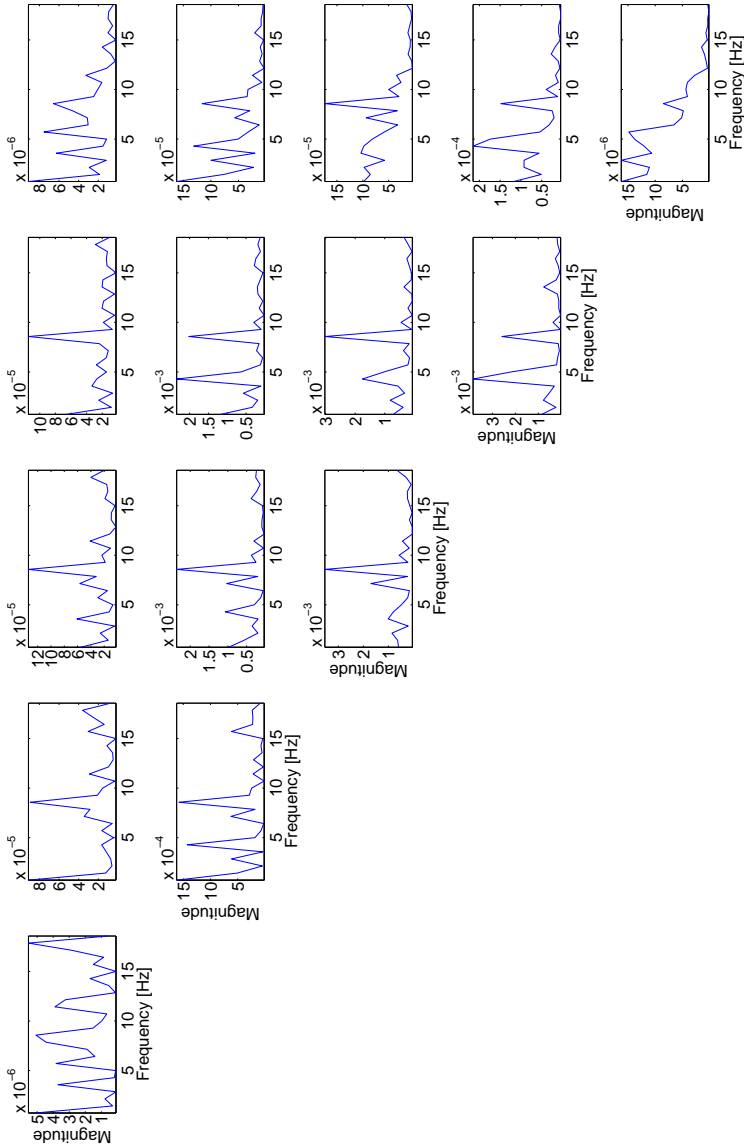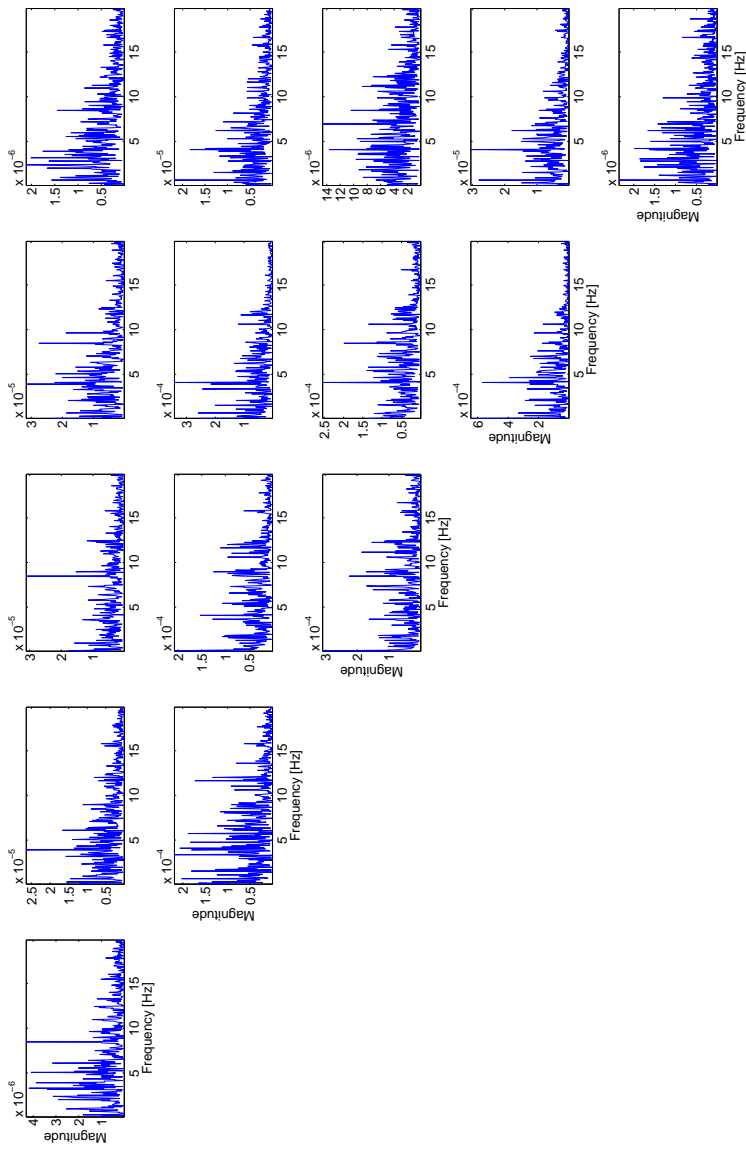
Figure 5.47: Auto- and cross-spectral density plots for sections (from the top) 1,4,7,10 and 13.
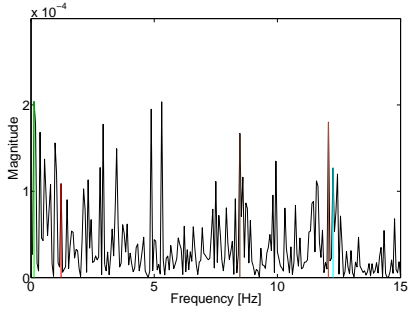
(a) Autospectral density section 6   (b) Autospectral density section 8
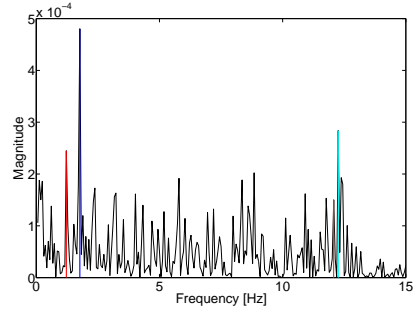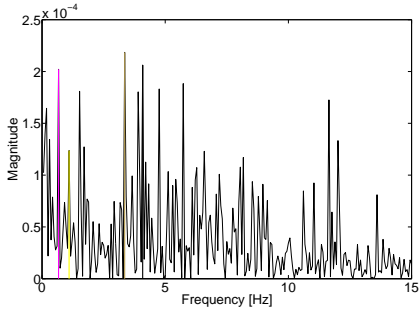
(c) Autospectral density section 4   (d) Autospectral density section 10
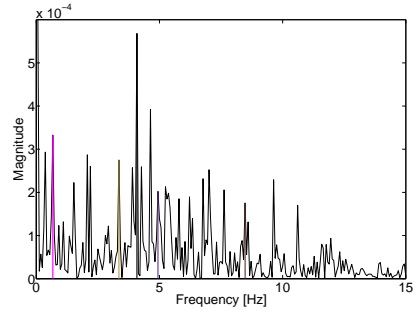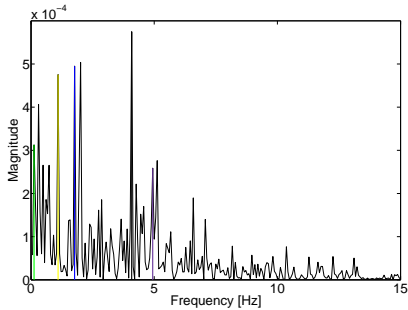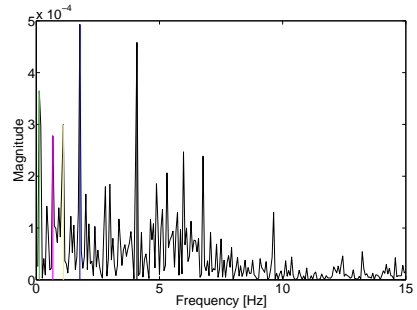
(e) Autospectral density section 2   (f) Autospectral density section 12

Figure 5.48: Auto-spectral density plots for some sections within sub-event III. Similar frequencies are highlighted with the same color.

Sub-Event IV: 200-270 mm/s

Same trends observed in sub-event IV were found form the auto- and cross-spectral density matrix in figure 5.49. A closer lock at the auto-spectral density plots shows few recurring frequencies at different locations around the indenter. Auto-spectral density plots for sections six, eight, four, ten, two and twelve are seen in figure 5.50, a color is representing the same frequency. Similar to sub-event I, most of the frequencies that recurred was found in sections close to the middle of the indenter. When changing number of sections, the recurring frequency pattern changed, so the location of dominating frequencies seemed to be random. Unlike sub-event II,recurring frequencies was in this case relatively high (<10 Hz). 13.26 Hz may be found to recur in six sections, three of them displayed in figure 5.50.
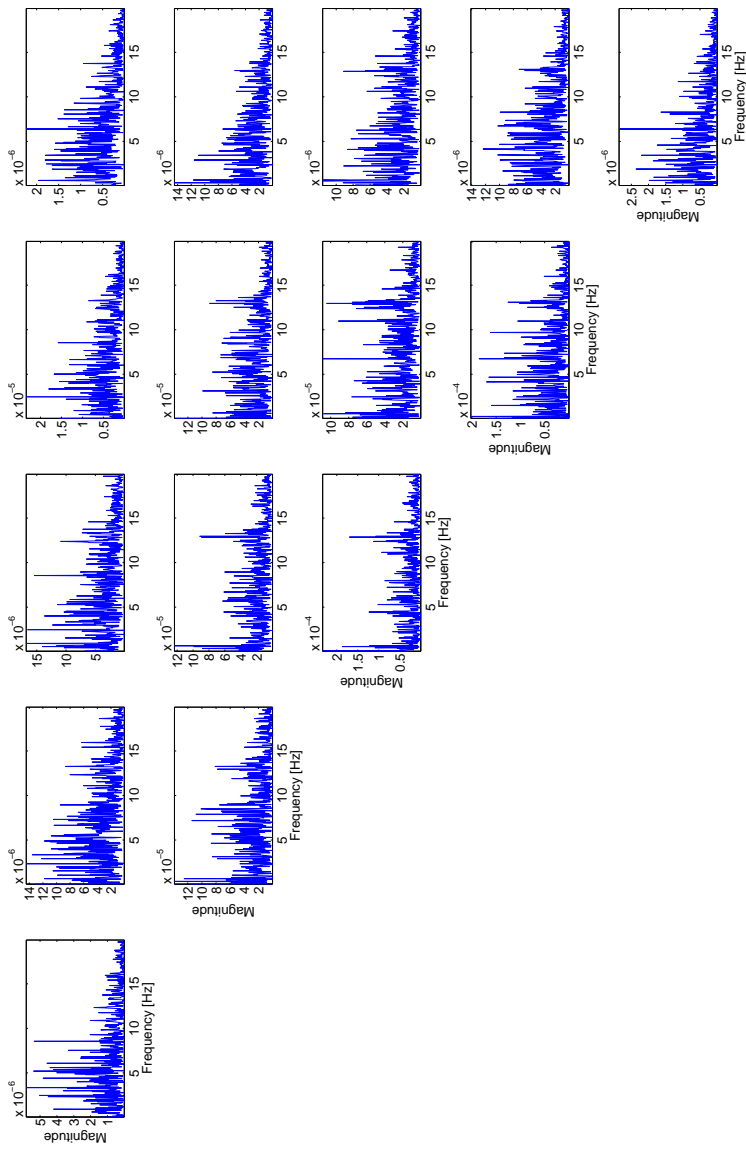
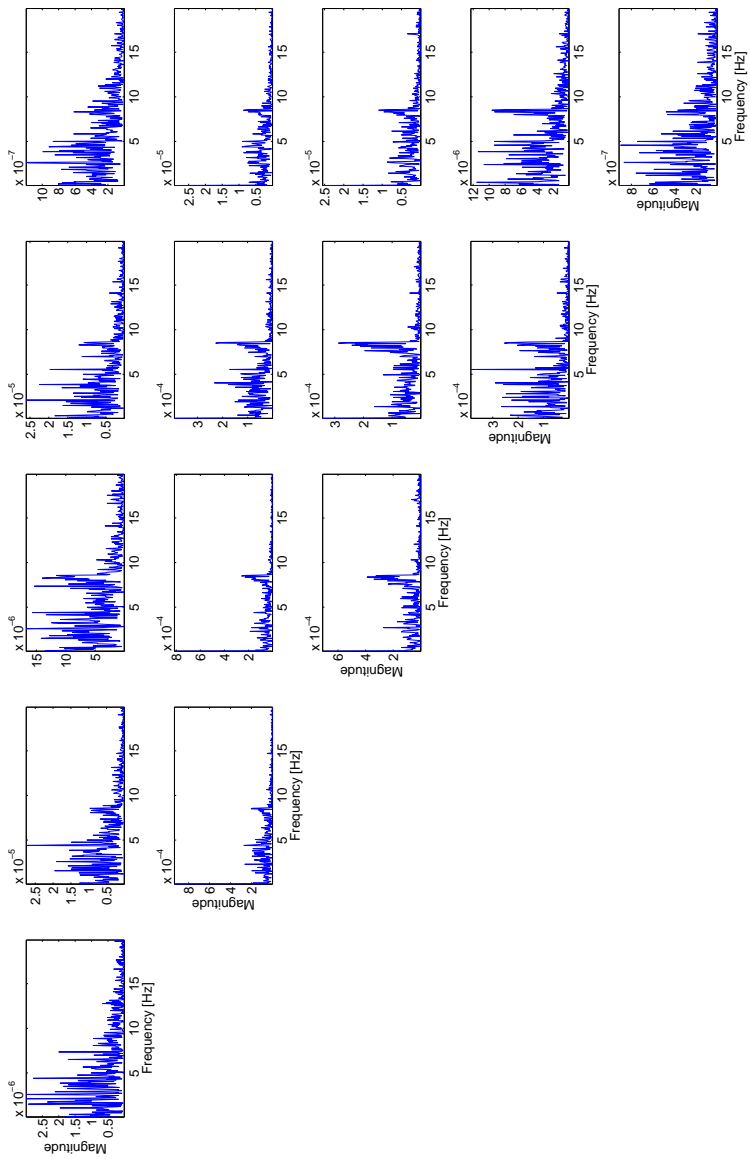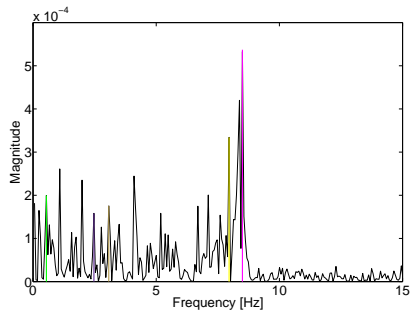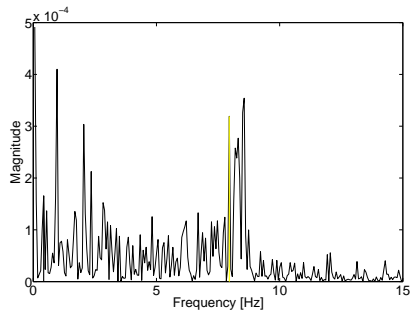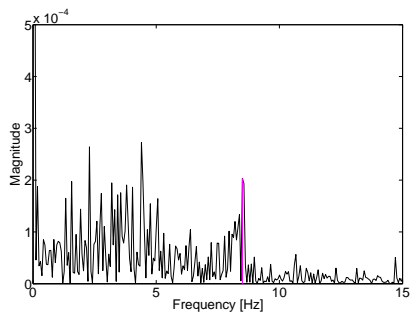Figure 5.49: Auto- and cross-spectral density plots for sections (from the top) 1,4,7,10 and 13.
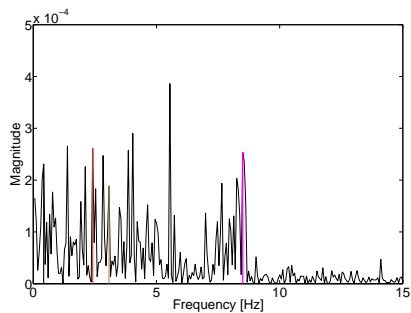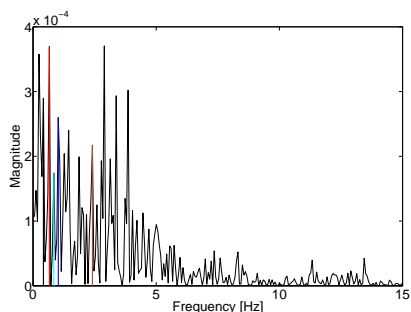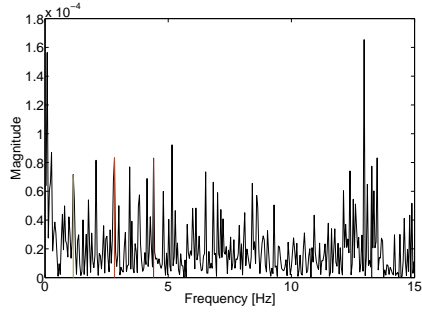
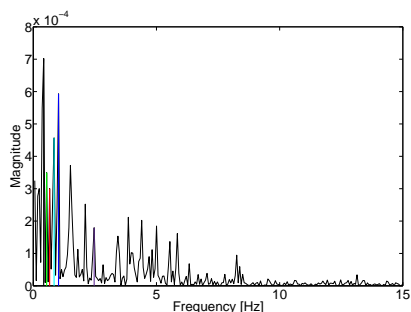(a) Autospectral density section 6
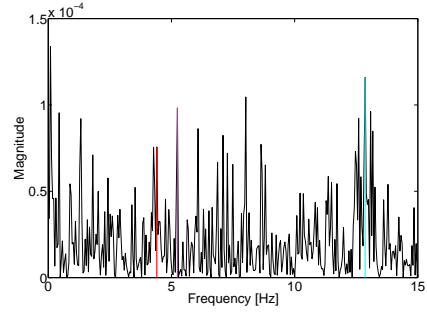
(b) Autospectral density section 8
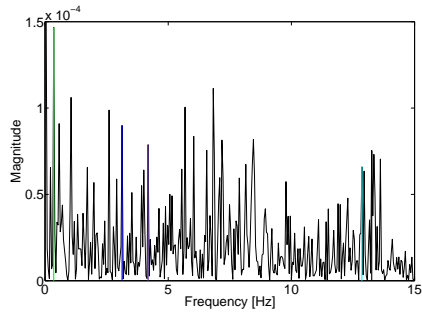
(c) Autospectral density section 4
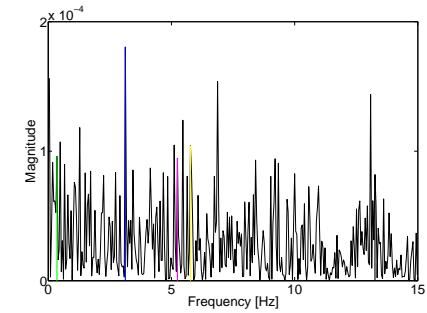
(d) Autospectral density section 10
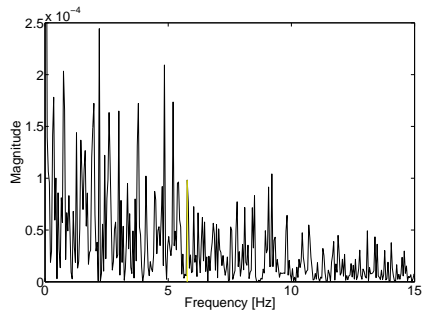
(e) Autospectral density section 2
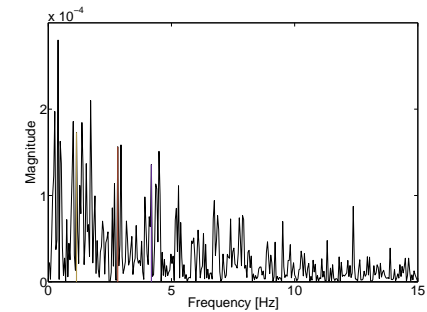
(f) Autospectral density section 12

Figure 5.50: Auto-spectral density plots for some sections within sub-event IV. Similar frequencies are highlighted with the same color.

5.3 Discussion of Local Panel Analysis

5.3.1 Time Domain Analyses

Based on observations from under water cameras, I-Scan and test results from two test series we have attempt to determine an indentation speed, at witch ductile to brittle transition takes place. Results from indentation test we have analyzed correspond to findings by Sodhi (1998), using a segmented indent in freshwater ice. Time-history plots at medium speed events (<80 mm/s) in test 4300 shows a typical sawtooth pattern. Forces gradually increased before they reached a maximum value and suddenly dropped to a near-zero value. A clear indication of an intermittent crushing regime. This pattern was harder to recognize with increasing velocities. At higher indentation velocities (>90mm/s) random occurrence of peak forces were observed from global forces and local forces within different sections. Indicating a random or non-simultaneous failure of ice. Data from lower velocity tests tended to have higher variation about the mean force, than forces from sub-events at higher velocities. Similar force trends were found from both global forces acting on the sensor template and local forces, with some exceptions. Due to accumulated ice rubble from the middle of the indenter out towards the edges less dynamic action was observed here. Regardless of velocities, irregular force distributions were found in sections one and thirteen. Magnitudes of force peaks were lower than what was found for other sections. Lower magnitude may be explained by positioning of the sensor. Sections one and thirteen was placed in such an angle that they was exposed to low normal forces forces, see figure 5.51. Forces implemented was a product of both normal- and shear forces. When removing sheer forces from local forces found in sections one and thirteen, peak forces were reduced. This indicates that sliding have a large effect on forces towards the edges. A frequent change in pressure area at the edges observed from pressure recordings, support this finding. A non-typical intermittent crushing trend was seen in sections two and twelve for velocity intervals 30 mm/s and 40 mm/s in test series 4300. Also this may be explained by sliding ice material against the edges of the cylinder. In velocities intervals near the transmission velocities were brittle behavior observed near the middle of the sensor. While a typical intermittent curve was found from local forces near the edges.

A transition velocity between intermittent and continuous brittle crushing in test 4300 were found within sub-event six, covering a 80 mm/s velocity interval. In test 3100, signs of a transition velocity was found to be slightly lower. Between 60 mm/s and 70 mm/s. Due to high initial velocity and constant acceleration was there hard to find a transient velocity for test 3100, compared to test 4300. A more exact value was not possible to find. However the velocity found in both test were in the same range and close to findings in previous literature by e.g. Sodhi (1998).

Time-averaged spatial correlations have been presented for all sub-events in both test series. Similar to findings from *JOAI* data reported by Taylor et al. (2010),
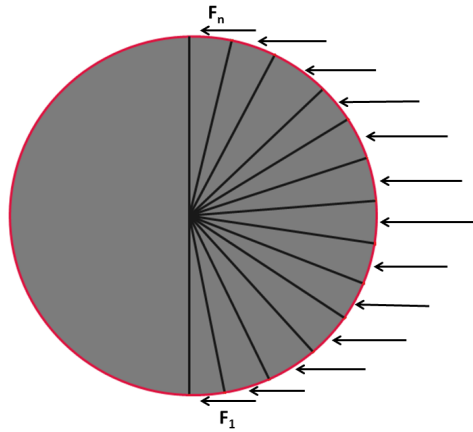
Figure 5.51: Forces in ice drift direction within each section.

our correlation plots show highest correlation between panels for lower speed velocity intervals (<60 mm/s in this cases). In general, increasing velocities show a decrease in correlation. Due to the non-uniform pressure distribution during high-speed events, an overall low correlation were there expected to found with slightly higher correspondence between immediately adjacent sections. Within sub-events where intermittent crushing dominated correlation coefficients were more uniformly distributed between sections, as seen in figure 5.6a. With increasing velocities the correlation between distant panels in general decreased, with a few exceptions that seemed to be random as figure 5.36a. Due to equal units along the diagonal of the correlation matrix highest correlation was expected to be found here. According to section 2.3.3, self-correlations along the diagonals were equal to one ($r_{ij} = 1$). Contour plots within some sub-events showed correlation values lower than one on the diagonal. This is most likely to do whit averaged values used to define a correlation between four points. Colors representing a value between two sections point should be read carefully. It was found that number of sections used in implementation and time window evaluated was important for the correlation output. An increased number of sections showed higher correlation between directly adjacent sections and lower correlation between distant sections. From theory in section 2.3.3 we know that correlation values are found from the mean value and standard deviation between two sections. Increasing numbers of sections should decrease the standard deviation between two nearby sections and therefor increase the correlation. However, when using thirteen sections a relatively high correlation was found between immediately adjacent sections. Also this in consistent with Taylor et al. (2010).

During tendencies to frequency lock-in within test 3100 slightly higher correlation was found than shortly after the event. Before the event, higher correlation was observed. Before an event the construction starts to enter a lock-in condition and therefore was higher correlation expected before the event compared to after the

event. Figure 5.52 shows the correlation within a 80 seconds frequency lock-in event at Norströmsgrund lighthouse (Larsen, 2014). Correlations between panels at Norströmsgrund were found to be higher than what was seen from our data. This might be due to the short duration of the event found in test 3100. Tendencies to lock-in in test series 3100 was observed in a 1.4 seconds time window, if a time-lack as mentioned in section 3.4 was hidden in the sensor equipment this may effect the result for such short time windows.
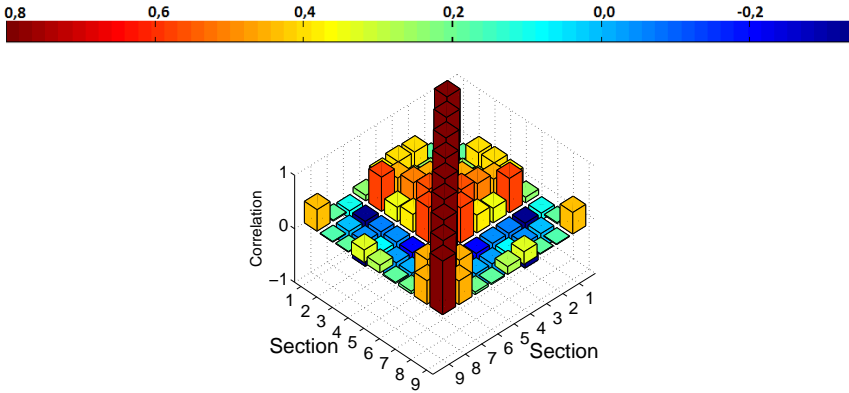
(a) Correlation coefficient matrix 3-D bar chart.
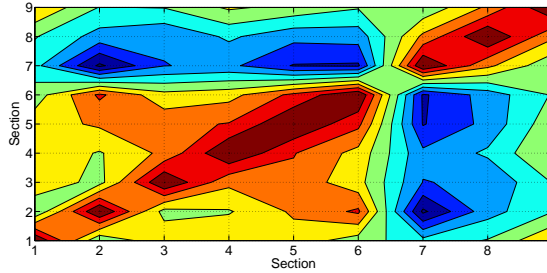
(b) Correlation coefficient matrix contour plot.

Figure 5.52: Data recorded from load panels during a frequency lock-in event at Norströmsgrund lighthouse (Larsen, 2014).

5.3.2 Frequency Domain Analyses

The spectral model first described by Kärnä (2003) was used on tactile sensor data. Manly to investigate the ability to distinguish between different crushing regimes in frequency domain. Data recorded by a tactile sensor was used during cylindrical indenter experiments, recorded in laboratory. A similar study was preformed for a small sub-event in test 4300 as a pre-study before this thesis. Excluding this, there was not found similar studies in former literature. This means that a direct comparison basis was small. For several velocity intervals have auto- and cross-spectral density plots been evaluated in thirteen different sections around the indenter. Two general trends in test series 4300 and 3100 were lower magnitude at peak values and lower frequencies in spectral plots for sections one and thirteen. Both trends may be explained by sliding of extruded ice rubble from the middle of the indenter toward the edges. First of all may resolved extruded material between the indenter and hard ice work as a filter, filtering away higher frequencies. In addition would extruded material work as a damper between the indenter and harder ice. Causing lower magnitude of frequencies peaks.

In accordance to Kärnä and Yan (2009) spectral densities were showing high values in the range of low frequencies at lower velocities. In general, auto- and cross-spectral density plots seemed to fluctuate more with increasing velocities. Higher frequencies were represented and spectral density plots were slower approaching a close to zero-value. Higher frequencies were expected. An increase in velocity would cause higher frequency crushing where pressures is more random and uneven distributed over the indenter. How fast spectral density plots approaching zero may be influenced by noise affecting the sensor. The recorded signals have not ben filtered, and noise would therefor be taken in to the spectral density plots for the time series. How fast plots approaches zero would therefor be a relative value between large and lower peaks. Therefor would noise apparently easier be seen as a part of recordings in spectral density plots for low velocities where highest peaks were observed for low frequencies. Potential noise sources can be the test rig itself or an opening between the sensor and the surrounding aluminum film. An exception from this trends was found in test 3100, sub-event III (150-200 mm/s). Spectral density plots were less fluctuating within this sub-event and approached zero for lower frequencies than what was found for lower velocity events. Further investigations were preformed, but an explanation was not found. Less fluctuation may be due to changes in ice properties ore damages in the ice sheet.

Spectral analyses of test 4300 shows some similar frequencies located around the indenter. Manly for low velocities events (<60 mm/s) and may be seen by comparing velocity intervals 30 mm/s and 80 mm/s. In sub-event one (30 mm/s) most of the recurrent frequencies were found to be less than 4 Hz. During the 80 mm/s velocity interval recurrent frequencies were slightly higher. During sub-event six recurring frequencies was manly found towards the edges of the indenter. In contrast to sub-event one recurring frequencies manly occurred towards the middle of the indenter. Lateral displacement of the indenter was not investigated. Studies

of lateral displacement may explain why highest similarities within sub-event one were found close to the middle of the indenter. Ice properties and propagation of cracks from the middle towards the sides may also explain few similarities towards the edge of the indenter. However, some similar frequencies were symmetrical located around the middle of the indenter. Most of them in lower velocity intervals of test 4300. Dempsey et al. (2000) claims that; *A state of symmetrical deformations is equally unlikely during fast speed events where brittle crushing predominates.* Analyses of both test 4300 and 3100 were indicating otherwise. Some frequencies appeared to be symmetrical located also in sections where brittle crushing clearly prevails. Whether this was random or not should be further investigated where lateral displacements are accounted fore.

In accordance to findings by Pedersen (2012) and Taylor et al. (2010), similar frequencies were found in advance panels. Especially in sub-events were intermittent crushing dominated. This most likely have to do with the division of sections. Witch frequencies who dominated in each section was changing when modifying number of sections used during analysis.

During a lock-in event at the JZ20-2-1 platform was findings of multiple resonance frequencies reported by Duan et al. (2002). This corresponded to findings seen in figure 5.44, from the possible event in test 3100. Yue et al. (2009) stated that the frequency of ice forces was locked in the natural frequency of the structure during an event. This was not the case in test 3100. A resonant frequency was found to be 8.57 Hz during the possible event. First and second mode of the system were calculated to be 9.45 and 14.9 Hz (Nord and Määttänen, 2013). A resonance frequency lower than the first natural frequency is most likely to do with the damping of the free oscillating damped system. Damping was not further investigated in this thesis. As mention in section 2.1.3 reported Kärnä (1994) about resonant frequencies where steady-state vibrations occurred, at frequencies 5 % to 15 % lower than the natural frequency of the structure. The resonant frequency in test 3100 was found to be 9.3 % lower then the first natural frequency of the system. Another finding was a possible sub-harmonic frequency observed in sections four and then during the possible event. Further investigations were not preformed and other lock-in events should be analyzed to say something more about this phenomena. It is important noting that they were only found in two of thirteen sections. However, sections four and ten were symmetrical around the middle of the indenter.

Bjerkås et al. (2006) mentioned that short periods with dominating frequencies may be hard to detect, due to time averaging. This corresponds to experiences during this work. Dominating crushing regimes were difficult to detect, based only on observations from spectral analysis. A preferable and recommended method would be to estimate a possible transition speed from time domain. Then spectral analysis may be used in shorter time windows to support findings. The transition speeds between intermittent and brittle crushing were found to be between 80 mm/s and 90 mm/s in time domain from test series 4300 and between 60 mm/s -70 mm/s for test 3100. A simple synchronization between pressure movies in I-scan and observations from cameras where preformed to support this findings. From

cameras above and below the waterline was a change in trend observed during the 80 mm/s velocity interval. Similar observations were not possible to see from spectral analyses. In general, comparison of frequencies in spectral density plots were time consuming and implementing the spectral model was more demanding than evaluating time domain. It is therefor not a preferable method to determine type of crushing regime acting on a structure.

A flow-chard based on the pre-study of this thesis was illustrated in figure 2.3. In frequency domain was there planned to use a filter on raw data to find coherence functions between panels. Due to satisfying results from correlation in time domain, was coherence functions not found in this thesis. For further interest using filters in dynamic force identification see Lourens et al. (2010).

Chapter 6

Context Between Failure Processes and Pressure Distribution

Both qualitative and quantitative analyses have been preformed on tactile sensor data, in order to attempt obtain a better insight into the associated pressure distribution and mode of ice failure. Visual interpretation of time traces and pressure views in I-Scan have been conducted for both test series 4300 and 3100 analyzed in chapter five. Local contact area have been numerical investigated by using Matlab. Contact areas were found by adding together number of sensing elements exposed to pressure within each section and multiplied with pixel area. Effective pressure generated during an ice- structure interaction depends on several events such as spalling, flaking, size and failure of individual crushing zones and nucleation of cleavage cracks. The influence of time, temperature and scale on formations of *hpz* have been reporter by Dempsey et al. (2000) and within the spring of 2010 were an industry project conducted to investigate the effect of stiffener compliance (Määttänen et al., 2011). In this thesis the influence of ice velocities on *hpz* formation was further explored. It is important to note that the therm *hpz* was in this context, used for areas exposed to pressure larger than 3692 kPa. Areas exposed to pressures higher than 3692 kPa are marked with read in the following pressure distribution pictures taken from I-Scan. As mentioned in chapter three may this legend be changed, and therefor also what may be referred to as *hpzs*. In the following legend values were kept constant to give a consistent picture of pressure changes. Do to a large amount of data, only data from representative regions for each event (Intermittent, tendencies to lock-in and continuous brittle crushing) was represented below. In Appendix C can pressure distributions taken from I-Scan for all sub-events in test series 4300 be seen.

Local panel analysis of test 4300 shows a dominating intermittent crushing regime within sub event-one (30 mm/s). A selected region for failure in this velocity interval are displayed in two and three dimensional spatial pressure maps in figure 6.1. In low velocity ranges where intermittent crushing dominated was there characteristic with a pressure build-up before it released, this may bee seen in from figure 6.1. In general areas with higher pressure was seen directly before a load-droop, however the pressure distribution appeared to decrease mostly near the edges of the indenter. This was consistent with observations reported by Taylor et al. (2010) from analyses of tactile sensor data conducted at the JOIA test campaign.

| 0 | 308 | 615 | 923 | 1231 | 1538 | 1846 | 2154 | 2462 | 2769 | 3077 | 3385 | 3692 kPa |

(a) 2-D Pressure distribution before failure.   (b) 2-D Pressure distribution after failure.

(c) 3-D Pressure distribution before failure.   (d) 3-D Pressure distribution after failure.

Figure 6.1: Spatial pressure maps taken from a selected region within the 30 mm/s velocity interval in test 4300.

In velocity ranges where continuous brittle crushing predominated, was shapes of contact areas changed in limited extent after failure. Compared to intermittent crushing, a more constant pressure distribution was expected during continuous brittle crushing. Consistent with observations reported by Taylor et al. (2010), reductions in contact area during continuous crushing manly was found around

the periphery of *hpzs*. Regardless of the limited extent of contact area a contact pressure was much less uniform. Time traces recorded by the tactile sensor shows non-simultaneous contact at high velocities. Areas with higher pressure then the surroundings were forming and failing rapidly. As shown in figure 6.2, larger areas with high pressure occurred before the event. After the event pressure zones were decreased and more concentrated near the center of the ice sheet. Decreased intensity of pressure may be due to extrusion of material from the center of the indenter towards the edges. Extrusion of ice rubble at higher velocities were clearly observed from movies recorded both above and below the waterline in test series 4300.

(a) 2-D Pressure distribution before failure.

(b) 2-D Pressure distribution after failure.

(c) 3-D Pressure distribution before failure.

(d) 3-D Pressure distribution after failure.
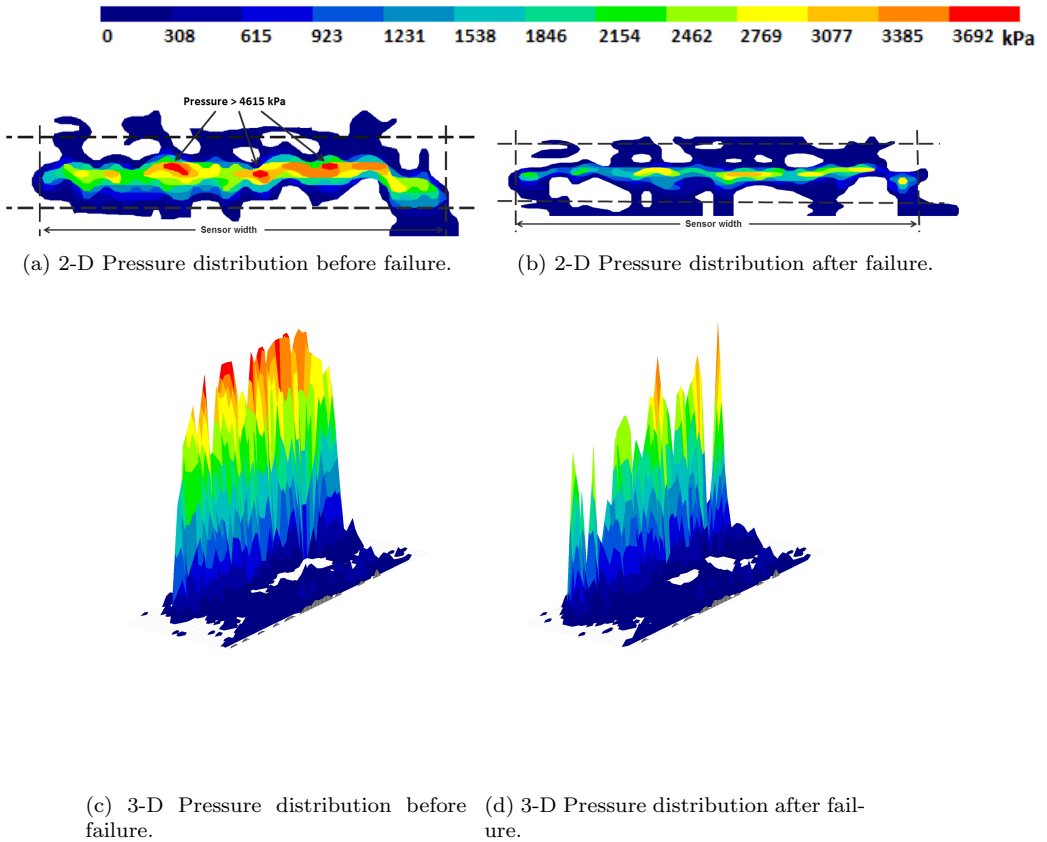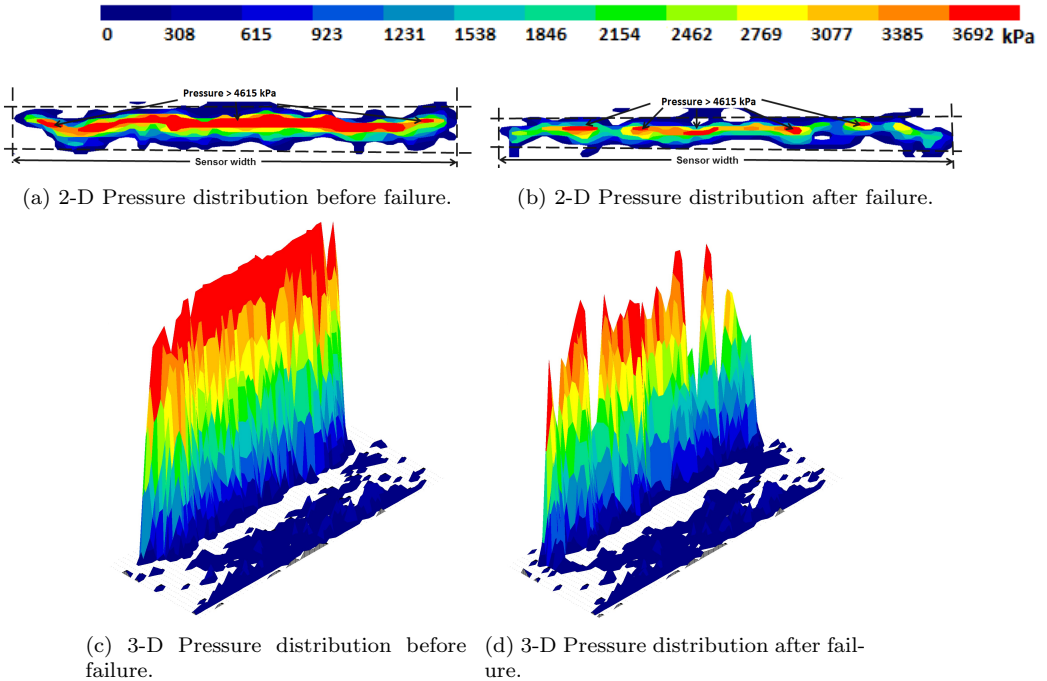
Figure 6.2: Spatial pressure maps taken from a selected region within the 100 mm/s velocity interval in test 4300.

A continual well correlated forming and fading of *hpz* over the indenter was characterized by Dempsey et al. (2000) as line-like contact. This line-like contact or 'line-load' have been reported by e.g. Dempsey et al. (2000), Jordaan et al. (2008), Määttänen et al. (2011) and Frederking (2004). In accordions to Määttänen et al. (2011) line-like contact was found to prevail during continuous crushing, (see figure 6.2). Similar to data from the JOIA test campaign reported by Frederking (2004), a line-like loading distribution was discontinuous across the entire width of the indenter. Highest continuous were observed at the time of the peak load, but even here areas with lower pressure was found especially near the edges of the indenter.
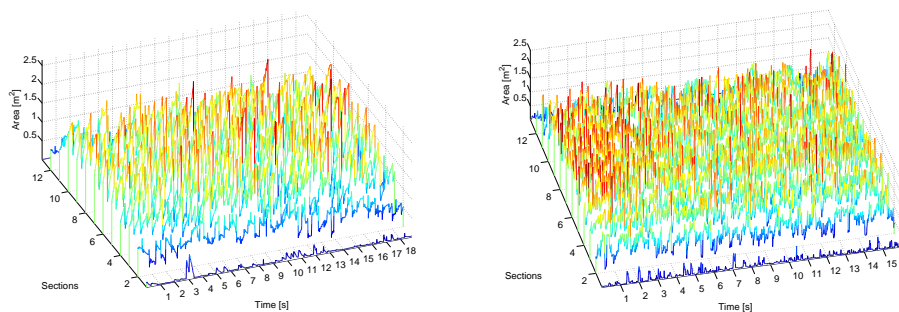
(a) Local contact area in thirteen sections during intermittent crushing.

(b) Local contact area in thirteen sections during brittle crushing.

Figure 6.3: Changes in local contact area within different crushing regimes.

Discontinuous line-like contact was also observed in test 3100.

Figure 6.3 illustrate differences in local contact area during intermittent and brittle crushing. Simultaneous contact may be seen between section three to eleven during intermittent crushing. This in contrast to figure 6.3b showing non-simultaneous crushing.

Through tendencies to frequency lock-in trends of line-like contact was observed from tactile pressure movies, see figure 6.4. As mentioned in section 2.1.3 Yue et al. (2009) was reporting about constant contact during self- excitation events. In test 3100 may constant contact during the event be observed for most of the indenter interface. At the edges reappearing pressure changes were observed from pressure movies in I-Scan. Similar to low indentation speeds simultaneous crushing was found during the possible event. Figure 6.5b illustrates changes in contact area within each section during the possible event. A spatially well correlated contact area may be observed between sections close to the middle of the indenter. Similar trends were found for lower velocities example within the 30 mm/s velocity interval. Changes in local contact area within, before and after tendencies to lock-in may be seen in figure 6.5. Compared to immediately before and after appeared there to be higher consistency in contact area during the possible event.

Independent of velocity a contact line was variating randomly in vertical direction. Most of the time was the contact line seen above the mid ice thickness level. Similar findings were reported by Frederking (2004) on data from the JOAI test campaign and during the Finnish joint industry project. Määttänen et al. (2011) explained this findings with the buoyancy effect and gravity loads. Small vertical stress fields inside the ice sheet with a maximum stress concentration at the waterline could be generated due to the gravity loads and the buoyancy effect. This will lead to a confinement effect which increases the ice strength in lateral direction. Other possible explanation could be changes in ice properties over the ice thickness, such as temperature, salinity, porosity or flaking. Camera filming both below and above

(a) 2-D Pressure distribution before failure.

(b) 3-D Pressure distribution before failure.

(c) 2-D Pressure distribution after failure.

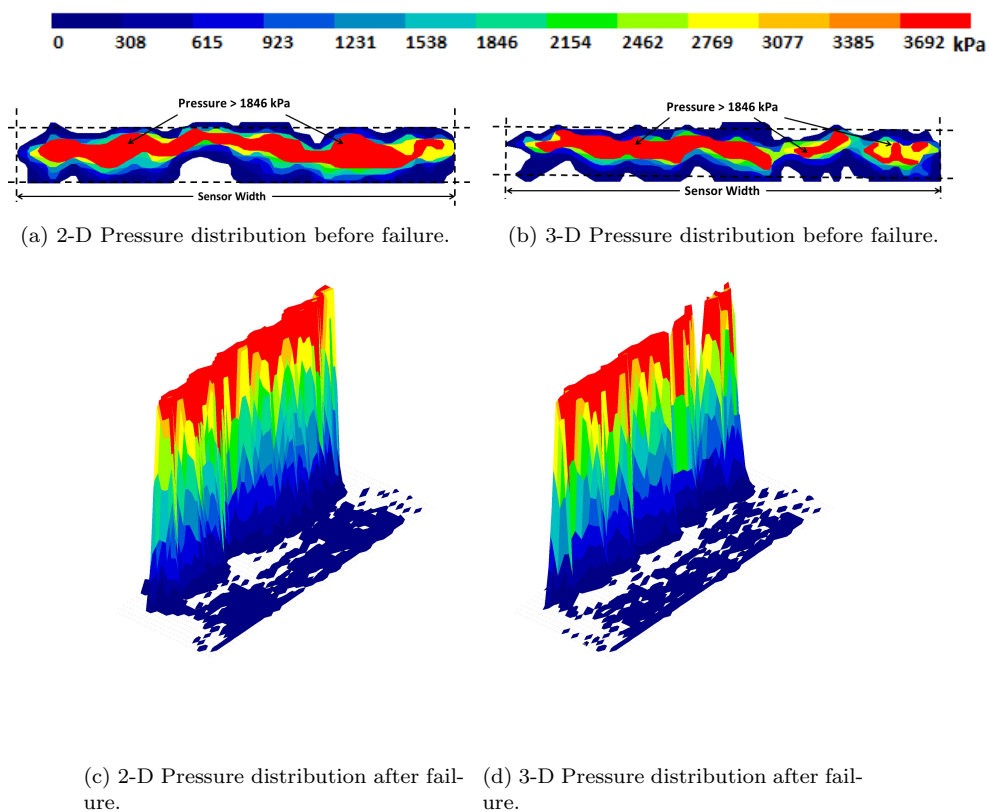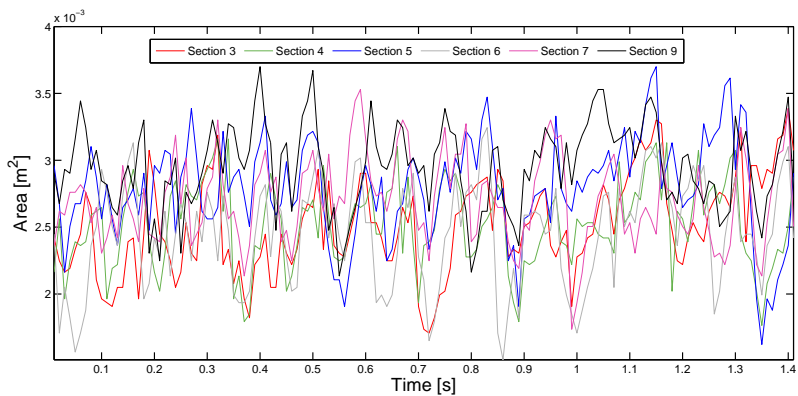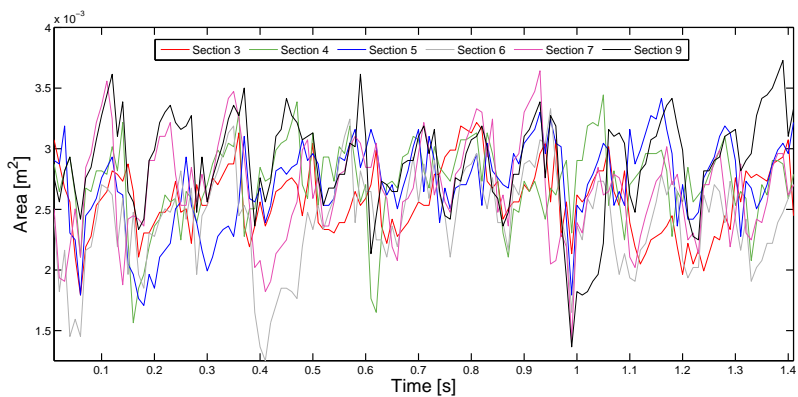(d) 3-D Pressure distribution after failure.

Figure 6.4: Spatial pressure maps taken from a selected region within possible lock-in event.
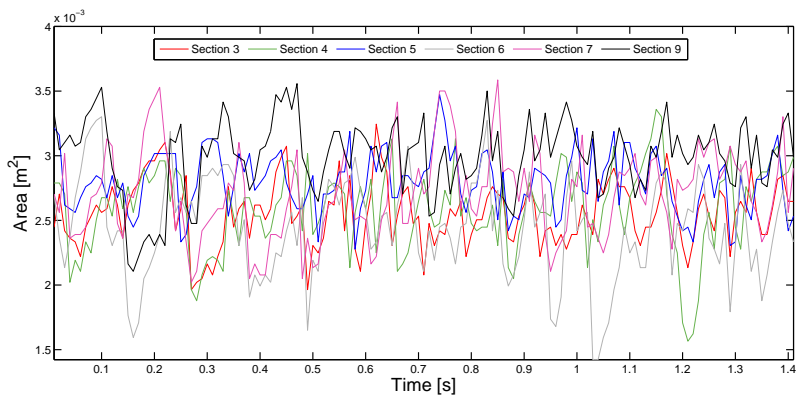
the waterline was examined to see if a possible explanation may bee seen from ice crushing. However, tis gave no answer.

(a) Befor tendencies to lock-in.

(b) During tendencies to lock-in.

(c) After tendencies to lock-in.

Figure 6.5: Time-history plots for changes in local contact area between sections 3,4,5,6,7 and 9 before, after and during the possible event.

Chapter 7

Conclusions

Pressure distribution and characteristics of failure processes along the structural interface have been investigated by time domain analyses, frequency domain analyses and visual characterization. In addition the usability and accuracy of the tactile sensor has been evaluated. The main conclusions are as follows:

- From time domain analyses and visual characterization transition speeds were in the ranges 80- 90 mm/s for test 4300 and 60-70 mm/s for test 3100.

- Local forces were changing over the indenter width. Different crushing regimes were observed at different locations around the indenter.

- By comparing trends in plots, the correlation length parameter was found to decrease with increasing indentation velocities. Higher correlation was registered between panels at velocities where an intermittent crushing regime were dominating. During brittle non-simultaneous crushing the overall correlation was low, except between immediately adjacent sections.

- Distinguishing between different crushing regimes in frequency domain was difficult. A few more frequencies occurred in velocity intervals where intermittent crushing dominated, compared to intervals there non- simultaneous crushing occurred. Few cases of symmetry around the indenter were found. Where this occurred seemed to be more or less random.

- During a possible lock-in event in test 3100, a slightly higher correlation was found in time domain during the event compared to before and after. Frequency domain analyses reviled a resonant frequency occurring in all sections at 8.57 Hz. The natural frequencies of the system was 9.45 and 14.9 Hz. In addition a possible sub-harmonic frequency was observed in two sections.

- Line-like contact prevailed during continuous crushing.

- During tendencies to frequency lock-in, a more simultaneous contact between sections were observed compared to directly after the event.

Hammer excitations and compression test of ice was preformed to investigate the tactile sensors ability to reconstruct rapid pressure changes. In addition an experimental calibration routine to calibrate the sensor was sought. The main experiences were as follows:

- A tactile sensor recording with 100 Hz, failed reconstructing a hammer-impact excitation.

- Satisfying materials to use during calibration was found to be POM and plexiglas.

- Outputs from tactile sensors were strongly dependent of calibration files. To achieve larger possibilities with recalibration should there be used a low sensitivity in the initial calibration file.

- Calibration for high ice-loads proved to be difficult when 25 % of sensing elements should be loaded.

- The tactile sensor was well reconstructing loads and areas of pressure during a compression test where the ice-sample gain a ductile behavior.

7.1 Suggestions for Further Work

To achieve more information about failure processes and the tactile sensor, the following things may be preformed:

- Check possible time lag in tactile sensor data. Investigate if there are better ways to compare tactile data with data from other measurement divides.

- Perform a statistical study on the stationarity of an ice crushing process.

- Preform laboratory experiment with exact known contact area. Examine how pressure between pixels are distributed.

- Assume a random stationary process and use a filter to find the coherence function in frequency domain. Compare findings in the coherence with different crushing regimes.

- In test 3100 was tendencies to frequency lock-in hard to discover in the frequency domain. Perform a more detailed study to see if dominating frequencies may be found in other lock-in phenomenas. Investigate how the damping of the system is effecting this resonance frequency.

- Collect data and lock at the effect of sub-harmonic frequencies.

- Perform field work and investigate how ice features affect changes in contact area and transmission velocities between failure modes.

- Perform compression tests in cold environments and try to obtain controlled brittle failures. Use tactile-and load cell data to analyze how accurate a tactile

sensor may reconstruct fast events in ice. Suitable compression apparatus for this purpose may be *Knekkis* in the cold lab at *UNIS* or *Kompis* out in the filed.

Bibliography

Bendat, J. S. and Piersol, A. G. (2010). *Random Data- Analysis and Measurment Procedures.* Wiley, Hoboken, New Jersey.

Bjerkås, M. and Skiple, A. (2006). Occurrence of continuous and intermittent crushing during ice-structure interaction. Technical report, Norwegian University of Science and Technology.

Bjerkås, M., Skiple, A., and Røe, O. I. (2006). Ice pressure variations during indentation. *Engineering Structures.*

Blenkarn, K. (1970). Measurement and analysis of ice forces on cook inlet structures. Technical report, Pan American Petroleum Corp.

Dempsey, J., Palmer, A., and Sodhi, D. (2000). High pressure zone formation during compressive ice failure. Technical report, Department of civil and environmental engineering, Clarkson University.

Duan, Z., Ou, J., and Spencer, B. (2002). Investigation of ice forces on jacket platform structures: In-situ measured data on jz20-2-1 platform in the china bohai sea. In *15th ASCE Engineering Mechanics Conference.*

Engelbrektson, A. (1997). A refines ice/structure interaction model based on observations in the gulf of bothnia. In *Proc. int. conf. offs. mech. arctice. eng., vol 4 OMAE. p. 373- 376.*

Ewins, D. (2000). *Modal Testing; Theory, Practice and Application.* Research Studies Press LTD., 325 Chestnut Street Philadelphia.

Frederking, R. (2004). Ice pressure variations during indentation. *IAHR International Symposium on Ice.*

Granheim, T. I. (2011). Sensor technology for normal stress measurements in geotechnical laboratory. Master's thesis, Norwegian University of Science and Technology.

Gudmestad, O. T., Løset, S., Alhimenko, A. I., Shkhinek, K. N., Tørum, A., and Jensen, A. (2007). *Engineering Aspects Related To Arctic Offshore Developments.* LAN, design.

IEC (2009). Wind turbines. part 3: Design requirements for offshore wind turbines, 2.nd edition.

ISO (2010). Petroleum and natural gas industries -arctic offshore structures (draft).

Jefferies, M. and Wright, W. (1973). Stochastic analysis of ice-structure interaction. In *Proc. int. conf. port and ocean eng. under arctic cond.*

Jefferies, M. and Wright, W. (1988). Dynamich response of molikpaq to ice-structure interaction. In *Proc. int. conf. offs. mech. arctic. eng., vol 4.*

Jordaan, I. J. (2000). Mechanics of ice-structure interaction. Technical report, Memorial University of Newfoundland.

Jordaan, I. J., Wells, J., Xiao, J., and Derradji-Aouat, A. (2008). Ice crushing and cyclic loading in compression. *IAHR International Symposium on Ice.*

Kärnä, T. (1994). Steady-state vibrations of offshore structures. In *Hydrotechnical Construction, Vol. 28, No. 8.*

Kärnä, T. (2003). A spectral model for dynamic ice actions. Technical report, VTT Technical research center of Finland.

Kärnä, T. and Yan, Q. (2009). Analysis of the size effect in ice crushing - edition 2. Technical report, VTT Technical research center of Finland.

Larsen, E. S. (2014). A numerical simulation of ice-structure interaction. Master's thesis, Norwegian University of Science and Technology.

Lourens, E., Reynders, E., Lombaert, G., Roeck, G., and Degrande, G. (2010). Dynamic force identification by means of state augmentation: a combined deterministic-stochastic approach. In *Proc. int. conf. on Noise and Vibration Engineering. ISMA2010-USD2010.*

Lourens, E. M. (2012). *Force Identification in Structural Dynamics*. PhD thesis, Katholieke Universiteit Leuven, Faculty of Engineering.

Lu, W. (2013). Experience with the i-scan system. Technical report, Norwegian University of Science and Technology.

Määttänen, M. (1981). Laboratory tests for dynamic ice-structure interaction. Technical report, Sustainable Arctic Marine and Costal Technology (SAMCoT).

Määttänen, M., Løset, S., I.Metriki, S.Sukhorukov, Metrikine, A., Evers, K.-U., Hendrikse, H., Lønøy, C., and Nord, T. (2012). Novel ice vibration testing in a large-scale facility: Deciphering ice induced vibrations, part 1. Technical report, Sustainable Arctic Marine and Costal Technology (SAMCoT).

Määttänen, M., Marjavaara, P., Saarinen, S., and Laakos, M. (2011). Ice crushing tests with variable structural flexibility. *Cold Regions Science and technology.*

Määttänen, M. and Reddy, D. (1973). Ice-structure interaction studied on a lighthouse in the gulf of bothnia using response spectrum and power spectral density function analyses. In *Proc. int. conf. port and ocean eng. under arctic cond.*

Newland, D. (1984). *An introduction to Random vibrations and spectral analysis, second edition.* Longman, Essex CM20 2JE, England.

Nord, T., Lourens, E.-M., Øiseth, O., and Metrikine, A. (2014). Model-based force and state estimation in experimental ice-induced vibrations by means of kalman filtering, crst, under review. In *Nord T., +++ 2014. Superstructure influence on ice-induced vibrations by means of input-state estimation and pressure measurements.*

Nord, T. S. and Määttänen, M. (2013). Frequency domain force identification in ice-structure interaction. Technical report, Sustainable Arctic Marine and Coastal Technology (SAMCoT).

Pedersen, C. Y. (2012). Time and frequency domain analysis of input data in dynamic ice-structure interaction. Master's thesis, Norwegian University of Science and Technology.

Peyton, H. (1966). Sea ice strength. Technical report, Final report for the Navy Office of Naval Research. Geophysical Institution, University of Alaska.

Sodhi, D. S. (1988). Ice induced vibration of structures. *IAHR International Symposium.*

Sodhi, D. S. (1989). Ice- structure interaction during indentation tests, in ice-structure interaction. Technical report, St. Johns, New Foundland.

Sodhi, D. S. (1998). Nonsimultaneous crushing during edge indentation of freshwater ice sheets. *Cold Regions Science and technology.*

Sodhi, D. S. (2000). Crushing failure during ice-structure interaction. Technical report, U.S Army Cold Regions Research and Engineering.

Sodhi, D. S. and Haehnel, R. B. (2003). Crushing ice forces on structures. *Journal of Cold Regions Engineering.*

Sodhi, D. S., Takeuchi, T., Nakazawa, N., Akagawa, S., and Saeki, H. (1998). Medium-scale indentation tests on sea ice at various speeds. *Cold Regions science and technology.*

Taylor, R. S., Eng, B., M.Eng, and P.Eng (2010). Analysis of scale effect in compressive ice failure and implications for design. Technical report, Memorial University of Newfoundland.

Taylor, R. S., Frederking, R., and Jordaan, I. J. (2008). The nature of high pressure zones in compressive ice failure. Technical report, Memorial University of Newfoundland.

Tekscan (1998-2012). *Tekscan Pressure Measurement System - Help File Version 6.1X*. West First Street, South Boston.

Timco, G., Frederking, R., and Singh, S. (1989). The transfer function approach for a structure subjected to ice crushing. *POAC89*.

Yue, Q., Guo, F., and Kärnä, T. (2009). Dynamic ice forces of slender vertical structures due to ice crushing. *Cold Regions Science and technology*.

Appendix A

Official Description of the Master Thesis

NTNU
Faculty of Engineering Science and Technology
Institute of Civil and Transport Engineering

Page 1 of 6 pages

MASTER DEGREE THESIS
Spring 2014
for
Cathrine Yvonne Pedersen

Interfacial study of input data in dynamic ice-structure interaction and evaluation of tactile sensors usability in ice-related problems.

BACKGROUND

In this thesis, we apply the knowledge obtained in the autumn project to identify the failure process along the structural interface by means of time domain analyses, frequency domain analyses and visual characterization. In a second stage, the student seek to develop an experimental routine to calibrate the tactile sensor, based on using classical dynamic excitation methods such as hammer impacts and step relaxation tests.

The difficulties lend towards interpretation of the results, because they are novel and physical explanations are difficult or impossible to find in literature. Therefore the student shall focus on to report the characteristics observed, describe them and if possible, explain them.

TASK

The first stage:
- A flow-chart of how the student want to analyze the data, based on the project, autumn 2013.
- Analyze the velocity effects, from 10 to 300mm/s, report visual characterizations.
- Analyze the velocity effects, from 10 to 300mm/s, Time domain characterizations of local forces/force.
- Analyze the velocity effects, from 10 to 300mm/s, Frequency domain characterizations of local/total forces/force.
- Development of contact areas over time. The contact area is dependent on the lower threshold of pressure. Statistical methods may be used for pressure lower threshold

The second stage:

Under the assumption that a uniaxial compression machine and an impact hammer can be accessed, we seek to assess calibration routines by means of classical experimental dynamic calibration procedures and following the guidelines of the Tactile sensor manual. We have a 100Hz limitation of the tactile sensor, therefore using a hammer impact on a tactile sensor attached to a rigid surface may not give the adequate number of points to reconstruct the force. It is expected that with increasing flexibility of the structure, the

NTNU
Faculty of Engineering Science and Technology
Institute of Civil and Transport Engineering

Page 2 of 6 pages

reconstruction will become better. Softness of the hammer tip may also be changed. After the calibration, we use a MTS machine to compress ice-samples at different indentation rates and compare measured forces for both instruments. Since the contact area is important, step loads can be performed to initialize even surfaces in the ice-sample, hence known contact areas are obtained

Task description

Data recorded by a tactile sensor during the EU-HYDRALAB DIIV test campaign at HSVA in 2011 should used to analyze the velocity effects from 10 mm/s to 300 mm/s both in time domain, frequency domain and visually. Emphasis may be placed on the connection between crushing regimes and initial velocities of ice. But also changes in pressure distribution over the indenter should be addressed. This work is limited to level dynamic ice forces and is only considering data from a tactile sensor. In addition, the usage of a tactile sensor should be evaluated. To get a review over the tactile sensors capacity and possible errors, different calibration routines are assessed. Rapid pressure changes are expected along the ice-structure interface. In order to examine if a tactile sensor would record such rapid changes, a hammer excitation test should be conducted. If reconstruction of a hammer impact impulse fails, the student should do additional tests to evaluate the use of tactile sensor in ice research.

Objective and purpose

The intention of this research is to contribute to the identification on failure processes in ice along a structural interface by considering input data recorded by a tactile sensor. In addition should usability of tactile sensors in ice-structures interaction research be evaluated.

Objectives with this thesis:
- Report characteristics in input data observed within different crushing regimes both in time domain and frequency domain.
- Compare changes in contact area within different crushing regimes and compared them with results from former literature.
- Get to know the tactile sensor system.
- Test different materials and equipment to calibrate the tactile sensor.
- Evaluation of the tactile sensors ability to reconstruct forces during an ice-structure interaction process.

Subtasks and research questions

Interfacial study of input data:
In time domain;
- A transient velocity between simultaneous intermittent crushing and continuous brittle crushing should be found for test series 4300 and 3100.

- Local forces around the indenter should be found to investigate changes in crushing regimes on different locations around the indenter. Different velocity steps/ranges need be evaluated.
- The indenter should be divided into sections.. Find the correlation between each section. How is this correlation effect by the indenter velocity? Evaluate correlation within different crushing regimes.

In frequency domain;
- Make auto- and cross-spectral density plots to evaluate changes in frequencies around the indenter at different velocity steps/ranges.
- Try to find a transient velocity in frequency domain.
- Evaluate if number or location of recurring frequencies on different locations around the indenter may be influenced of the dominating crushing regime.
- The student should consider and evaluate the usability of taking data into frequency domain.

If a frequency lock-in interval is found, should this interval be evaluated as a separate event.
In addition should changes in contact area within different crushing regimes be evaluated and compared to former literature. Results should be supported by visual characterization of movies recorded by cameras above and below the water- line.

Evaluation on usability of tactile sensors in ice-structure interaction research:
- Time should be used to understand how the tactile sensor works and the I-Scan program. Further should effects of different calibration files on the output data be evaluated.
- Evaluate how different materials and loading techniques affects the calibration file.
- Conduct hammer-excitation test to see the ability for the tactile sensor to reconstruct forces from a hammer impulse. If reconstruction fails, evaluated how this affects results from an ice-structure interaction process.

NTNU
Faculty of Engineering Science and Technology
Institute of Civil and Transport Engineering

Page 4 of 6 pages

General about content, work and presentation

The text for the master thesis is meant as a framework for the work of the candidate. Adjustments might be done as the work progresses. Tentative changes must be done in cooperation and agreement with the professor in charge at the Department.

In the evaluation thoroughness in the work will be emphasized, as will be documentation of independence in assessments and conclusions. Furthermore the presentation (report) should be well organized and edited; providing clear, precise and orderly descriptions without being unnecessary voluminous.

The report shall include:
➢ Standard report front page (from DAIM, http://daim.idi.ntnu.no/)
➢ Title page with abstract and keywords.(template on: http://www.ntnu.no/bat/skjemabank)
➢ Preface
➢ Summary and acknowledgement. The summary shall include the objectives of the work, explain how the work has been conducted, present the main results achieved and give the main conclusions of the work.
➢ The main text.
➢ Text of the Thesis (these pages) signed by professor in charge as Attachment 1.

The thesis can as an alternative be made as a scientific article for international publication, when this is agreed upon by the Professor in charge. Such a report will include the same points as given above, but where the main text includes both the scientific article and a process report.

Advice and guidelines for writing of the report is given in "Writing Reports" by Øivind Arntsen, and in the departments "Råd og retningslinjer for rapportskriving ved prosjekt og masteroppgave" (In Norwegian) located at http://www.ntnu.no/bat/studier/oppgaver.

Submission procedure
Procedures relating to the submission of the thesis are described in DAIM (http://daim.idi.ntnu.no/). Printing of the thesis is ordered through DAIM directly to Skipnes Printing delivering the printed paper to the department office 2-4 days later. The department will pay for 3 copies, of which the institute retains two copies. Additional copies must be paid for by the candidate / external partner.

On submission of the thesis the candidate shall submit a CD with the paper in digital form in pdf and Word version, the underlying material (such as data collection) in digital form (e.g. Excel). Students must submit the submission form (from DAIM) where both the Ark-Bibl in SBI and Public Services (Building Safety) of SB II has signed the form. The submission form including the appropriate signatures must be signed by the department office before the form is delivered Faculty Office.

Documentation collected during the work, with support from the Department, shall be handed in to the Department together with the report.

According to the current laws and regulations at NTNU, the report is the property of NTNU. The report and associated results can only be used following approval from NTNU (and external cooperation partner if applicable). The Department has the right to make use of the results from the work as if conducted by a Department employee, as long as other arrangements are not agreed upon beforehand.

Tentative agreement on external supervision, work outside NTNU, economic support etc.

Separate description is to be developed, if and when applicable. See http://www.ntnu.no/bat/skjemabank for agreement forms.

Health, environment and safety (HSE) http://www.ntnu.edu/hse

NTNU emphasizes the safety for the individual employee and student. The individual safety shall be in the forefront and no one shall take unnecessary chances in carrying out the work. In particular, if the student is to participate in field work, visits, field courses, excursions etc. during the Master Thesis work, he/she shall make himself/herself familiar with "Fieldwork HSE Guidelines". The document is found on the NTNU HMS-pages at http://www.ntnu.no/hms/retningslinjer/HMSR07E.pdf

The students do not have a full insurance coverage as a student at NTNU. If you as a student want the same insurance coverage as the employees at the university, you must take out individual travel and personal injury insurance.

Startup and submission deadlines
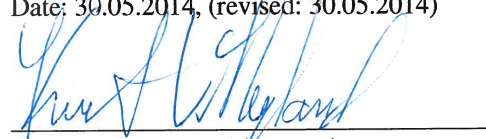
Startup and submission deadlines are according to information found in DAIM.

Professor in charge: Knut Vilhelm Høyland

Other supervisors: Torodd Skjerve Nord

Department of Civil and Transport Engineering, NTNU
Date: 30.05.2014, (revised: 30.05.2014)

Professor in charge (signature)

Appendix B

Calibration Files Made Before the Hammer Impact Excitation

Table B.1: Calibration loads 50.4 N to 246.6 N

Weight [Kg]	Calculated force [N]	Sensor [N]	Deviation [N]	Contact Area [m^2]
5.14	50.4	50.4	0.0	0.0033
15.14	148.5	162.0	13.5	0.0065
25.14	246.6	247.3	0.7	0.0075
35.14	344.7	341.0	3.7	0.0076
45.14	442.8	427.0	15.82	0.0082
54.14	531.1	500.0	31.1	0.0083
83.04	814.6	719.0	95.6	0.0083

Table B.2: Calibration loads 50.4 N to 796.6 N.

Weight [Kg]	Calculated force [N]	Sensor [N]	Deviation [N]	Contact Area [m^2]
5.14	50.4	47.1	3.3	0.0032
15.14	148.5	157.3	8.8	0.0065
25.14	246.6	266.7	20.1	0.0076
35.14	344.7	361.1	16.4	0.0079
45.14	442.8	457.4	14.6	0.0082
54.14	531.1	540.2	9.1	0.0082
83.04	814.6	800.3	14.3	0.0083

Table B.3: Calibration loads 50.4 N to 796.6 N. Loading point was moved toward the edge of the sensor.

Weight [Kg]	Calculated force [N]	Sensor [N]	Deviation [N]	Contact Area [m^2]
5.14	50.4	47.0	3.4	0.0032
15.14	148.5	139.1	9.4	0.0061
25.14	246.6	242.2	4.4	0.0072
35.14	344.7	339.9	4.8	0.0075
45.14	442.8	423.1	19.72	0.0078
54.14	531.1	515.3	15.8	0.0080
83.04	814.6	782.6	32	0.0081

Appendix C

Local panel analyses of remaining velocity steps in test 4300
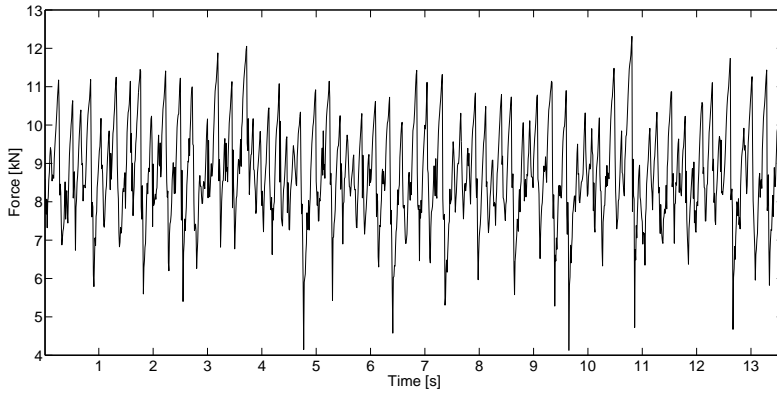
C.1   Sub-Event Two: 40 mm/s

Force Analysis
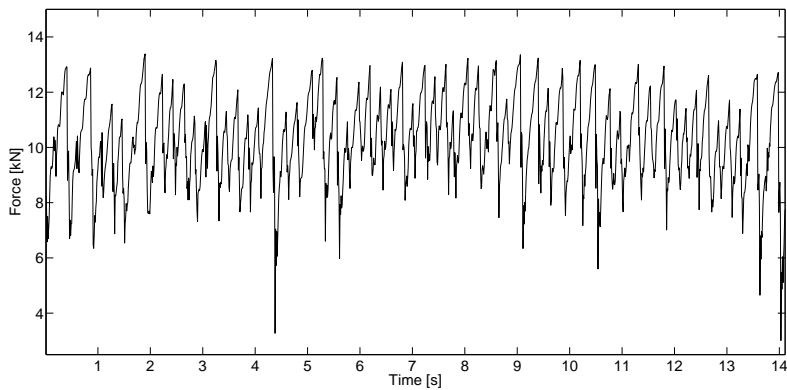
Figure C.1: Global force time-history plots in sub-event two.
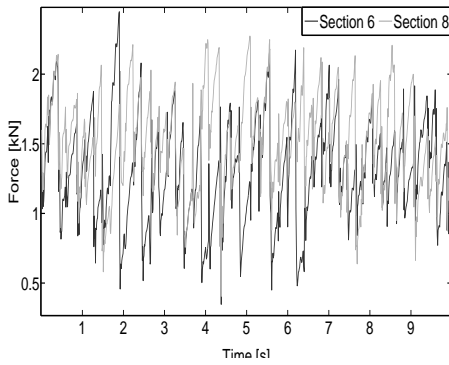
(a) Section six and eight
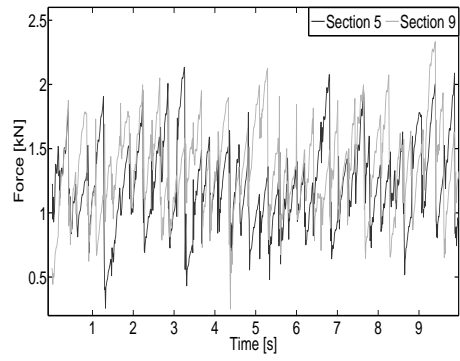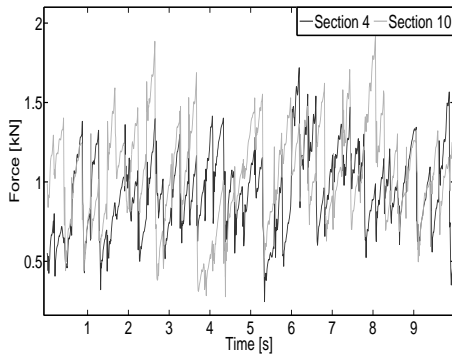
(b) Section five and nine.

(c) Section four and ten.
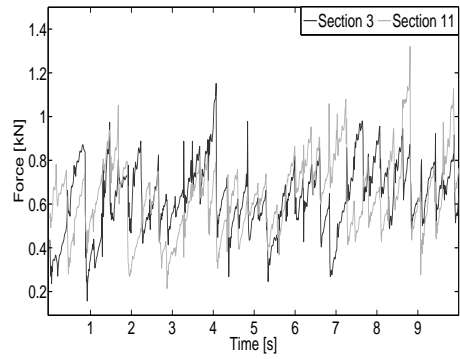
(d) Section three and eleven.
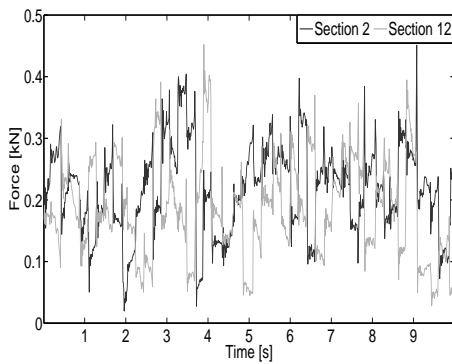
(e) Section two and twelve.
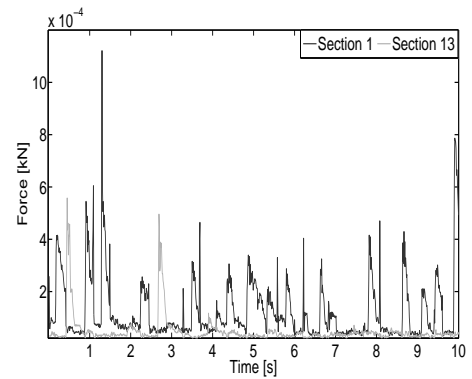
(f) Section one and thirteen.

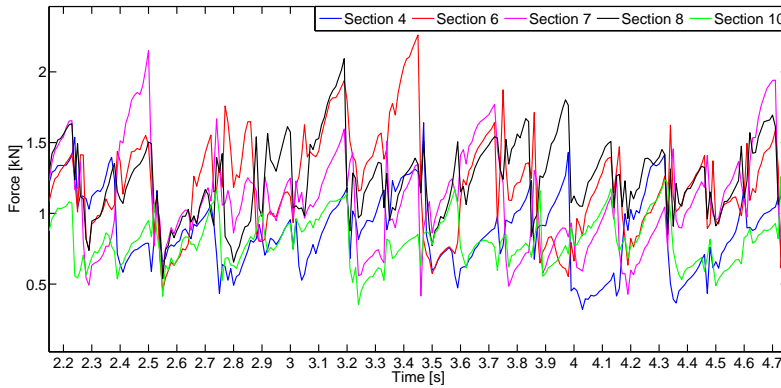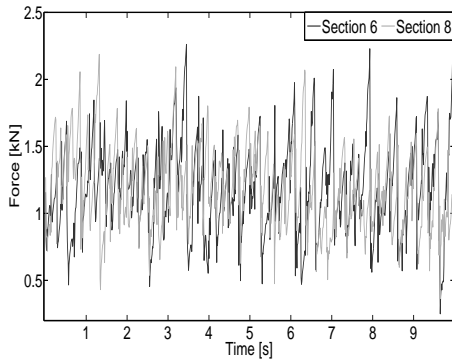Figure C.2: Local forces in symmetrical sections around the middle for velocity 40 mm/s.
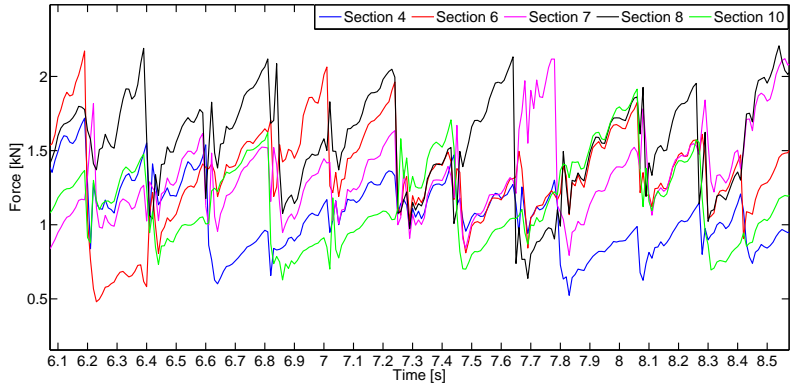
Figure C.3: Comparison between sections 4,6,7,8 and 10 within sub-event two.
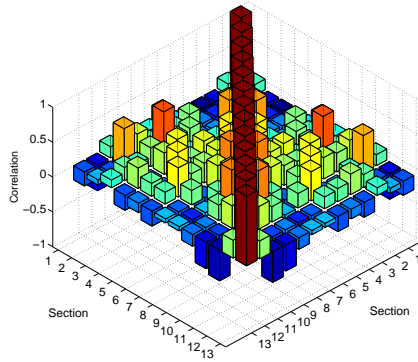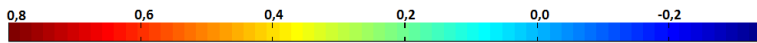
(a) 3-D Correlation coefficient matrix for sub-event two.
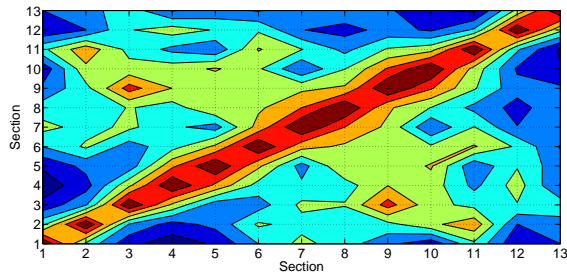
(b) Correlation coefficient contour plot for sub-event two.

Figure C.4: Correlation plots for sub-event two.

Contact Area
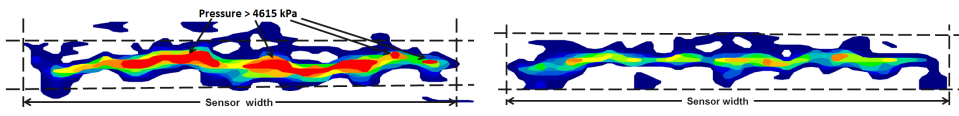
(a) 2-D contour map before failure.

(b) 2-D contour map after failure.
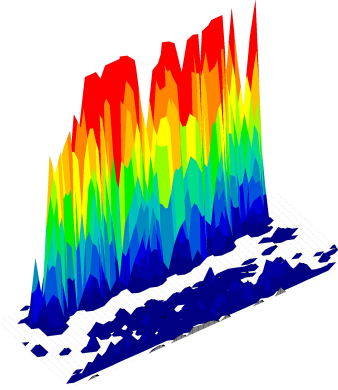
(c) 3-D contour map before failure.
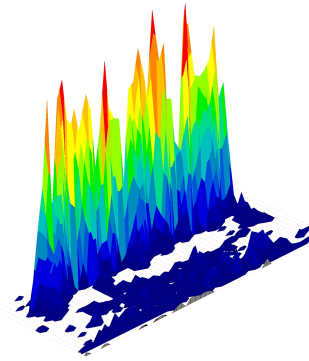
(d) 3-D contour map after failure.

Figure C.5: Pressure distributions of selected regions within sub-event two.

C.2 Sub-Event Three: 50 mm/s

Force Aanalysis
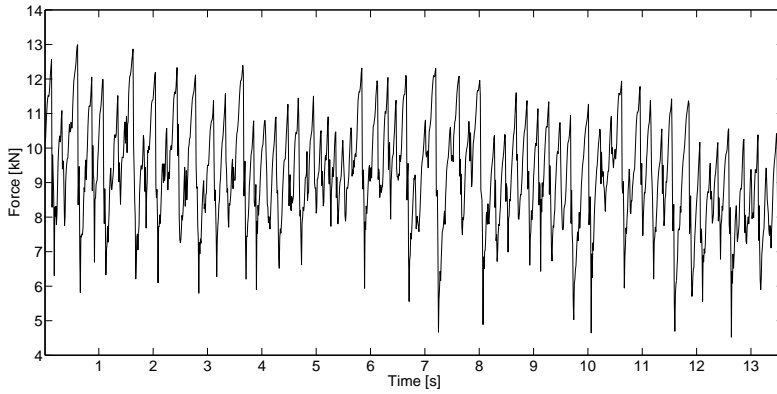

Figure C.6: Global force time-history plots in sub-event three.
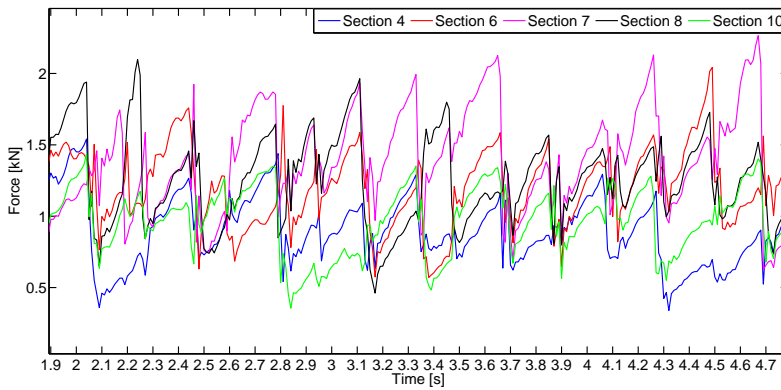
Figure C.7: Comparison between sections 4,6,7,8 and 10 within sub-event three.
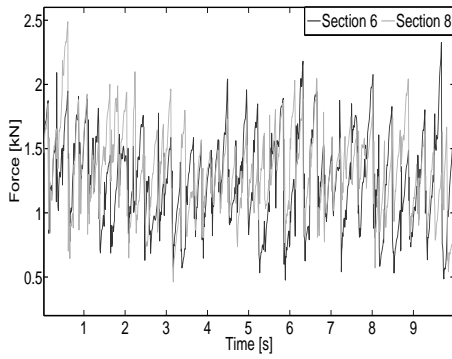
(a) Section six and eight.
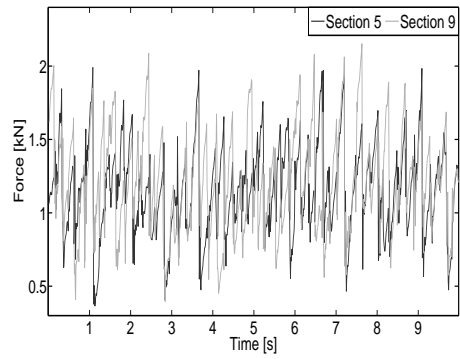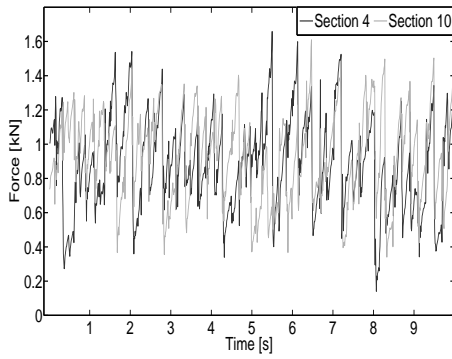
(b) Section five and nine.

(c) Section four and ten.
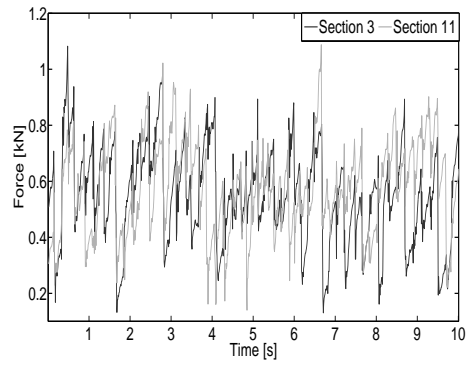
(d) Section three and eleven.
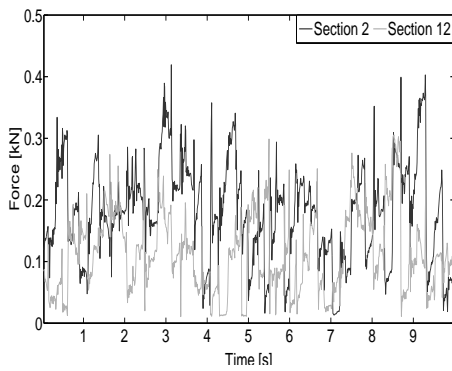
(e) Section two and twelve.
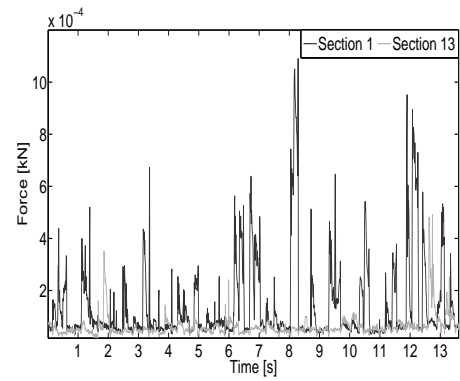
(f) Section one and thirteen.

Figure C.8: Local forces in symmetrical sections around the middle for velocity 50 mm/s.
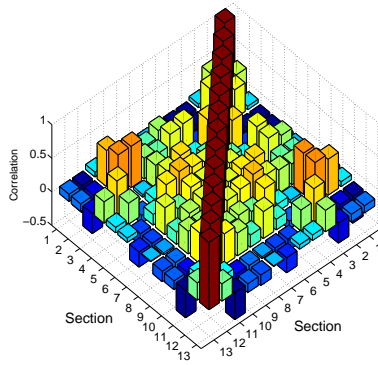
(a) 3-D Correlation coefficient matrix for sub-event three.
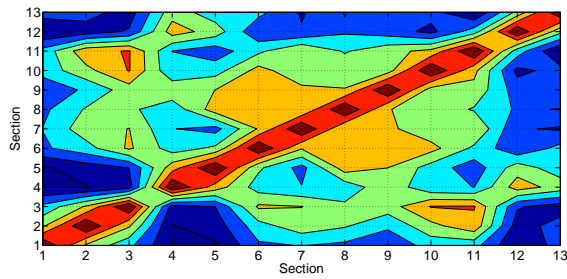
(b) Correlation coefficient contour plot for sub-event three.

Figure C.9: Correlation plots for sub-event three.

Contact Area
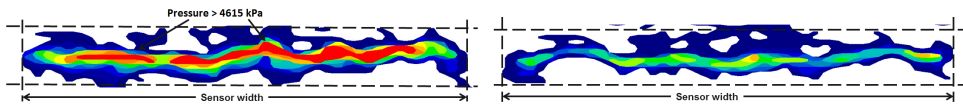
(a) 2-D contour map before failure.

(b) 2-D contour map after failure.
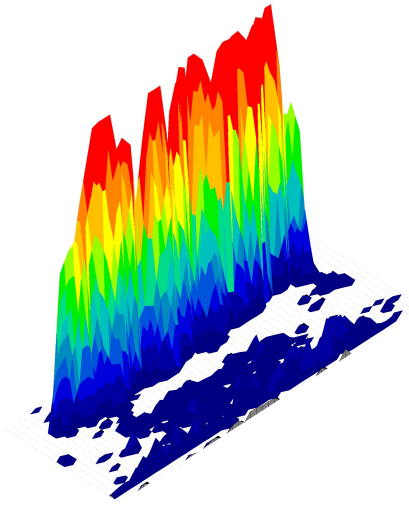
(c) 3-D contour map before failure.
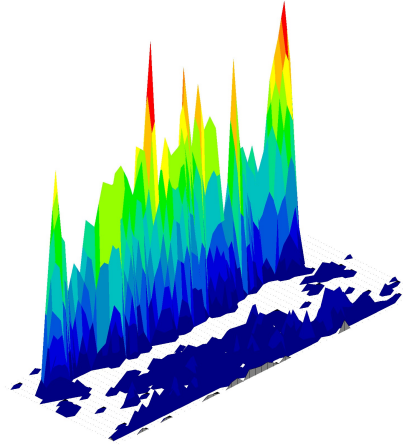
(d) 3-D contour map after failure.

Figure C.10: Pressure distributions of selected regions within sub-event three.

C.3   Sub-Event Four: 60 mm/s

Force Analysis

Figure C.11: Global force time-history plots in sub-event four.

Figure C.12: Comparison between sections 4,6,7,8 and 10 within sub-event four.

(a) Section six and eight.
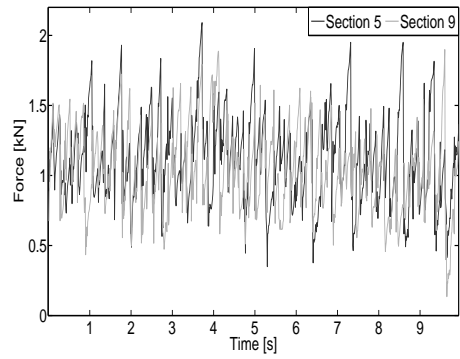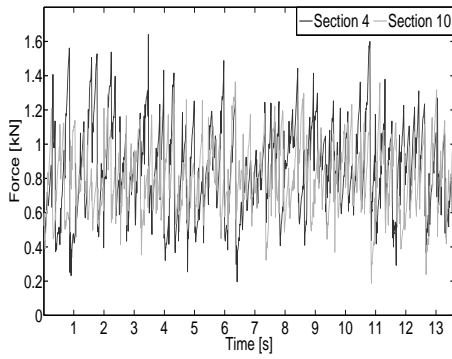
(b) Section five and nine.

(c) Section four and ten.
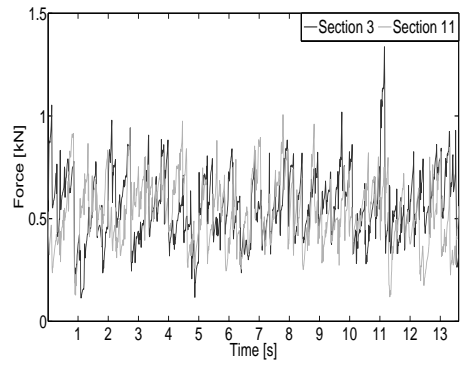
(d) Section three and eleven.
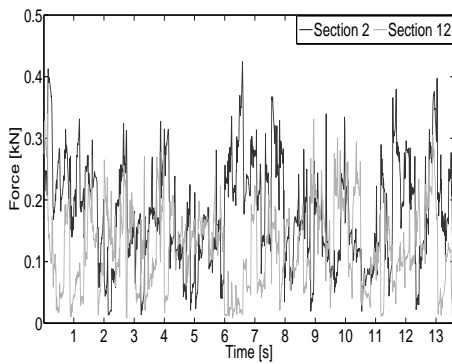
(e) Section two and twelve.
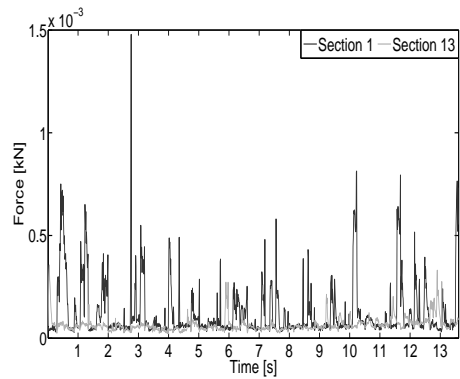
(f) Section one and thirteen.

Figure C.13: Local forces in symmetrical sections around the middle for velocity 60 mm/s.
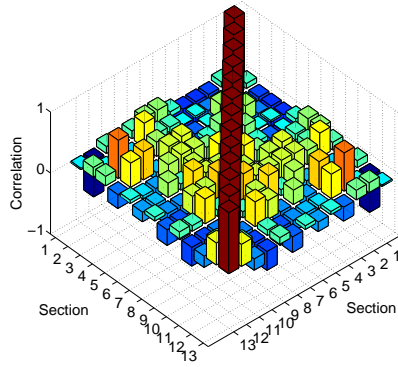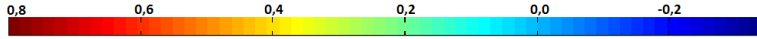
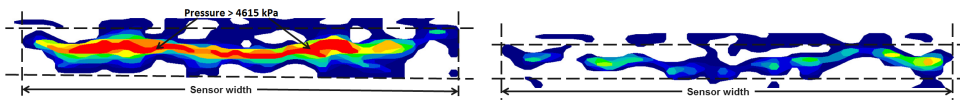(a) 3-D Correlation coefficient matrix for sub-event four.
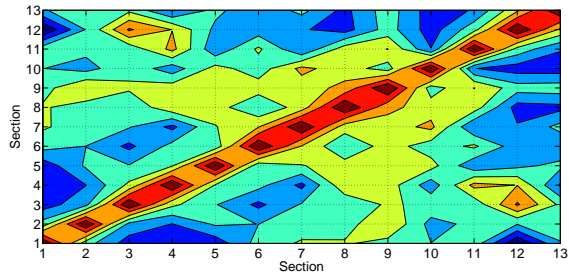
(b) Correlation coefficient contour plot for sub-event four.
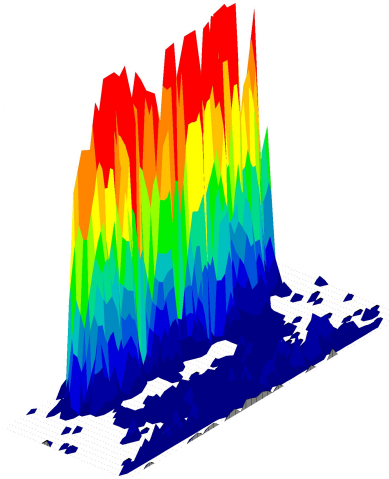
Figure C.14: Correlation plots for sub-event four.
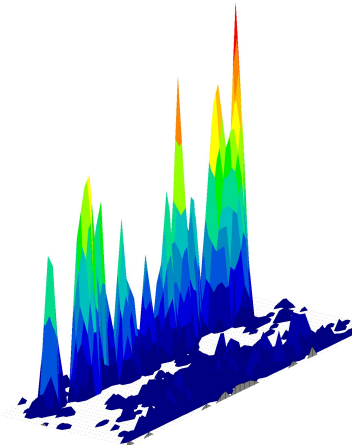
Contact Area

(a) 2-D pressure distribution before failure.

(b) 2-D pressure distribution after failure.

(c) 3-D pressure distribution before failure.

(d) 3-D pressure distribution after failure.

Figure C.15: Pressure distributions of selected regions within sub-event four.

C.4   Sub-Event Five: 70 mm/s

Force Analysis
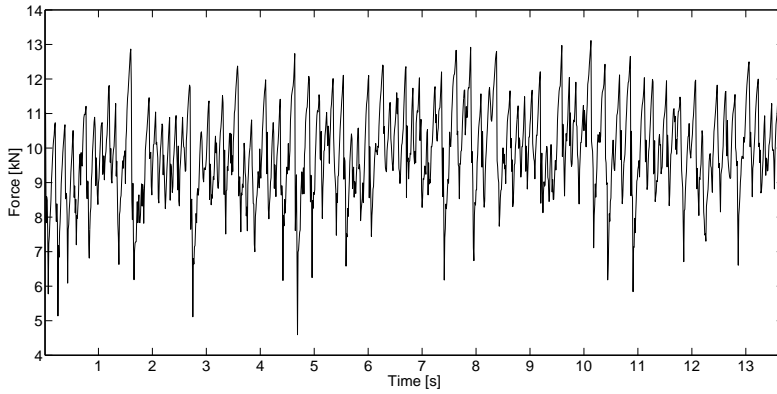

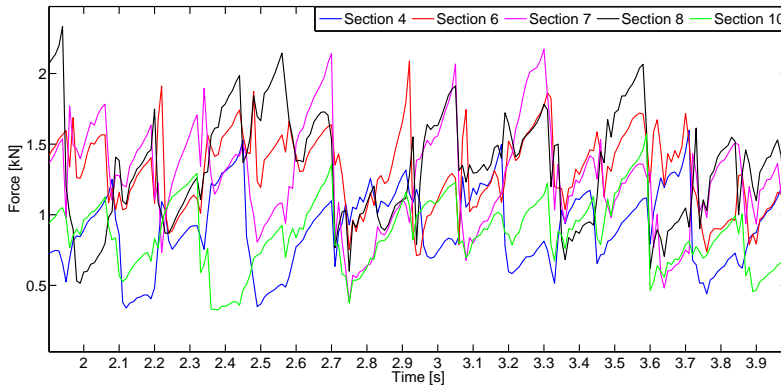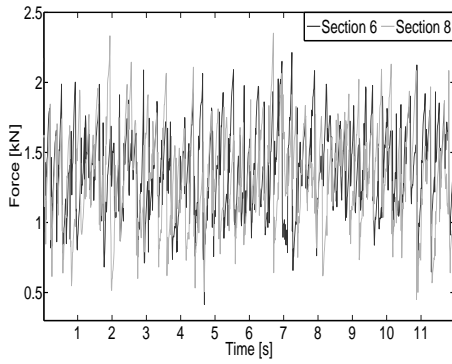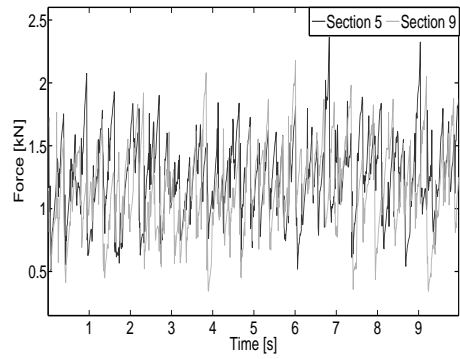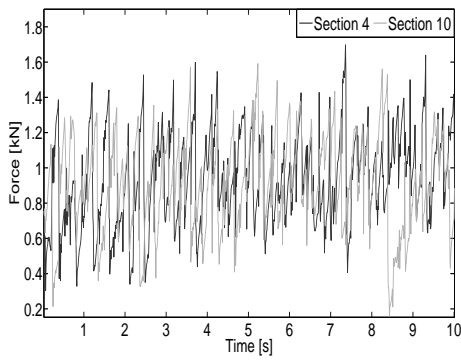Figure C.16: Global force time-history plots in sub-event five.

Figure C.17: Comparison between sections 4,6,7,8 and 10 within sub-event five.

(a) Section six and eight.

(b) Section five and nine.

(c) Section four and ten.
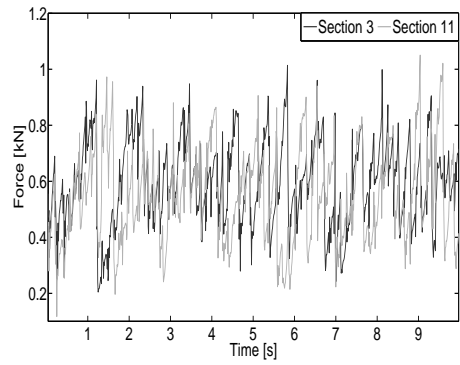
(d) Section three and eleven.
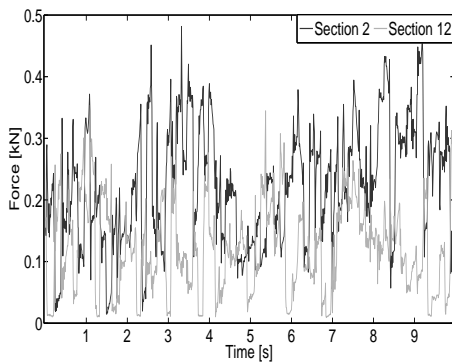
(e) Section two and twelve.
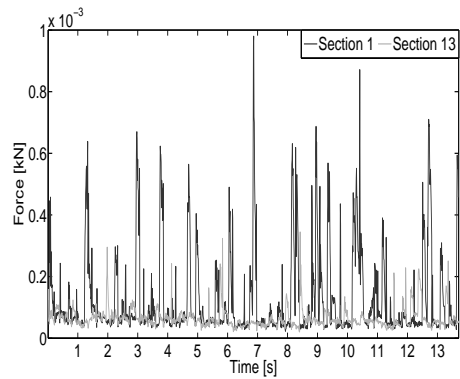
(f) Section one and thirteen.

Figure C.18: Local forces in symmetrical sections around the middle for velocity 70 mm/s.
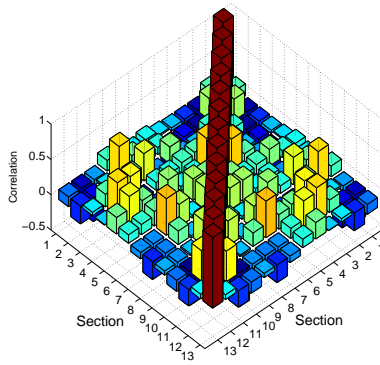
(a) 3-D Correlation coefficient matrix for sub-event five.
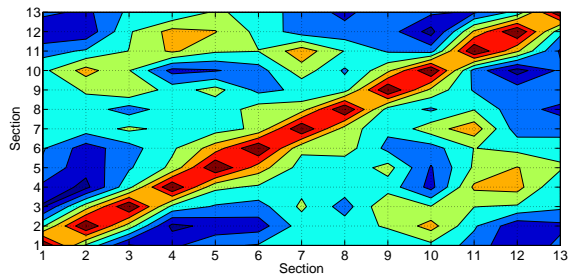
(b) Correlation coefficient contour plot for sub-event five.

Figure C.19: Correlation plots for sub-event five.

Contact Area
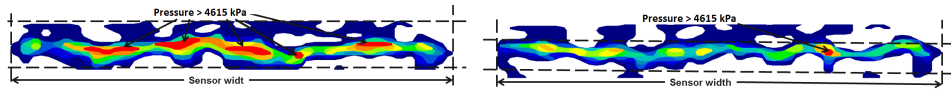
(a) 2-D pressure distribution before failure.

(b) 2-D pressure distribution after failure.
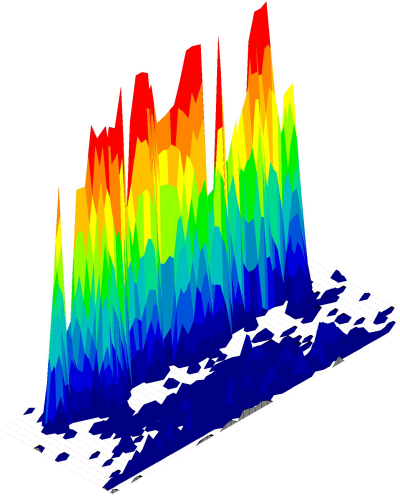
(c) 3-D pressure distribution before failure.
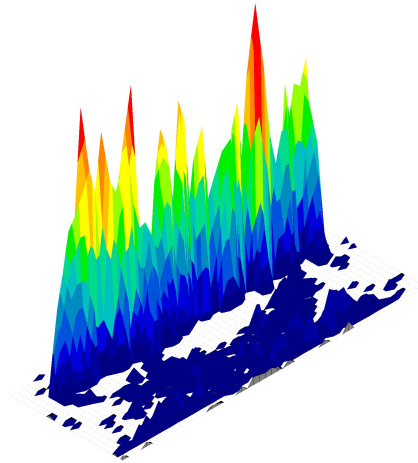
(d) 3-D pressure distribution after failure.

Figure C.20: Pressure distributions of selected regions within sub-event five.

C.5   Sub-Event Seven: 90 mm/s

Force Analysis
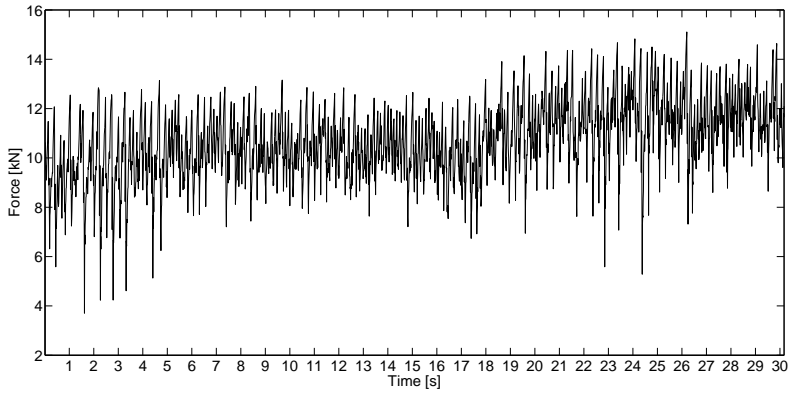
Figure C.21: Global force time-history plots in sub-event seven.
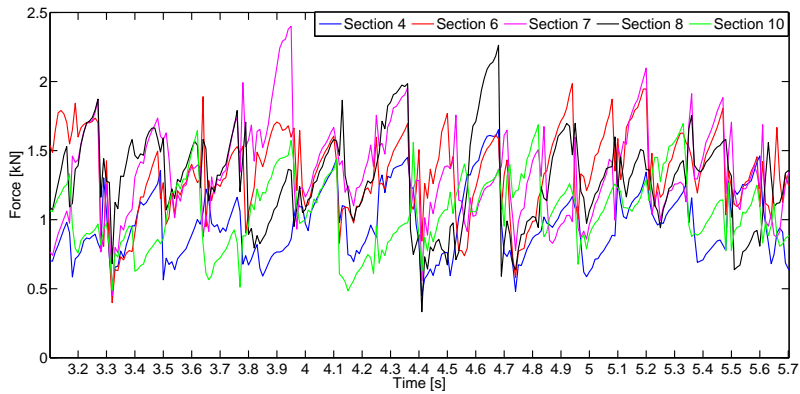
Figure C.22: Comparison between sections 4,6,7,8 and 10 within sub-event seven.
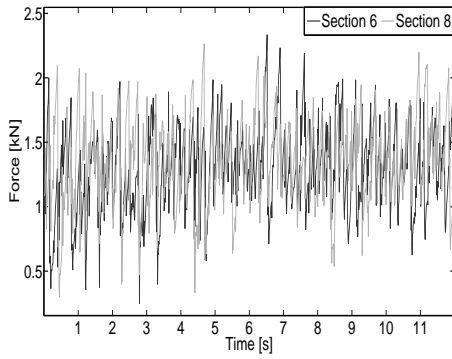
(a) Section six and eight.
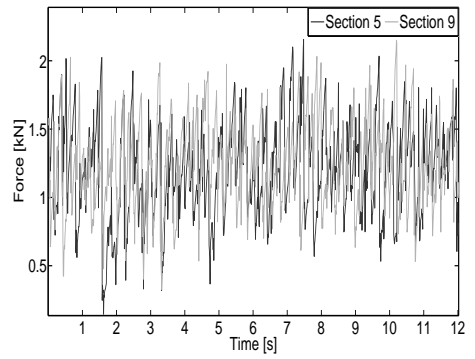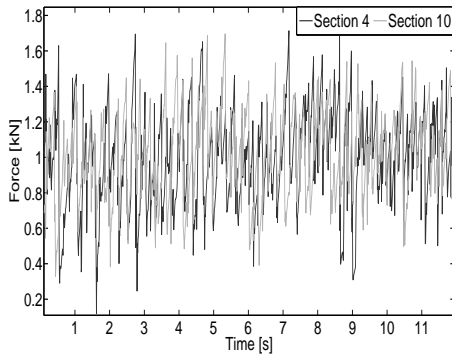
(b) Section five and nine.

(c) Section four and ten.
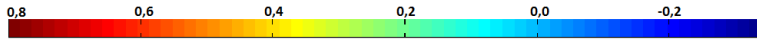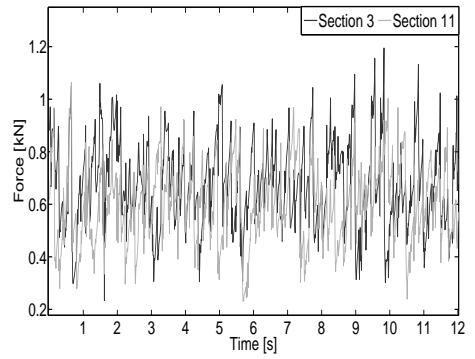
(d) Section three and eleven.
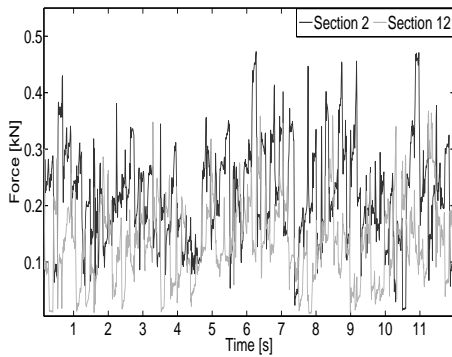
(e) Section two and twelve.
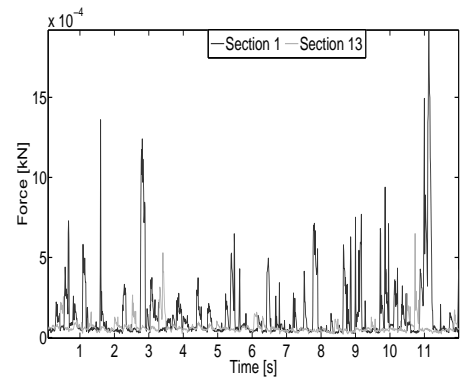
(f) Section one and thirteen.

Figure C.23: Local forces in symmetrical sections around the middle for velocity 90 mm/s.
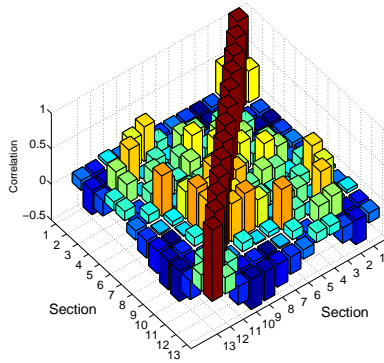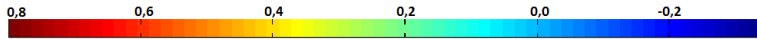
(a) 3-D Correlation coefficient matrix for sub-event seven.
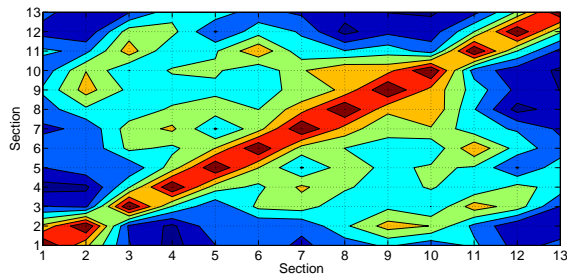
(b) Correlation coefficient contour plot for sub-event seven.

Figure C.24: Correlation plots for sub-event seven.

Contact Area
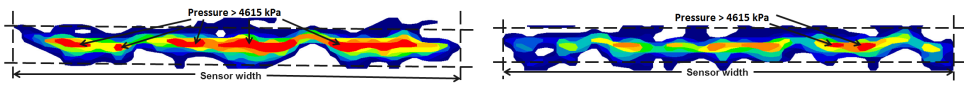
(a) 2-D view before failure.

(b) 2-D view after failure.
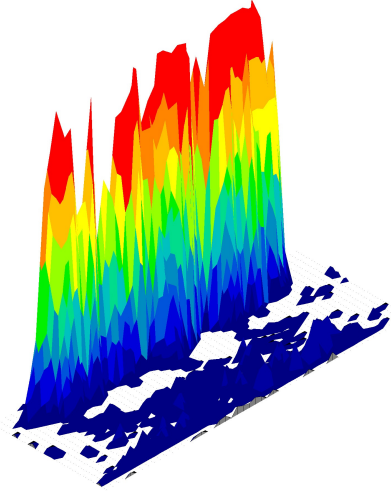
(c) 3-D view before failure.
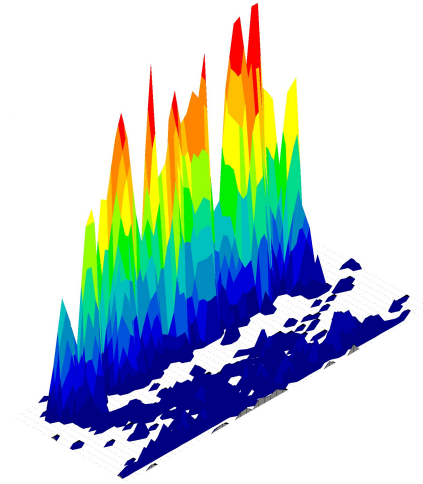
(d) 3-D view after failure.

Figure C.25: Pressure distributions of selected regions within sub-event seven.

C.6 Sub-Event Nine: 200 mm/s

Force Analysis
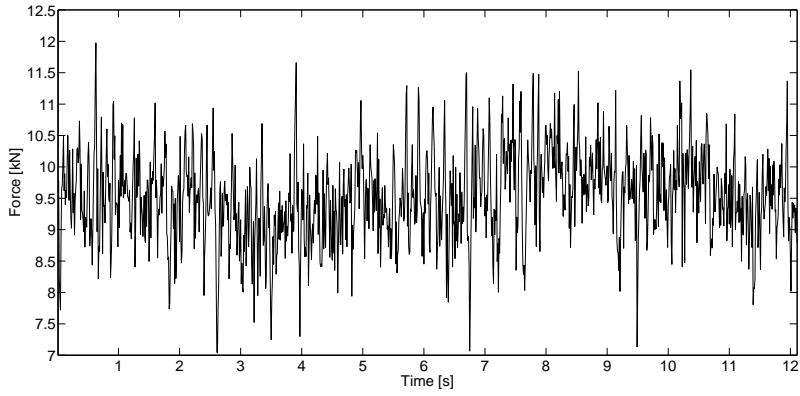
Figure C.26: Time-history plot for sub-event nine.
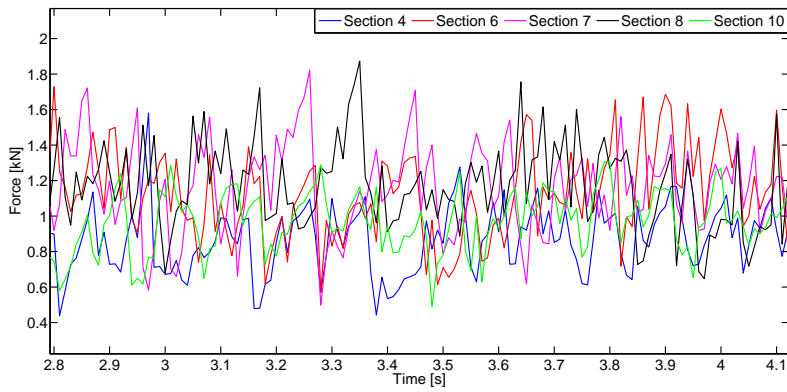
Figure C.27: Comparison between sections 4,6,7,8 and 10 within sub-event nine.
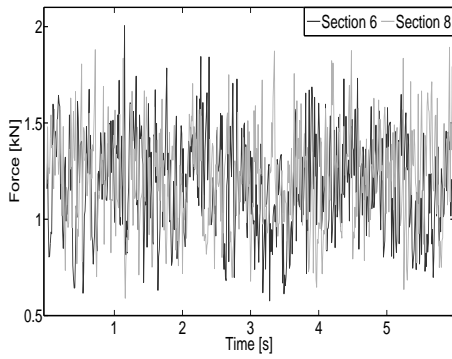
(a) Section six and eight.
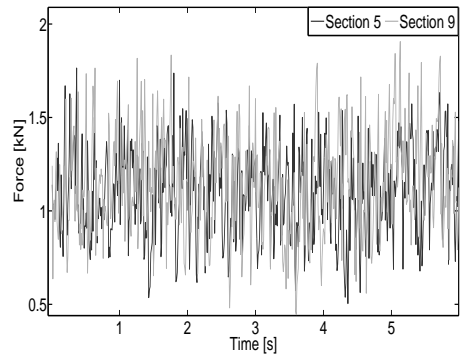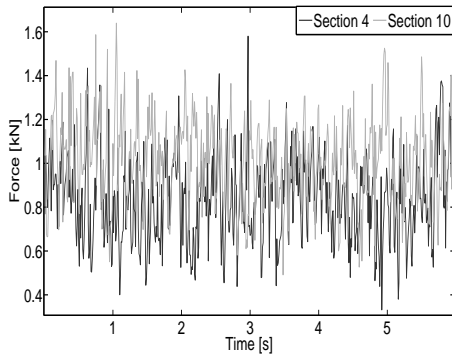
(b) Section five and nine.

(c) Section four and ten.
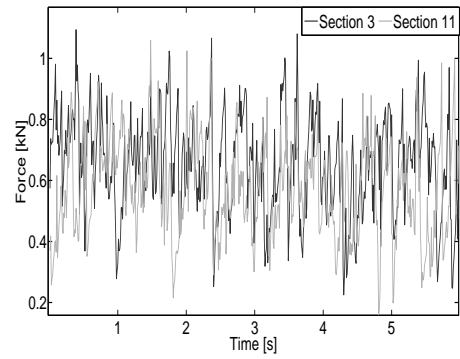
(d) Section three and eleven.
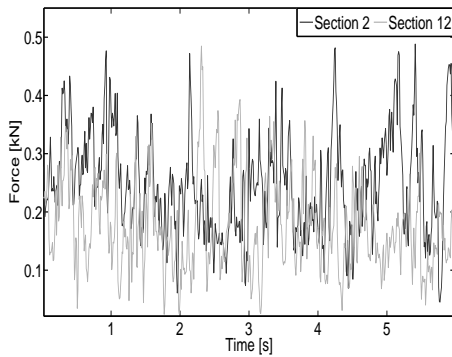
(e) Section two and twelve.
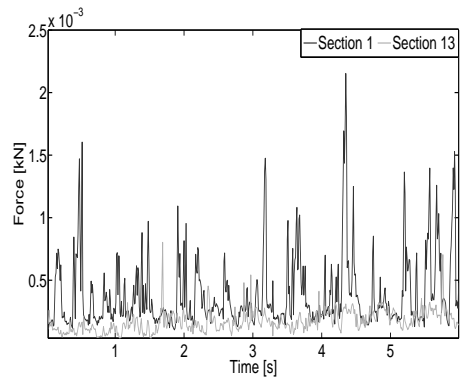
(f) Section one and thirteen.

Figure C.28: Local forces in symmetrical sections around the middle for velocity 200 mm/s.
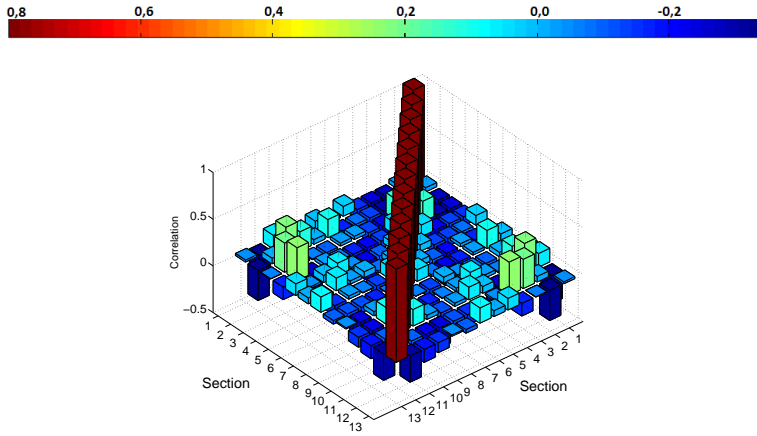
(a) 3-D Correlation coefficient matrix for sub-event nine.
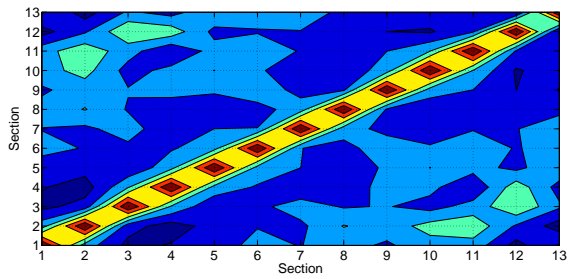
(b) Correlation coefficient contour plot for sub-event nine.

Figure C.29: Correlation plots for sub-event nine.

Contact Area
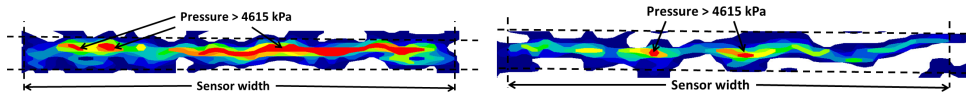
(a) 2-D view before failure.

(b) 2-D view after failure.
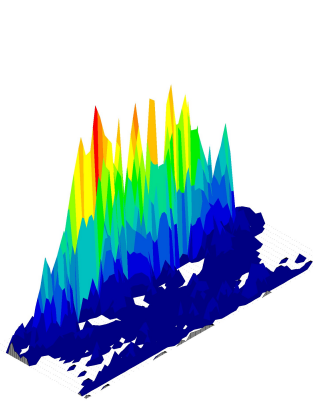
(c) 3-D view before failure.
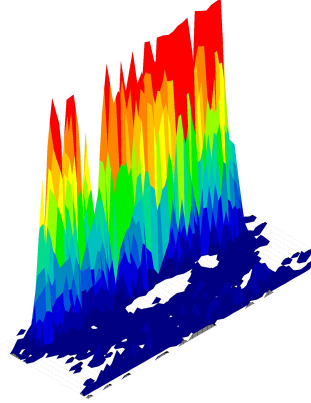
(d) 3-D view after failure.

Figure C.30: Pressure distributions of selected regions within sub-event nine.

Appendix D

MATLAB® Script

A overview of methods used to implement data into Matlab® is submitted in this Appendix. It is important noting that a large part of this thesis have been to process data in Matlab®. Due to a large amount of data only parts assumed to be necessarily are included in this Appendix.

```
clear all
close all
clc
```

Converting .csv- files to .mat- files

```
% fid = fopen(strcat('Series',test_nr,'_M1','.csv'));
% Zeit Shear500 bending600 bending700 laser_01 laser_02 Acc Sync Sx Vx F on
%  the latest tests, 21000 have different column system
% numColsT=9; numHeaders=1;numColsD=5;
% numframes=100;%37626
% format1 = repmat('%s ',1,numColsT); format2 = repmat('%f ',1,numColsD);
% myHeader = textscan(fid, format1,numframes);
% myData = textscan(fid, format2,numframes);
% fclose(fid);


%%%%%%%%%%%%%%%%%%%%%%%%%%%%%%%%%%%%%%%%%%%%%%%%%%%%%%%%%%%%%%%%%%%%%%%%%%%%%
%%                            START OF SCRIPT
%%%%%%%%%%%%%%%%%%%%%%%%%%%%%%%%%%%%%%%%%%%%%%%%%%%%%%%%%%%%%%%%%%%%%%%%%%%%%

HDRS1(1:1730796,1:52)=nan;

format='%f';
for i=1:51
```

```
        format=[format ' %f'];
end
fid = fopen('pressure_4300.csv');
k=0;
while(~feof(fid))
    tline = fgetl(fid);
    if(length(tline)<2)
    elseif(tline(1)=='F')

    else
        k=k+1;
        if((round(k/1000)-k/1000)==0),disp(k),end
         C= textscan(tline,format,'delimiter',',');
         HDRS1(k,1:52)=cell2mat(C);
    end
end
```

Analysis of test series 4300 and 3100

```
%%%%%%%%%%%%%%%%%%%%%%%%%%%%%%%%%%%%%%%%%%%%%%%%%%%%%%%%%%%%%%%%%%%%%%%%%
%%                              START OF SCRIPT
%%%%%%%%%%%%%%%%%%%%%%%%%%%%%%%%%%%%%%%%%%%%%%%%%%%%%%%%%%%%%%%%%%%%%%%%%

% Loading data:

R=26150;                                 % Starting poin
window_length=1590;                      % Interval length
signal_start=R*44+1;
signal_length=44*window_length;
pressuret=load('pressure_4300.mat');
pressure1=pressuret.HDRS1;
p_=zeros(44,52,window_length);
k=0;

for j=signal_start:44:(signal_start+signal_length);
    k=k+1;
    p_(1:44,:,k)=pressure1(signal_start+44*(k-1):signal_start+k*44-1,:);
end
signal_length=k;
```

```
% Geometry and sensor parameters

OL= 0.4161;                              % Overall Length    [m]
OW= 0.6096;                              % Overall Width     [m]
MW= 0.4161;                              % Matrix Width      [m]
MH= 0.1565;                              % Matrix Hight      [m]

n=52;                                    % Number of columns in sensor
r=44;                                    % Number of rows in sensor
s=(180*L)/(pi*(d/2));                    % Angle of sensor range
d=0.220;                                 % Diameter of indenter     [m]


N=13;           % Number of sections used in analyses.
q=N;            % N MUST BE EVEN NUMBER!!! choose N=52, N=26, N=13...


A=(0.4161*0.1565)/N;                     % Local area        [mm^2]
A_pixel=(0.4161*0.1565)/44/52;           % Pixel area        [mm^2]

% Constants

u=0.027;   % Friction coefficient
Fs=100;    % Sampling frequency

% Dividing the sensor area into sections.

A lower and an upper part has to be considered to obtain positive angels
on both sides of the indenter


zone_ang=s/N;                            % Angel of each section
zone_ang=zone_ang*pi/180;                % Angle of each section in radians
tetta_low=zeros(N/2,1);                  % Defining a zero vector.

for j=1:(N/2);                                  % Half sensor range
    tetta_low(j,1)=(zone_ang/2)+zone_ang*(j-1);  % Lower part of the sensor range
end

tetta_high=flipdim(tetta_low,1);    % Upper part of the sensor range
tetta= [tetta_high;0;tetta_low];    % Angle for each section, from the middle
tetta_abs=abs(tetta);               % Taking the absolute value of tetta.
```

```
% Establishing column vectors B and C.

C=cos(tetta);                    % Returns an array of the same size as tetta
B=sin(tetta_abs);                % Returns an array of the same size as tetta
B0=zeros(N,signal_length);       % Defining a zero vector.
C0=zeros(N,signal_length);       % Defining a zero vector.

% Calculating Normal F__l components

if N==13 % Number of sections are equal to 13.
      C=cos(tetta);
      B=sin(tetta_abs);
      B0=zeros(N,signal_length);
      C0=zeros(N,signal_length);
  for t=1:signal_length;
     for l=1:13;
         P=(p_(1:44,(l-1)*4+1:l*4,t));
         Anum(t,l)=length(nonzeros(P));      % Local areas applied with pressure
         Atot_ekv(t,l)=Anum(t,l)*A_pixsel;
         F_l(t,l)=[A_pixel*sum(sum(P))];     % Vector sith normal F__ls
     end
         B0(:,t)=B;
         C0(:,t)=C;
  end

else                                         % Number of sections > 13.
      C=cos(tetta);
      B=sin(tetta_abs);
      B0=zeros(N+1,signal_length);
      C0=zeros(N+1,signal_length);

 for t=1:signal_length;
      for l=1:q;
          P=(p_(1:44,(l-1)*(n/N)+1:l*(n/N),t));
          Anum(t,l)=length(nonzeros(P));
          Atot_ekv(t,l)=Anum(t,l)*A_pixel;
          F_l(t,l)=[A_pixel*sum(sum(P))];
      end
          B0(:,t)=B;
          C0(:,t)=C;
  end
end

F__l_ind=sum(F_l');              % Sum of normal F__ls over the sensor area
```

```
% Calculating shear F__l components

if N==13;
    F_t=zeros(N,signal_length);
    F_t(1:N,:)=F_l';
  for j=1:length(F_t(1,:));
      F__t=eye(length(F_t(:,1)),length(F_t(:,1)))*diag(F_t(:,j));
      F___t(j)=(C+u*B)'*F_t(:,j);
  end
else
    F_t=zeros(N+1,signal_length);
    F_t(1:N,:)=F_l';
  for j=1:length(F_t(1,:));
      F__t=eye(length(F_t(:,1)+1),length(F_t(:,1)+1))*diag(F_t(:,j));
      F__tn(:,j)=repmat(C,1,length(F_t(1,:))).*F_t(:,j);
  end
end

F__normal=repmat(C,1,length(F_t(1,:))).*F_t;      % Normal F__ls
F__shear=u*repmat(B,1,length(F_t(1,:))).*F_t;     % Shear F__ls

F__l=F__normal+F__shear;                          % Local F__ls in each section
F_g=sum(F__normal)+sum(F__shear);                 % Global F__l



M=signal_length;
f = (Fs*linspace(0,1,M))';
f1=(Fs/2*linspace(0,1,M/2))';

S=fft(F_l,M)/M;          % Take local F__ls into frequency domain
S_conj=conj(S');

f1=(Fs/2*linspace(0,1,M/2))';

%Spectral Matrix

for i=1:length(S(:,1));
  for j=1:length(S(1,:));
      S_FF(j,i)=S(i,j)*S_conj(j,i);
  end
end
```

```
%Auto-spectral density of the total ice F__l

for j=1:length(S(:,1));
    S_FF_=eye(length(S(1,:)),length(S(1,:)))*diag(S_FF(:,j));
    S_Fd(j)=(C+u*B)'*S_FF_*(C+u*B);
end

    S_Fd_t=ifft(S_Fd); % Inverse discrete Fourier transform of vector S_Fd.

for i=1:n;
    for j=1:n;
        Sxy=(abs(conj(S_conj(i,:)).*(S_conj(j,:))));
        Sxx=(S_conj(j,:).*conj(S_conj(j,:)));
        Syy=(S_conj(i,:).*conj(S_conj(i,:)));
        eval(['S1_' num2str(j) '_' num2str(i) ' = abs(Sxy) ']);
    end
end
```

Contact area

```
% Plotting local contact areas

figure(1)
plot(Atot_ekv(:,1),'r')
hold on
plot(Atot_ekv(:,4),'c')
hold on
plot(Atot_ekv(:,7), 'm')
hold on
plot(Atot_ekv(:,10),'k')
hold on
plot(Atot_ekv(:,13))
set(gca,'FontSize',20,'XTick',100:100:length(F_l),'XTickLabel',...
    {1:length(F_l)/100})
axis tight

figure(2)
surf(Atot_ekv(:,:)')
set(gca,'FontSize',14)

figure(3)
waterfall(F_l(:,:)')
set(gca,'FontSize',14)
xlabel('Time [s]')
zlabel('Area [m^2]','FontSize',14)
```

```
set(gca,'FontSize',20,'XTick',100:100:length(F_l),'XTickLabel',...
    {1:length(F_l)/100})
axis tight
ylabel ('Sections')
```

Time domain analysis

```
%Correlation

%BAR3C Extension of bar3, which sets the bar color corresponding to its height.

% Extra parameter: 'MaxColorVal', maxclr
% This will make the color/height of the bar absolute against this maximum
% value. Otherwise, the colors will be relative against the maximum zdata
% value of all bars on the graph.

function hh = bar3c( varargin )

[abscolor, idxabsc]=getarg('MaxColorVal',varargin{:});

if idxabsc
    varargin(idxabsc+(0:1))=[];
end

     h = bar3(varargin{:});
for ii = 1:numel(h)
    zdata = get(h(ii),'Zdata');
    cdata = makecdata(zdata(2:6:end,2),abscolor);
    set(h(ii),'Cdata',cdata, 'facecolor','flat');
end

if nargout>0,
    hh = h;
end

function [val, idx] = getarg(strname,varargin)
        idx = 0;
        val = NaN;
    for jj=1:nargin-2
       if strcmpi(varargin{jj},strname)
          idx = jj;
          val = varargin{jj+1};
          return;
       end
    end
```

```
end

function cdata = makecdata(clrs,maxclr)
        cdata = NaN(6*numel(clrs),4);
    for ii=1:numel(clrs)
        cdata((ii-1)*6+(1:6),:)=makesingle_cdata(clrs(ii));
    end
      if nargin>=2
% it doesn't matter that we put an extra value on cdata(1,1)
% this vertex is NaN (serves as a separator)
        cdata(1,1)=maxclr;
      end
end

function scdata = makesingle_cdata(clr)
        scdata = NaN(6,4);
        scdata(sub2ind(size(scdata),[3,2,2,1,2,4],[2,1,2,2,3,2]))=clr;
end


x = F_l(1:256,:);        % input data  % Introduce correlation.
[r,p] = corrcoef(x);  % Compute sample correlation and p-values.
[i,j] = find(p<0.07);  % Find significant correlations.
[i,j]                  % Display their (row,col) indices.


% Correlation plots

figure (4)
bar3c(r)                    % Correlation coefficient matrix 3-D bar chart.
view([90 90])
xlabel('Section')
ylabel('Section')

figure(5)
contourf(r)              % Correlation coeffisient contour plot
xlabel('Section')
ylabel('Section')


% Global F__l plot

  figure(1)
  plot(F__tot,'k')
  axis tight
```

```
   xlabel('Time [s]')
   ylabel('Force [kN]')


% Plots of local F__ls in different sections

figure (6)
plot(F__l(6,:),'color',[0.2 0.2 0.2],'LineWidth',4)
hold on
plot(F__l(8,:),'color',[0.7 0.7 0.7],'LineWidth',4)
set(gca,'FontSize',20,'XTick',100:100:length(F_l),'XTickLabel',...
   {1:length(F_l)/100})
axis tight
xlabel('Time [s]')
ylabel('Force [kN]')
legend('Section 6', 'Section 8')

figure (7)
plot(F__l(5,:),'color',[0.2 0.2 0.2],'LineWidth',2)
hold on
plot(F__l(9,:),'color',[0.7 0.7 0.7],'LineWidth',2)
set(gca,'FontSize',20,'XTick',100:100:length(F_l),'XTickLabel',...
   {1:length(F_l)/100})
axis tight
xlabel('Time [s]')
ylabel(' Force [kN]')
legend('Section 5', 'Section 9')

figure (8)
plot(F__l(4,:),'color',[0.2 0.2 0.2],'LineWidth',2)
hold on
plot(F__l(10,:),'color',[0.7 0.7 0.7],'LineWidth',2)
set(gca,'FontSize',20,'XTick',100:100:length(F_l),'XTickLabel',...
   {1:length(F_l)/100})
axis tight
xlabel('Time [s]')
ylabel(' Force [kN]')
legend('Section 4', 'Section 10')

figure (9)
plot(F__l(3,:),'color',[0.2 0.2 0.2],'LineWidth',2)
hold on
plot(F__l(11,:),'color',[0.7 0.7 0.7],'LineWidth',2)
set(gca,'FontSize',20,'XTick',100:100:length(F_l),'XTickLabel',...
   {1:length(F_l)/100})
```

```
axis tight
xlabel('Time [s]')
ylabel(' Force [kN]')
legend('Section 3', 'Section 11')

figure (10)

plot(F__l(2,:),'color',[0.2 0.2 0.2],'LineWidth',2)
hold on
plot(F__l(12,:),'color',[0.7 0.7 0.7],'LineWidth',2)
set(gca,'FontSize',20,'XTick',100:100:length(F_l),'XTickLabel',...
    {1:length(F_l)/100})
axis tight
xlabel('Time [s]')
ylabel(' Force [kN]')
legend('Section 2', 'Section 12')


figure (11)
plot(abs(F__l(1,:)),'color',[0.2 0.2 0.2],'LineWidth',2)
hold on
plot(abs(F__l(13,:)),'color',[0.7 0.7 0.7],'LineWidth',2)
set(gca,'FontSize',20,'XTick',100:100:length(F_l),'XTickLabel',...
   {1:length(F_l)/100})
axis tight
xlabel('Time [s]')
ylabel(' Force [kN]')
legend('Section 1', 'Section 13')
```

Frequency domain analysis

```
% Autocorrelaton plots (Sub-event eight: 100 mm/s)

  figure ('Color','w')
  plot (f(2:end/5-1),(S1_13_13(2:end/5-1)),'color','k')
  set(gca,'FontSize',16)
  line([0.3774 0.3774],[0.0 0.00001379],...
'LineWidth',3.0,'color',[0 0 0]),line ([1.258 1.258],[0.0 0.00002011],...
'LineWidth',3.0,'color',[0.4 0.5 0.3]),line([1.572 1.572],[0.0 0.000008882],...
'LineWidth',3.0,'color','b'), line([1.698 1.698],[0.0 0.00001331],...
'LineWidth',3.0,'color','g'),line([1.95 1.95],[0.0 0.00001114],...
'LineWidth',3.0,'color','r')
   set(gca,'YLim',[0 0.00003],'XLim',[0 15])
   title('Autocorrelation section 13')
   xlabel('Frequency [Hz]')
```

```
 ylabel('Magnitude')

figure ('Color','w')
plot (f(2:end/5-1),(S1_12_12(2:end/5-1)),'color','k')
set(gca,'FontSize',16)
line([1.95 1.95],[0.0 0.000567],...
'LineWidth',3.0,'color','r'),line ([1.761 1.761],[0.0 0.001645],...
'LineWidth',3.0,'color','c'),line([2.642 2.642],[0.0 0.001074],...
'LineWidth',3.0,'color','m'), line([0.2516 0.2516],[0.0 0.002706],...
'LineWidth',3.0,'color','y'), line([3.396 3.396],[0.0 0.0007362],...
'LineWidth',3.0,'color',[0.4 0.2 0.6])
 set(gca,'YLim',[0 0.004],'XLim',[0 15])
 title('Autocorrelation section 12')
 xlabel('Frequency [Hz]')
 ylabel('Magnitude')

figure ('Color','w')
plot (f(2:end/5-1),(S1_11_11(2:end/5-1)),'color','k')
set(gca,'FontSize',16)
line([0.3774 0.3774],[0.0 0.003873],...
'LineWidth',3.0,'color','k'),line ([1.258 1.258],[0.0 0.003305],...
'LineWidth',3.0,'color',[0.4 0.5 0.3]),line([1.572 1.572],[0.0 0.001127],...
'LineWidth',3.0,'color','b'), line([1.698 1.698],[0.0 0.001236],...
'LineWidth',3.0,'color','g'),line([1.95 1.95],[0.0 0.00116],...
'LineWidth',3.0,'color','r'),line([2.642 2.642],[0.0 0.001757],...
'LineWidth',3.0,'color','m'),line([3.899 3.899],[0.0 0.0009704],...
'LineWidth',3.0,'color',[0.7 0.3 0.2]);
 set(gca,'YLim',[0 0.0045],'XLim',[0 15])
 title('Autocorrelation section 11')
 xlabel('Frequency [Hz]')
 ylabel('Magnitude')

figure ('Color','w')
plot (f(2:end/5-1),(S1_9_9(2:end/5-1)),'color','k')
set(gca,'FontSize',16)
line([1.572 1.572],[0.0 0.0005861],...
'LineWidth',3.0,'color','b'),line([0.2516 0.2516],[0.0 0.00114],...
'LineWidth',3.0,'color','y'),line([3.899 3.899],[0.0 0.001024],...
'LineWidth',3.0,'color',[0.7 0.3 0.2]), line([3.396 3.396],[0.0 0.0005997],...
'LineWidth',3.0,'color',[0.4 0.2 0.6]), line([4.78 4.78],[0.0 0.0005005],...
'LineWidth',3.0,'color',[0.7 0.6 0.3]);
 set(gca,'YLim',[0 0.002],'XLim',[0 15])
 title('Autocorrelation section 9')
 xlabel('Frequency [Hz]')
 ylabel('Magnitude')
```

```
figure ('Color','w')
plot (f(2:end/5-1),(S1_5_5(2:end/5-1)),'color','k')
set(gca,'FontSize',16)
line([0.2516 0.2516],[0.0 0.001014],...
'LineWidth',3.0,'color','y'), line([4.78 4.78],[0.0 0.0005653],...
'LineWidth',3.0,'color',[0.7 0.6 0.3]), line([3.396 3.396],[0.0 0.0007698],...
'LineWidth',3.0,'color',[0.4 0.2 0.6]);
  set(gca,'YLim',[0 0.002],'XLim',[0 15])
  title('Autocorrelation section 5')
  xlabel('Frequency [Hz]')
  ylabel('Magnitude')

figure ('Color','w')
plot (f(2:end/5-1),(S1_3_3(2:end/5-1)),'color','k')
set(gca,'FontSize',16)
line([0.3774 0.3774],[0.0 0.0008682],...
'LineWidth',3.0,'color','k'),line ([1.258 1.258],[0.0 0.000864],...
'LineWidth',3.0,'color',[0.4 0.5 0.3]),line([1.698 1.698],[0.0 0.0005449],...
'LineWidth',3.0,'color','g'), line([4.78 4.78],[0.0 0.00108],...
'LineWidth',3.0,'color',[0.7 0.6 0.3]);
  set(gca,'YLim',[0 0.004],'XLim',[0 15])
  title('Autocorrelation section 3')
  xlabel('Frequency [Hz]')
  ylabel('Magnitude')

figure ('Color','w')
plot (f(2:end/5-1),(S1_2_2(2:end/5-1)),'color','k')
set(gca,'FontSize',16)
line([0.3774 0.3774],[0.0 0.003076],...
'LineWidth',3.0,'color','k'),line([1.761 1.761],[0.0 0.00146],...
'LineWidth',3.0,'color','c'),line([3.899 3.899],[0.0 0.0009484],...
'LineWidth',3.0,'color',[0.7 0.3 0.2]);
  set(gca,'YLim',[0 0.004],'XLim',[0 15])
  title('Autocorrelation section 2')
  xlabel('Frequency [Hz]')
  ylabel('Magnitude')

    figure ('Color','w')
plot (f(2:end/5-1),(S1_1_1(2:end/5-1)),'color','k')
set(gca,'FontSize',16)
line([0.3774 0.3774],[0.0 0.00005931],...
'LineWidth',3.0,'color','k'),line ([1.258 1.258],[0.0 0.00007706],...
'LineWidth',3.0,'color',[0.4 0.5 0.3]),line([2.642 2.652],[0.0 0.0001013],...
'LineWidth',3.0,'color','m'), line([1.698 1.698],[0.0 0.00001331],...
```

```
  'LineWidth',3.0,'color','c'),line([1.761 1.761],[0.0 0.000153],...
  'LineWidth',3.0,'color','r')
    set(gca,'YLim',[0 0.0002],'XLim',[0 15])
    title('Autocorrelation section 1')
    xlabel('Frequency [Hz]')
    ylabel('Magnitude')

%Spectral matrix

    figure(13)
    subplot(5,5,1), plot (f(2:end/5-1),(S1_1_1(2:end/5-1)))
     set(gca,'FontSize',18)
     axis tight
     xlabel('Frequency [Hz]')
     ylabel('Magnitude')
    subplot(5,5,2), plot (f(2:end/5-1),(S1_1_4(2:end/5-1)))
     set(gca,'FontSize',18)
     axis tight
    subplot(5,5,3), plot (f(2:end/5-1),(S1_1_7(2:end/5-1)))
     set(gca,'FontSize',18)
     axis tight
    subplot(5,5,4), plot (f(2:end/5-1),(S1_1_10(2:end/5-1)))
     set(gca,'FontSize',18)
     axis tight
    subplot(5,5,5), plot (f(2:end/5-1),(S1_1_13(2:end/5-1)))
     set(gca,'FontSize',18)
     axis tight


    subplot(5,5,7), plot (f(2:end/5-1),(S1_4_4(2:end/5-1)))
     set(gca,'FontSize',18)
     axis tight
     xlabel('Frequency [Hz]')
     ylabel('Magnitude')
    subplot(5,5,8), plot (f(2:end/5-1),(S1_4_7(2:end/5-1)))
     set(gca,'FontSize',18)
     axis tight
    subplot(5,5,9), plot (f(2:end/5-1),(S1_4_10(2:end/5-1)))
     set(gca,'FontSize',18)
     axis tight
    subplot(5,5,10), plot (f(2:end/5-1),(S1_4_13(2:end/5-1)))
     set(gca,'FontSize',18)
     axis tight

    subplot(5,5,13), plot(f(2:end/5-1),(S1_7_7(2:end/5-1)))
```

```
  set(gca,'FontSize',18)
  axis tight
  xlabel('Frequency [Hz]')
  ylabel('Magnitude')
subplot(5,5,14), plot (f(2:end/5-1),(S1_7_10(2:end/5-1)))
  set(gca,'FontSize',18)
  axis tight
subplot(5,5,15), plot (f(2:end/5-1),(S1_7_13(2:end/5-1)))
  set(gca,'FontSize',18)
  axis tight

subplot(5,5,19), plot (f(2:end/5-1),(S1_10_10(2:end/5-1)))
  set(gca,'FontSize',18)
  axis tight
  xlabel('Frequency [Hz]')
  ylabel('Magnitude')
subplot(5,5,20), plot (f(2:end/5-1),(S1_10_13(2:end/5-1)))
  set(gca,'FontSize',18)
  axis tight

subplot(5,5,25), plot (f(2:end/5-1),(S1_13_13(2:end/5-1)))
  set(gca,'FontSize',18)
  axis tight
  xlabel('Frequency [Hz]')
  ylabel('Magnitude')
```

Hammer excitation

```
% Loading files:

%c=open('HammerTestFilm-acc1-load1-no1.mat');
%c=open('HammerTestFilm-acc1-load1-no2.mat');

%c=open('HammerTestFilm-acc1-load2-no1.mat');
%c=open('HammerTestFilm-acc1-load2-no2.mat');

%c=open('HammerTestFilm-acc1-load3-no1.mat');
%c=open('HammerTestFilm-acc1-load3-no2.mat');

%c=open('HammerTestFilm-acc1-load4-no1.mat');
c=open('HammerTestFilm-acc1-load4-no2.mat');

data=c.data;
tid =c.t;
kraft=data(:,1);
```

```
Fs=1/(tid(2)-tid(1));

% Hammer excitation plot

figure(14)
plot(tid,kraft)
xlabel('Time [s]')
ylabel(' Force [N]')
```

Compression test:

```
% cal-1-ice calibration file

R=0;
window_length=20800;
signal_start=R*44+1;
signal_length=44*window_length;
pressuret=load('Ice_3_1.mat');
pressure1=pressuret.HDRS1;
p_=zeros(44,52,window_length);
k=0;

for j=signal_start:44:(signal_start+signal_length);
    k=k+1;
    p_(1:44,:,k)=pressure1(signal_start+44*(k-1):signal_start+k*44-1,:);
end

signal_length=k;

A_pixel=(0.4161*0.1565)/44/52; %Pixel area

for t=1:signal_length;
    for l=1:13;
        P=(p_(1:44,(l-1)*4+1:l*4,t));
        Anum(t,l)=length(nonzeros(P));% Local areas applied with pressure
        Atot_ekv(t,l)=Anum(t,l)*Acell;
        F_l(t,l)=[A_pixel*sum(sum(P))]; % Vector with F_l in each cell
    end
end

F__l_ind=sum(F_l');


% cal-2-ice calibration file
```

```
signal_length=44*window_length;
pressuretcal=load('Ice_3_3.mat');
pressure1cal=pressuretcal.HDRS1;
pcali_=zeros(44,52,window_length);
k=0;
for j=signal_start:44:(signal_start+signal_length);
    k=k+1;
pcali_(1:44,:,k)=pressure1cal(signal_start+44*(k-1):signal_start+k*44-1,:);
end
signal_length=k;

for t=1:signal_length;
    for l=1:13;
        Pcal=(pcali_(1:44,(l-1)*4+1:l*4,t));
        Anum(t,l)=length(nonzeros(Pcal));
        Atot_ekv(t,l)=Anum(t,l)*Acell;
        F_l_cal(t,l)=[Acell*sum(sum(Pcal))];
    end
 end


F__l_ind_cal=sum(F_l_cal');


%cal-3-ice calibration file

signal_length=44*window_length;
pressuretcal2=load('ice_crushing_4_72.mat');
pressure1cal2=pressuretcal2.HDRS1;
pcali2_=zeros(44,52,window_length);
k=0;
for j=signal_start:44:(signal_start+signal_length);
    k=k+1;
pcali2_(1:44,:,k)=pressure1cal2(signal_start+44*(k-1):signal_start+k*44-1,:);
end
signal_length=k;

for t=1:signal_length;
    for l=1:13;
        Pcal2=(pcali2_(1:44,(l-1)*4+1:l*4,t));
        Anum(t,l)=length(nonzeros(Pcal2));
        Atot_ekv(t,l)=Anum(t,l)*A_pixel;
        F_l_cal2(t,l)=[Acell*sum(sum(Pcal2))];
    end
end
```

```
% Loading data from load cell

loadcell=open('load_cell_ice.mat');
data=loadcell.Icecrushingloadcell1;
Force=data(7156:10:9236,9)/1000;
F=data(:,9)/1000;
time=data(:,1);
Fs=1/(time(6)-time(5));
timet1=linspace(0,208.01,209);




figure(15)
timet=linspace(0,208.01,20801);
timet1=linspace(0,208.01,209);
plot(timet,Force_ind_cal,'color','k')
 hold on
plot(timet,Force_ind,'color',[0.7 0.7 0.7])
 hold on
plot(timet,Force_ind_cal2,'color','r')
 hold on
plot(timet1,Force)
xlabel('Time [s]')
ylabel('Force [kN]')
axis([0 208 0 5.5])
legend('cal-1-ice calibration file','cal-2-ice calibration file',...
    'cal-3-ice calibration file','Load cell')
```

Writing .mat figures to PDF.

```
% Figure name and properties

Bredde=55;
Hoyde=20;

% Changing properies for each subplot

h = get(gcf,'Children');
test=get(h,'type');
for m=1:size(h,1)
      if strcmp('axes', test(m,1))==1
           'jepp'
          set(get(h(m,1),'xlabel'),'fontsize',20)
```

```
            set(get(h(m,1),'title'),'fontsize',20)
            set(get(h(m,1),'ylabel'),'fontsize',20)
            set(get(h(m,1),'title'),'fontsize',20)
            set(get(h(m,1),'zlabel'),'fontsize',20)
            set(h(m,1),'Fontsize',20,'Linewidth',1.0)
            set(get(h(m,1),'children'),'markersize',4)
            set(get(h(m,1),'children'),'Linewidth',1.3)
            set(h(m,1), 'FontName', 'Arial');
            set(get(h(m,1),'ylabel'),'FontName', 'Arial')
            set(get(h(m,1),'xlabel'),'FontName', 'Arial')
            set(get(h(m,1),'title'),'FontName', 'Arial')
        end
end

% Saving picture file

h=get(gcf);
set(gcf, 'PaperPositionMode', 'manual');
set(gcf, 'PaperUnits', 'centimeters');
set(gcf, 'PaperPosition', [0 0 Bredde Hoyde],'PaperSize',[Bredde Hoyde]);
```